OPTIMAL RECONSTRUCTION OF MATERIAL PROPERTIES

COMPUTATIONAL METHODS FOR THE OPTIMAL RECONSTRUCTION OF MATERIAL PROPERTIES IN COMPLEX MULTIPHYSICS SYSTEMS

By VLADISLAV BUKSHTYNOV, M.Sc., B.Sc.

A Thesis
Submitted to the School of Graduate Studies
in Partial Fulfilment of the Requirements
for the Degree
Doctor of Philosophy

McMaster University

DOCTOR OF PHILOSOPHY (2012) McMaster University

(Computational Engineering and Science) Hamilton, Ontario

TITLE:	Computational Methods for the Optimal Reconstruction of Material Properties in Complex Multiphysics Systems
AUTHOR:	Vladislav Bukshtynov, M.Sc, B.Sc. (Vitebsk State University)
SUPERVISOR:	Dr. Bartosz Protas
NUMBER OF PAGES:	xiv, 157

Abstract

In this work we propose and validate a computational method for reconstructing constitutive relations (material properties) in complex multiphysics phenomena based on incomplete and noisy measurements which is applicable to different problems arising in nonequilibrium thermodynamics and continuum mechanics. The parameter estimation problem is solved as PDE–constrained optimization using a gradient–based technique in the optimize–then–discretize framework. The reconstructed material properties taken as an example here are the transport coefficients characterizing diffusion processes such as the viscosity and the thermal conductivity, and we focus on problems in which these coefficients depend on the state variables in the system. The proposed method allows one to reconstruct a smooth constitutive relation defined over a broad range of the dependent variable. This research is motivated by questions arising in the computational analysis and optimization of advanced welding processes which involves modelling complex alloys in the liquid phase at high temperatures.

Acknowledgements

I owe sincere thanks to my supervisor Dr. Bartosz Protas for sharing with me his knowledge, for providing me with enough freedom to experiment and to feel self–confident in the area much broader than the research problem needed, for his patience, encouragement and for serving as a great example of a bright and successful scientist. I am indebted to Dr. Dmitry Pelinovsky for useful discussions and comments on my research problems and to Dr. Oleg Volkov who provided me with help and care while I was doing my very first steps at McMaster. I would also like to thank Dr. David Novog, Dr. Nikolas Provatas and Dr. James Wadsley as the Supervisory Committee members for constant guidance and support throughout my entire PhD study.

I would like to acknowledge generous funding provided for this research by the Natural Sciences and Engineering Research Council of Canada (Collaborative Research and Development Program), Ontario Centres of Excellence — Centre for Materials and Manufacturing, and General Motors of Canada. I am also indebted to the School of Computational Engineering and Science and also to the Department of Mathematics and Statistics, McMaster University, for financial assistance throughout my stay as a doctorate candidate.

I am also very grateful to my family, wife Katerina and daughter Ksenia, for providing me with their understanding, infinite patience, continuous care

and support along the hard way to this degree. My warm and sincere thanks also go to my friends and colleagues: Anton Sakovich, Dmitry Ponomarev, Diego Ayala, Ramesh Yapalparvi for all the assistance in my research, fruitful discussions and encouragement during my stay at McMaster.

To my wife Katerina and daughter Ksenia

Contents

List of Figures

List of Tables

Chapter 1

Introduction

1.1 Motivation

Reliable mathematical and computational modelling of physical processes depends on our knowledge of the relevant properties of the materials involved. Obtaining such properties is particularly challenging when the materials are of a less common type. For example, when investigating thermo–fluid phenomena occurring in liquid metals, one needs to know the coefficients of viscosity, thermal diffusivity, surface tension, etc., for the specific alloys. This task is often made more difficult by the fact that these coefficients tend to depend on the temperature in a complicated way. As a result, precise information about such material properties is rarely available, except for some common materials. The main goal of the investigation, this thesis is devoted to, is to propose and validate a suite of computational techniques that will allow one to reconstruct such material properties based on some measurements available for a particular process (e.g., heat conduction) and a particular material. The specific motivation for this investigation comes from the research on optimiza-

tion of multiphysics phenomena involved in advanced welding processes [1], where accurate data concerning material properties is quite important. While our intended applications concern more complicated systems, for the sake of clarity our approach is first developed and validated based on a fairly simple model problem, namely the reconstruction of a temperature–dependent heat conductivity coefficient in a steady–state heat equation discussed in Chapter 2. Then, we extended this approach to more complex phenomena to validate its applicability for time–dependent systems where the reconstructed property used in one conservation equation is a function of a state variable governed by a different conservation equation. Thus, as an example of such complex "multiphysics" phenomena in Chapters 3 and 4 we consider a reconstruction of the temperature dependence of the viscosity coefficient used in the momentum equation where the temperature is governed by a separate energy equation. Both models are considered under the assumption that the systems consist of a single homogenous phase; some questions concerning parameter estimation in multi–phase systems are mentioned in Chapter 5.

1.2 Parameter Reconstruction as an Inverse Problem

We start with general definitions and some notations for direct and inverse problems. Let $\mathcal{A} : \mathcal{X}_1 \to \mathcal{X}_2$ be an operator in mapping the state of the system, denoted $\mathbf{x}$, to a set of parameters, or inputs, $\mathbf{b}$

$$\mathcal{A}\,\mathbf{x} = \mathbf{b}, \tag{1.1}$$

where the inputs $\mathbf{b}$ are known. The problem of solving (1.1) with respect to $\mathbf{x}$ is usually called a *direct problem*. Following the definition given by Hadamard [2], the problem (1.1) is considered as *well–posed* (or, *well–defined*) if (i) there exists a solution for (1.1), (ii) this solution is unique and (iii) it depends continuously on the data in $\mathbf{b}$ in some reasonable topology, i.e., the solution $\mathbf{x}$ is stable with respect to perturbations in $\mathbf{b}$.

In practice, one often has to solve a different problem in which one is given some incomplete and possibly noisy measurements $\tilde{\mathbf{x}}$ of the state $\mathbf{x}$, and on the basis of this information one seeks to reconstruct the system input $\mathbf{b}$. Such problems are referred to as *inverse problems* and the broad family of parameter estimation problems represents a typical example of inverse problems. We remark that given the approximate nature of the measurements, the vectors $\tilde{\mathbf{x}}$ and $\mathbf{b}$ do not satisfy equation (1.1) exactly which typically leads to different forms of ill–posedness mentioned above. One family of approaches devised to deal with such problems relies on the variational (least–squares) formulation of (1.1), namely $\min \|\mathcal{A}\tilde{\mathbf{x}} - \mathbf{b}\|$. A major technical difficulty in solving such inverse problems tends to be lack of continuous dependence of the solution $\mathbf{b}$ on the data $\tilde{\mathbf{x}}$.

There exists a group of mathematical techniques, known as *regularization methods*, that have been developed to deal with this ill–posedness. For example, for discrete data models one of the useful and widely used techniques is the *singular value decomposition* (SVD) method [3] which consists in applying a regularizing filter function, e.g. of the Tikhonov-Phillips type, to small singular values division by which causes the instability problem. To obtain the convergence utilizing the SVD method requires some prior information about the noise level in the input data and about the true solution, which in practice is rarely available.

In problems dealing with very large systems, which require the singular value decomposition of very large matrices, implementation of Tikhonov regularization can be possible in a form of alternate variational representations applying one of the techniques from the range of *variational regularization methods* based on the total variation representation and using the Calculus of Variations and Euler–Lagrange Multiplier Theorem [4].

Statistical estimation approach, where the notion of the inverse problem is based on conditional probabilities and the Bayes' Theorem, also provides very useful tools to work with measurement errors and to regularize the solution using, for example, Bayesian or Monte Carlo (random) estimations [5].

Methods to solve inverse problems using gradients of the fit–to–data functionals and iterative procedures to minimize such functionals are called *iterative regularization methods*. While these methods require many iterations, and, though, are computationally costly, they are also able to generate an accurate regularized solution and are in use where eliminating dependence of the approach on the model's discrete structure is desirable, see e.g. [6]. In this work we in fact use methods from this category, and the main concept of iterative regularization via the adjoint–based gradient method will be illustrated on our model problems in Chapters 2 and 3.

In principle, as regards the inverse problem of parameter estimation, one can consider two distinct formulations:

- material properties depending on the *space* variable $\mathbf{x}$ (i.e., the *independent* variable in the problem), and
- material properties depending on the *state* variable T (i.e., the *dependent* variable in the problem).

Problems of the first type have in fact received quite a lot of atten-

tion in the literature, and we may refer to the monographs [7] and [5, 8] for surveys of the mathematical and more applied aspects of these problems, respectively. For example, as the reconstructed parameters are functions of the space variables, these problems represent the foundation of numerous imaging techniques in medical diagnostics, such as, e.g., X–ray tomography [8], as well as in geosciences [9, 10]. Problems of this type are at least in principle relatively well understood, and there exist several established methods for their solution.

In this work our focus will be exclusively on parameter estimation problems of the second type in which we want to determine the material properties as a function of the state (i.e., *dependent*) variable, e.g., the temperature T, rather than the position in space (the *independent* variable). In other words, we seek a relationship between the material property and the state variable that holds uniformly at *every* point $\mathbf{x}$ of the domain Ω in which the problem is formulated. This problem seems to have received less attention in the literature than the problem of estimating the space–dependent material properties. Foundations of an optimization–based approach to the solution of this problem were laid in the work of Chavent and Lemonnier [11] (which to the best of our knowledge never appeared in the English language), where the authors established the existence of solutions to the problem and derived expressions for the gradient of the least–squares error functional. They also showed the results of computations in which the cost functional gradients were obtained based on a suitably–defined adjoint system. Similar problems were also considered by Alifanov et al. [12, 13], except that in their formulation the dependence of the material property on the state variable was assumed in the form of a spline interpolant, effectively resulting in a finite–dimensional optimization problem. A computational approach also based on a least–squares error func-

tional and a linearization of the problem via a suitable change of variables was considered by Tai and Kärkkäinen [14]. An alternative technique utilizing the adjoint equations, but without making use of the error functional, was proposed by DuChateau et al. [15], whereas Janicki and Kindermann studied a method combining Green's functions and Landweber's iteration applied to the parameter–to–measurements map [16]. A different approach, based on the "equation error method", was pursued by Hanke and Scherzer [17] who also considered a discrete formulation. Some mathematical aspects of the inverse problem of determining the state–dependent diffusion coefficients were addressed by Kügler [18, 19] who investigated the Tikhonov regularization, by Neubauer [20] who studied regularization using adaptive grids and also by DuChateau et al. [21, 22]. Limited–memory algorithms applicable to large–scale non–smooth optimization problems are discussed in [23]. Some analytical results concerning this problem posed in an infinite domain were also reported in [24].

1.3 Challenges in the Reconstruction of State–Dependent Parameters

While adjoint analysis is now routinely used to solve partial differential equation (PDE)–constrained optimization problems [25], we emphasize that the structure of the gradients in the present investigation will in fact be shown to be quite different from what is encountered in typical problems [6]. The reason is that the optimization variable is a function of the dependent, rather than independent, variables in the problem. We also add that, in contrast to the results reported in some of the references quoted in the present Chapter,

our approach is formulated in the "optimize–then–discretize" framework, i.e., while we ultimately discretize the problem for the purpose of a numerical solution, our optimality conditions and the cost functional gradients are derived in the continuous (PDE) setting. As a consequence,

- the main constituents of our approach are independent of the specific discretization used,
- the method provides explicit control on regularity of the obtained reconstruction and
- the approach is more elegant from the point of view of mathematical derivation.

An issue which typically appears in this class of state–dependent reconstruction problems is that the gradient generates the sensitivity information only over a specific range of a state variable, namely the identifiability region (precise definition will be given later in Chapter 2), which tends to be smaller than the desired interval of the reconstruction. While the cost functional gradient may be formally extended outside this identifiability interval, such techniques are not capable of accurately reconstructing the material properties for broader values of the state variable. Thus, a systematic approach is proposed to modify the inputs to the system, so that the reconstructed constitutive relation can be estimated over the desired range of the temperature.

We reiterate also that the main goal of our research is to develop and validate a self–contained suite of computational techniques for reconstructing solution–dependent material properties for a broad range of problems arising in nonequilibrium thermodynamics and continuum mechanics. This implies an ability of the proposed approach to be easily extended for multiphysics

problems of different degree of complexity, in different dimensions and on domains with different geometry. In a view of such possible extensions, we may note that applying these methods to more complex multiphysics problems will lead in complications of technical character only, e.g. in the derivation of the cost functional gradient, while adding the time–dependency and/or changing the model geometry (increasing dimensions or the domain complexity) will affect only the computational aspect of the solution.

1.4 Outline of the Thesis and Summary of the Results

The thesis focuses on an optimization–based approach to estimation of a state–dependent material property and the main contributions of this work are as follows. For the first simplified model

- we provide a novel expression for the gradient of the cost functional which is more computationally tractable than the formula originally derived in [11].

We then extend this approach to derive an expression for the gradient in a complex multiphysics problem. We also show the applicability of the entire approach, first developed and validated for the simple "toy" problem, for complex problems, including multiphysics, time–dependence and higher dimensions, addressing, in particular, the following issues:

- recognizing that in the standard formulation (based on the L_2 inner products) the cost functional gradients may be discontinuous or at least do not show required regularity, we develop an approach ensuring a required degree of smoothness of the reconstructed material properties,

- noting that in a given problem reconstruction is normally limited to the corresponding identifiability region, we propose a systematic experimental design procedure that allows one to tune inputs to the system, so that the constitutive relation can be reconstructed over a broader range of the state variable, and

- in view of the general ill-posedness of the parameter estimation problems, in the sense that measurement noise results in instabilities of the solutions, we analyze the performance of the approach in the presence of noise and assess the efficiency of Tikhonov regularization.

We also address a number of computational challenges related to accurate and efficient evaluation of cost functional gradients. As in 2D and 3D these gradients are given in terms of integrals over manifolds defined by a level-set function, we analyze and compare three different methods for evaluation of cost functional gradients. In particular

- we demonstrate, both theoretically and computationally, the superior accuracy and efficiency of a novel numerical approach to the evaluation of gradients which is elaborated in this thesis.

The structure of the thesis is as follows: in the next Chapter we formulate and validate the optimization–based approach to estimation of a state–dependent material property based on a simple 1D model problem involving a steady–state heat equation. Chapter 3 is devoted to extension of this approach to more complex multiphysics phenomena to validate its applicability for time–dependent systems where the reconstructed material property appearing in one conservation equation is a function of a state variable governed by a different conservation equation. More specifically, we consider the reconstruction of the temperature dependence of the viscosity coefficient in the

momentum equation, where the temperature is governed by a separate energy equation. In Chapter 4 we present extensive computational results concerning the reconstruction in a such complex multiphysics system, whereas in Chapter 5 we outline briefly other possible extensions for the proposed approach and open the discussion for future research problems; summary and conclusions are deferred to Chapter 6. We also add that at the core of the thesis there are two papers, with Chapter 2 built on the material presented in an already published work [26], and with Chapters 3 and 4 containing results which will be reported in another manuscript [27], currently in the final stages of preparation.

Chapter 2

Formulation of the Problem based on a Simplified Model

2.1 Description of the Simplified Model

In order to ensure applicability of our proposed approach to a broad array of problems in continuum mechanics and nonequilibrium thermodynamics, we formulate it in terms of reconstruction of constitutive relations. Thus, we will consider optimal reconstruction of isotropic constitutive relationships between thermodynamic variables based on measurements obtained in a spatially–extended system. In other words, assuming the constitutive relation in the following general form

$$\begin{bmatrix} \text{thermodynamic} \\ \text{flux} \end{bmatrix} = k\,(\text{state variables}) \begin{bmatrix} \text{thermodynamic} \\ \text{“force”} \end{bmatrix}, \tag{2.1}$$

our approach allows us to reconstruct the dependence of the transport coefficient k on the state variables consistent with the assumed governing equations.

Constitutive relations in form (2.1) arise in many areas of nonequilibrium thermodynamics and continuum mechanics. To fix attention, but without loss of generality, in the first simple model problem we focus on a heat conduction problem in which the heat flux $\mathbf{q}$ represents the thermodynamic flux, whereas the temperature gradient $\boldsymbol{\nabla} T$ is the thermodynamic "force", so that relation (2.1) takes the specific form

$$\mathbf{q}(\mathbf{x}) = -k(T)\, \boldsymbol{\nabla} T(\mathbf{x}), \qquad \mathbf{x} \in \Omega, \tag{2.2}$$

where $\Omega \subset \mathbb{R}^d$, $d = 1, 2, 3$, is an open domain in which the problem is formulated. We note that by assuming the function $k : \mathbb{R} \to \mathbb{R}$ to be given by a constant, we recover the well–known linear Fourier law of heat conduction. While expressions for the transport coefficients such as $k(T)$ are typically obtained using methods of statistical thermodynamics or just empirically, in the present investigation we will show how to reconstruct the function $k(T)$ based on some available measurements of the spatial distribution of the state variable T combined with the relevant conservation law. Such a technique could be useful, for example, to systematically adjust the form of a constitutive relationship derived theoretically to better match actual experimental data. Combining constitutive relation (2.2) with an expression for the conservation of energy, we obtain a partial differential equation describing the distribution of the temperature T in the domain Ω corresponding to the distribution of heat sources $g : \Omega \to \mathbb{R}$ and suitable boundary conditions (for example, of the Dirichlet type), i.e.,

$$-\boldsymbol{\nabla} \cdot [k(T)\, \boldsymbol{\nabla} T] = g \qquad \text{in } \Omega, \tag{2.3a}$$

$$T = T_0 \qquad \text{on } \partial\Omega, \tag{2.3b}$$

where T_0 denotes the boundary temperature. Instead of (2.3b), we could also consider Neumann boundary conditions involving $k(T)\frac{\partial T}{\partial n}$, where $\mathbf{n}$ is the unit vector normal to the boundary $\partial\Omega$ and pointing out of the domain, and our subsequent analysis would essentially be unchanged. In regard to reconstruction of constitutive relations, it is important that such relations be consistent with the second principle of thermodynamics [28]. There exist two mathematical formalisms, one due to Coleman and Noll [29] and another one due to Liu [30], developed to ensure in a very general setting that a given form of the constitutive relation does not violate the second principle of thermodynamics. In continuous thermodynamical and mechanical systems this principle is expressed in terms of the Clausius–Duhem inequality [31] which in the case of the present simple model problem (2.2)–(2.3) reduces to the statement that $k(T) > 0$ for all values of T. At the same time, the condition $k(T) > 0$ is also required for the mathematical well–posedness of elliptic boundary value problem (2.3). In addition, to ensure the existence of classical (strong) solutions of (2.3), we will assume that the heat source $g(\mathbf{x}) > 0$ is at least a continuous function of $\mathbf{x}$. This appears reasonable taking into account possible physical phenomena represented by this term. The positivity of g allows us to establish a lower bound on classical solutions of problem (2.3), cf. Appendix A.

We should also define two intervals:

- $[T_\alpha, T_\beta] \triangleq [\min_{\mathbf{x}\in\overline{\Omega}} T(\mathbf{x}), \max_{\mathbf{x}\in\overline{\Omega}} T(\mathbf{x})]$ which represents the range spanned by the solution of problem (2.3); we note that, as demonstrated in Appendix A, the minimum T_α is attained at the boundary $\partial\Omega$; following [19], we will refer to the interval $\mathcal{I} \triangleq [T_\alpha, T_\beta]$ as the *identifiability interval*,

- $\mathcal{L} \triangleq [T_a, T_b]$, where $T_a \leq T_\alpha$ and $T_b \geq T_\beta$; this will be the interval on which we will seek to obtain a reconstruction of the constitutive relation; we note that in general the interval $\mathcal{L}$ will be larger than the identifiability interval, i.e., $\mathcal{I} \subseteq \mathcal{L}$.

It is assumed that the constitutive relations $k(T)$ are differentiable functions of the state variable (temperature) and belong to the following set

$$\mathcal{K} = \{k(T) \text{ piecewise } C^1 \text{ on } \mathcal{L};\ 0 < m_k < k(T) < M_k,\ \forall\, T \in \mathcal{L}\}, \qquad (2.4)$$

where $m_k, M_k \in \mathbb{R}^+$, whereas solutions of problem (2.3) belong to $H^1(\Omega)$, i.e., the Sobolev space of functions defined on Ω with square–integrable derivatives.

The specific parameter estimation problem that we address in this investigation is formulated as follows. Given a set of continuous "measurements" $\tilde{T}(\mathbf{x})$, $\mathbf{x} \in \Sigma$, of the state variable (temperature) T acquired on the sensing domain $\Sigma \subseteq \Omega$, we seek to reconstruct the constitutive relation $k(T)$ for $T \in \mathcal{L}$ such that the solutions of problem (2.3) obtained with this reconstructed function $k(T)$ will best match the available measurements in the least–squares sense. Therefore, the constitutive relation $k(T)$ can be regarded as the "cause", whereas the measurements of the temperature field as the "effect". The general reconstruction problem is set up here based on continuous measurements, as required for consistency with the PDE–based formulation of the optimization problem. However, when we perform actual computations based on discretized PDEs, continuous measurements will be expressed in terms of suitable pointwise measurements which are more relevant from the application point of view. While our main goal in this investigation is to develop an efficient computational algorithm for this problem, some basic mathematical results concerning differentiability of the system outputs (mea-

surements) with respect to the constitutive relation are recalled in Appendix B. Parameter estimation problems in general tend to be ill–posed [5], in the sense that measurement noise usually results in instabilities of the computed solutions. Therefore, we will analyze the performance of our method in the presence of noise, and will also assess the efficiency of Tikhonov regularization.

2.2 Parameter Estimation as an Optimization Problem

We will assume that the set $\mathcal{K}$ consisting of constitutive relations $k(T)$ defined on $\mathcal{L}$ is embedded in a Hilbert (function) space $\mathcal{X}$ to be specified below. Solving our parameter estimation problem is therefore equivalent to finding a solution to the operator equation

$$\mathcal{F}(k) = T, \tag{2.5}$$

where $\mathcal{F} : \mathcal{K} \to L_2(\Sigma)$ is the map from the constitutive relations to the measurements. An approach commonly used to solve such problems consists in reformulating them as least–squares minimization problems which in the present case can be done by defining the cost functional $\mathcal{J} : \mathcal{X} \to \mathbb{R}$ as

$$\mathcal{J}(k) \triangleq \frac{1}{2} \int_{\Sigma} \left[\tilde{T}(\mathbf{x}) - T(\mathbf{x}; k) \right]^2 d\mathbf{x}, \tag{2.6}$$

where the dependence of the temperature field $T(\cdot; k)$ on the form of the constitutive relation $k = k(T)$ is given by governing equation (2.3), and "$\triangleq$" means "equal to by definition". We will find minimizers of (2.6) using methods of gradient–based optimization and the required differentiability of map (2.5) with respect to k when $\mathcal{X} = H^1(\mathcal{I})$ is established in Appendix B. The

optimal reconstruction $\hat{k}$ is therefore obtained as an unconstrained minimizer of cost functional (2.6), i.e.,

$$\hat{k} = \underset{k \in \mathcal{X}}{\operatorname{argmin}} \mathcal{J}(k). \tag{2.7}$$

It is characterized by the first–order optimality condition which requires the directional differential of cost functional $\mathcal{J}$, defined as $\mathcal{J}'(k;k') = \lim_{\epsilon \to 0} \epsilon^{-1}[\mathcal{J}(k+\epsilon k') - \mathcal{J}(k)]$, to vanish for all perturbations $k' \in \mathcal{X}$ [32], i.e.,

$$\forall_{k' \in \mathcal{X}} \qquad \mathcal{J}'(\hat{k};k') = 0. \tag{2.8}$$

The (local) optimizer $\hat{k}$ can be computed with the following gradient descent algorithm as $\hat{k} = \lim_{n \to \infty} k^{(n)}$, where

$$\begin{cases} k^{(n+1)} = k^{(n)} - \tau^{(n)} \boldsymbol{\nabla}_k \mathcal{J}(k^{(n)}), & n = 1, \dots, \\ k^{(1)} \quad = k_0, \end{cases} \tag{2.9}$$

in which $\boldsymbol{\nabla}_k \mathcal{J}(k)$ represents the *gradient* of cost functional $\mathcal{J}(k)$ with respect to the control variable k (we will adopt the convention that a subscript on the operator $\boldsymbol{\nabla}$ will be used when differentiation is performed with respect to variables other than $\mathbf{x}$), $\tau^{(n)}$ is the length of the step along the descent direction at the n–th iteration, whereas k_0 is the initial guess taken, for instance, as a constant corresponding to a linear version of constitutive relation (2.2), or some other approximate theoretical prediction. For the sake of clarity, formulation (2.9) represents the steepest–descent algorithm, however, in practice one typically uses more advanced minimization techniques, such as the conjugate gradient method, or one of the quasi–Newton techniques [33]. We note that, since minimization problem (2.6)–(2.7) is in general nonconvex,

condition (2.8) characterizes only a *local*, rather than *global*, minimizer. We reiterate that the constitutive property is required to satisfy the additional positivity condition $k(T) > 0$ for all $T \in \mathcal{L}$. Therefore, to be more precise, the optimal reconstruction $\hat{k}$ should be obtained as an *inequality*–constrained minimizer of cost functional (2.6), i.e.,

$$\hat{k} = \underset{\substack{k\in\mathcal{X},\\ k(T)>0,\ T\in\mathcal{L}}}{\operatorname{argmin}} \ \mathcal{J}(k). \tag{2.10}$$

We add that in problems involving constitutive relations depending on several state variables the inequality constraint $k(T) > 0$ will be replaced with a more general form of the Clausius–Duhem inequality [31]. Inequality–constrained problem (2.10) can be transformed to an unconstrained formulation analogous to (2.7) using for example the barrier function approach [34]. Other computational techniques for solution of inequality–constrained parameter estimation problems are discussed in [4]. However, in the computational studies performed for our current model problem and reported in Section 2.6 all solutions we found satisfied the condition $k(T) > 0$, $\forall T \in \mathcal{L}$, without having to enforce this condition explicitly. Hence, this issue will not be considered in the present Chapter, although we revisit it in the context of more complicated problem in Chapter 3.

2.3 Cost Functional Gradients via Adjoint–based Analysis

The key ingredient of minimization algorithm (2.9) is computation of the cost functional gradient $\boldsymbol{\nabla}_k \mathcal{J}(k)$. We emphasize that, since $k = k(T)$ is a contin-

uous variable, the gradient $\boldsymbol{\nabla}_k \mathcal{J}(k)$ represents in fact an infinite–dimensional sensitivity of $\mathcal{J}(k)$ to perturbations of $k(T)$. Since our constitutive relations belong to set $\mathcal{K}$, cf. (2.4), we will seek to reconstruct $k(T)$ as elements of the Sobolev space $H^1(\mathcal{L})$, so that the gradient $\boldsymbol{\nabla}_k \mathcal{J}$ will need to be obtained with respect to the corresponding inner product. However, in order to make the derivation procedure easier to follow, we will first obtain an expression for the gradient in the space $L_2(\mathcal{L})$, and only then will obtain the Sobolev gradients which will be eventually used in the solution of optimization problem (2.7). In both steps our transformations will be formal. We begin by computing the directional differential of cost functional (2.6) which yields

$$\mathcal{J}'(k;k') = \int_\Sigma [T(\mathbf{x};k) - \tilde{T}(\mathbf{x})]\, T'(\mathbf{x};k,k')\, d\mathbf{x}, \tag{2.11}$$

where the perturbation variable $T'(\mathbf{x}_i;k,k')$ satisfies the perturbation system obtained from (2.3). Next, we invoke the Riesz representation theorem [35] for the directional differential $\mathcal{J}'(k;\cdot)$, which yields

$$\mathcal{J}'(k;k') = \langle \boldsymbol{\nabla}_k \mathcal{J}, k' \rangle_{\mathcal{X}}, \tag{2.12}$$

where $\langle \cdot,\cdot \rangle$ represents an inner product in the Hilbert space $\mathcal{X}$ (we will first set $\mathcal{X} = L_2(\mathcal{L})$ and afterwards change that to $\mathcal{X} = H^1(\mathcal{L})$). We note that the expression on the right–hand side (RHS) in (2.11) is not consistent with Riesz representation (2.12), since the perturbation variable k' is hidden in the system defining $T'(k,k')$. However, this expression can be transformed to Riesz form (2.12) with the help of a suitably–defined adjoint variable. Since our derivation of this result for the present problem is in fact quite different from the approach followed in [11], we state it in the form of the following

theorem.

Theorem 2.1 *Let Ω be a smooth bounded open set and $k' \in \mathcal{X} = L_2(\mathcal{L})$. We assume that the function g and the solution T of (2.3) are sufficiently smooth. Then, the Riesz representation of directional differential (2.11) has the form*

$$\mathcal{J}'(k;k') = \int_{T_a}^{T_b} \left[\int_\Omega \chi_{[T_\alpha, T(\mathbf{x})]}(s) \Delta T^* \, d\mathbf{x} - \int_{\partial\Omega} \chi_{[T_\alpha, T(\mathbf{x})]}(s) \frac{\partial T^*}{\partial n} \, d\sigma \right] k'(s) \, ds, \tag{2.13}$$

where $\chi_{[a,b]}(s)$ is the characteristic function for an interval $[a,b]$ defined as follows

$$\chi_{[a,b]}(s) = \begin{cases} 1, & s \in [a,b], \\ 0, & s \notin [a,b], \end{cases}$$

whereas the adjoint state T^* is defined as the solution of the system

$$k(T)\boldsymbol{\Delta} T^* = [\tilde{T}(\mathbf{x}) - T(\mathbf{x})]\chi_\Sigma(\mathbf{x}), \qquad \text{in } \Omega, \tag{2.14a}$$

$$T^* = 0, \qquad \text{on } \partial\Omega, \tag{2.14b}$$

where

$$\chi_\Sigma(\mathbf{x}) = \begin{cases} 1, & \mathbf{x} \in \Sigma, \\ 0, & \mathbf{x} \notin \Sigma, \end{cases}$$

denotes the characteristic function of the sensing domain Σ.

Proof. While in principle the proof could be formulated based on the original form of governing system (2.3), the derivation and structure of the resulting expressions for the gradient $\boldsymbol{\nabla}_k \mathcal{J}$ are simplified by a change of variables known as the "Kirchhoff transformation" [36]. We thus introduce an auxiliary

function $V : \mathcal{I} \to \mathbb{R}$ defined as follows

$$V(T) \triangleq \int_{T_\alpha}^{T} k(s)\, ds. \tag{2.15}$$

Noting that in fact $T = T(\mathbf{x})$, we have $\boldsymbol{\nabla} V(\mathbf{x}) = k(T(\mathbf{x}))\, \boldsymbol{\nabla} T(\mathbf{x})$, and governing system (2.3) can be expressed as

$$-\boldsymbol{\Delta} V = g \qquad \text{in } \Omega, \tag{2.16a}$$

$$V(\mathbf{x}) = \int_{T_\alpha}^{T_0(\mathbf{x})} k(s) ds \qquad \text{on } \partial\Omega. \tag{2.16b}$$

(Using one symbol V to denote functions depending on T and $\mathbf{x}$ admittedly represents an abuse of notation, yet is justified here by simplicity.) Let $T^* : \Omega \to \mathbb{R}$ be an adjoint variable. We integrate (2.16a) against T^* to obtain

$$-\int_\Omega (\boldsymbol{\Delta} V)\, T^* d\mathbf{x} = \int_\Omega g\, T^* d\mathbf{x},$$

and then integrating by parts we get

$$\int_\Omega \boldsymbol{\nabla} V \cdot \boldsymbol{\nabla} T^*\, d\mathbf{x} - \int_{\partial\Omega} \frac{\partial V}{\partial n}\, T^*\, d\sigma = \int_\Omega g\, T^* d\mathbf{x}. \tag{2.17}$$

Next we differentiate (2.17) with respect to k

$$\int_\Omega \boldsymbol{\nabla} V' \cdot \boldsymbol{\nabla} T^* d\mathbf{x} - \int_{\partial\Omega} \frac{\partial V'}{\partial n} T^* d\sigma = 0,$$

where the perturbation variable V' can be expressed as [cf. (2.15)]

$$V'(T) = \int_{T_\alpha}^{T} k'(s)\, ds + k(T) T'(k, k'), \tag{2.18}$$

so that after integrating by parts one more time we obtain

$$\begin{aligned} &-\int_\Omega \left[\int_{T_\alpha}^{T(\mathbf{x})} k'(s)ds\right] \Delta T^* d\mathbf{x} - \int_\Omega k(T)T'\Delta T^* d\mathbf{x} \\ &+\int_{\partial\Omega} \left[\int_{T_\alpha}^{T(\mathbf{x})} k'(s)ds + k(T)T'\right] \frac{\partial T^*}{\partial n} d\sigma - \int_{\partial\Omega} \frac{\partial V'}{\partial n} T^* d\sigma = 0. \end{aligned} \tag{2.19}$$

We now require that the adjoint variable T^* satisfy system (2.14). We note that owing to the judicious choice of the RHS term in (2.14a), the second term in relation (2.19) is in fact equal to the directional differential $\mathcal{J}'(k;k')$, so that we have

$$\mathcal{J}'(k;k') = \int_\Omega \left[\int_{T_\alpha}^{T(\mathbf{x})} k'(s)\, ds\right] \Delta T^*\, d\mathbf{x} - \int_{\partial\Omega} \left[\int_{T_\alpha}^{T(\mathbf{x})} k'(s)\, ds\right] \frac{\partial T^*}{\partial n} d\sigma. \tag{2.20}$$

We also notice that the boundary terms in (2.19) having T' and T^* as factors vanish due to the boundary conditions on the state and adjoint variables, respectively, (2.3b) and (2.14b). Finally, expression (2.13) for the Riesz representation of directional differential (2.11) can be obtained from (2.20) using the characteristic function $\chi_{[T_\alpha,T(\mathbf{x})]}(s)$ and reversing the order of integration with respect to $\mathbf{x}$ and s, where this last step is justified by Fubini's theorem. □

With the Riesz representation established in (2.13), we now proceed to identify expressions for the cost functional gradient $\boldsymbol{\nabla}_k \mathcal{J}$ according to (2.12). While this is not the gradient that we will use in actual computations, we analyze first the "simplest" case when $\mathcal{X} = L_2(\mathcal{L})$, i.e., the space of functions square integrable on $[T_a, T_b]$, as it already offers some interesting insights into the structure of the problem. The L_2 gradient of the cost functional hence

takes the form

$$\boldsymbol{\nabla}_k^{L_2}\mathcal{J}(s) = \int_\Omega \chi_{[T_\alpha,\, T(\mathbf{x})]}(s)\Delta T^*\, d\mathbf{x} - \int_{\partial\Omega} \chi_{[T_\alpha,\, T(\mathbf{x})]}(s)\frac{\partial T^*}{\partial n}\, d\sigma. \tag{2.21}$$

We will now show that (2.21) is in fact equivalent to the cost functional gradient derived by Chavent and Lemonnier in [11] and adapted to the present time–independent problem. Let us consider the differentiation in (2.21) in the sense of distributions. Integration by parts of the first term on the RHS in (2.21) and the resulting cancelation of the second term yield

$$\boldsymbol{\nabla}_k^{L_2}\mathcal{J}(s) = -\int_\Omega \nabla\chi_{[T_\alpha,\, T(\mathbf{x})]}(s)\cdot\nabla T^*\, d\mathbf{x}. \tag{2.22}$$

The characteristic function $\chi_{[T_\alpha,T(\mathbf{x})]}(s)$ is a combination of Heaviside functions with respect to T. Therefore, its distributional derivative with respect to $\mathbf{x}$ can be expressed using the chain rule and a Dirac delta function as follows

$$\boldsymbol{\nabla}_k^{L_2}\mathcal{J}(s) = -\int_\Omega \delta(T(\mathbf{x})-s)\,\nabla T\cdot\nabla T^*\, d\mathbf{x} = \frac{d}{ds}\int_\Omega \chi_{[T_\alpha,T(\mathbf{x})-s]}(s)\,\nabla T\cdot\nabla T^*\, d\mathbf{x} \tag{2.23}$$

which is essentially the form of the cost functional gradient obtained in [11]. We note that the expression on the RHS in (2.23) involves differentiation of an integral with respect to the level set defining the integration region, an operation that is rather difficult to perform accurately in numerical computations. Using (2.14a) we can transform expression for cost functional gradient (2.21) to a form more convenient from the point of view of numerical computations, namely

$$\boldsymbol{\nabla}_k^{L_2}\mathcal{J}(s) = \int_\Sigma \chi_{[T_\alpha,\, T(\mathbf{x})]}(s)\frac{\tilde{T}(\mathbf{x})-T(\mathbf{x})}{k(T(\mathbf{x}))}\, d\mathbf{x} - \int_{\partial\Omega} \chi_{[T_\alpha,\, T(\mathbf{x})]}(s)\frac{\partial T^*}{\partial n}\, d\sigma, \tag{2.24}$$

where the numerical differentiation (with respect to $\mathbf{x}$) is only required in the second integral term.

The L_2 gradients have been used in numerous computational studies involving PDE–constrained optimization problem. In regard to the possibility of using the gradient $\boldsymbol{\nabla}_k^{L_2}\mathcal{J}$ in the computations for the present problem, the following comments are in place:

1. gradient (2.21), or (2.24), is nonvanishing for $s \in \mathcal{I}$, and therefore the sensitivity of the functional $\mathcal{J}(k)$ to perturbations of k can only be determined on the identifiability region $\mathcal{I}$ which is typically smaller than the region $\mathcal{L}$ over which one would wish to reconstruct the constitutive relation; the relationships between the interval $\mathcal{L}$ and the identifiability region $\mathcal{I}$, the physical and the state spaces are illustrated in Figure 2.1 where we assumed $\Omega = (-1, 1)$,

2. in view of the structure of expression (2.24), the L_2 gradient $\boldsymbol{\nabla}_k^{L_2}\mathcal{J}$ is in general a discontinuous function.

Evidently, in view of the issues mentioned above, the L_2 gradients are unsuitable for the reconstruction of the constitutive relations with the required properties, cf. (2.4). We will show that these difficulties can be overcome using cost functional gradients defined in the Sobolev space consistent with the functional setting of the problem, here $H^1(\mathcal{L})$ [37, 38]. Such gradients are guaranteed to be sufficiently smooth and are obtained in a straightforward way from the L_2 gradients. Furthermore, these gradients can be defined on the entire interval $[T_a, T_b]$ without an artificial extension by zero and can be naturally combined with a technique to shift the identifiability region. The Sobolev gradients are discussed below, whereas shifting the identifiability region is introduced in Section 2.5.

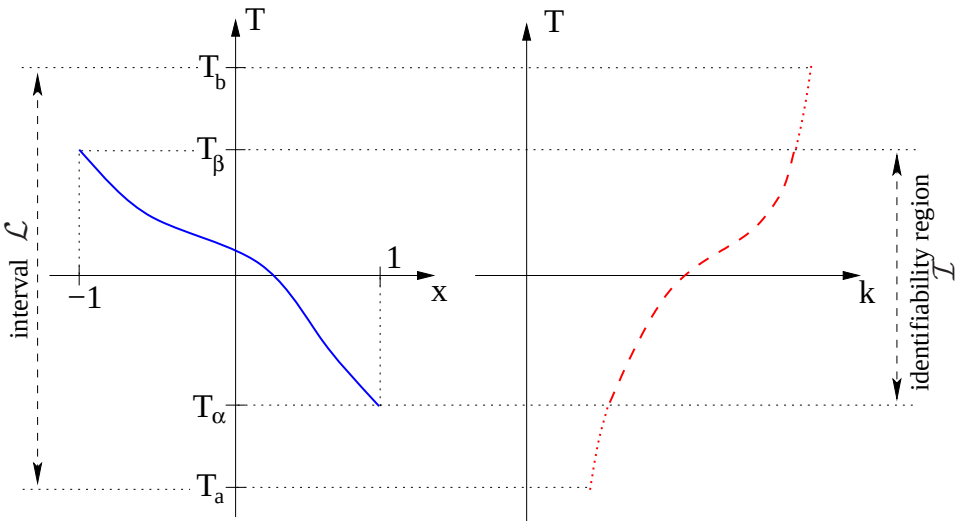

Figure 2.1: Schematic showing (left) the solution $T(x)$ of governing system (2.3) and (right) the corresponding constitutive relation $k(T)$ defined over their respective domains, i.e., $\Omega = (-1, 1)$ and the identifiability region $\mathcal{I}$. The thick dotted line represents the extension of the constitutive relation $k(T)$ from $\mathcal{I}$ to the interval $\mathcal{L}$. In the figure on the right the horizontal axis is to be interpreted as the ordinate.

When defining Sobolev gradients in a PDE–constrained optimization problem one needs to specify suitable boundary conditions characterizing the behavior of the gradient on the boundary of its domain of definition. In "classical" problems in which the control parameter is a function of the independent variables in the problem, the choice of these boundary conditions usually follows quite naturally from the structure of the governing PDE. This is, however, not the case in the present problem where it is not obvious what behavior should be imposed on the gradient at the limits of the interval $\mathcal{L}$. Out of several different possibilities, we choose to examine the following two approaches.

In the first approach we construct the Sobolev gradients $\boldsymbol{\nabla}_k^{H^1}\mathcal{J}$ by assuming that $\mathcal{X} = H^1(\mathcal{L})$, where the Sobolev space $H^1(\mathcal{L})$ is endowed with the following inner product

$$\langle z_1, z_2\rangle_{H^1(\mathcal{L})} = \int_{T_a}^{T_b}\left[z_1 z_2 + \ell^2 \frac{dz_1}{ds}\frac{dz_2}{ds}\right] ds, \qquad z_1, z_2 \in H^1(\mathcal{L}) \tag{2.25}$$

in which $\ell \in \mathbb{R}$ is a parameter with the meaning of a length–scale [we note that the L_2 inner product is obtained by setting $\ell = 0$ in (2.25)]. Next, we again invoke the Riesz representation theorem, however, now we assume that $k' \in H^1(\mathcal{L})$, so that we obtain

$$\begin{aligned}\mathcal{J}'(k;k') &= \langle \boldsymbol{\nabla}_k^{L_2}\mathcal{J}, k'\rangle_{L_2(\mathcal{L})} = \langle \boldsymbol{\nabla}_k^{H^1}\mathcal{J}, k'\rangle_{H^1(\mathcal{L})} \\ &= \int_{T_a}^{T_b}\left[\boldsymbol{\nabla}_k^{H^1}\mathcal{J}\, k'(s) + \ell^2 \frac{d(\boldsymbol{\nabla}_k^{H^1}\mathcal{J})}{ds}\frac{dk'}{ds}\right] ds.\end{aligned} \tag{2.26}$$

Performing integration by parts and imposing the homogeneous Neumann boundary conditions on the Sobolev gradient, i.e., $\frac{d}{ds}\boldsymbol{\nabla}_k^{H^1}\mathcal{J}\big|_{T_a,T_b}=0$, we obtain

$$\mathcal{J}'(k;k')=\int_{T_a}^{T_b}\boldsymbol{\nabla}_k^{L^2}\mathcal{J}\,k'(s)\,ds=\int_{T_a}^{T_b}\left[\boldsymbol{\nabla}_k^{H^1}\mathcal{J}-\ell^2\frac{d^2}{ds^2}\boldsymbol{\nabla}_k^{H^1}\mathcal{J}\right]k'(s)\,ds. \tag{2.27}$$

Noting that relation (2.27) must be satisfied for any arbitrary k', we conclude that the Sobolev gradient $\boldsymbol{\nabla}_k^{H^1}\mathcal{J}$ can be determined as a solution of the following inhomogeneous elliptic boundary–value problem

$$\boldsymbol{\nabla}_k^{H^1}\mathcal{J}-\ell^2\frac{d^2}{ds^2}\boldsymbol{\nabla}_k^{H^1}\mathcal{J}=\boldsymbol{\nabla}_k^{L^2}\mathcal{J}\qquad\text{on }(T_a,T_b), \tag{2.28a}$$

$$\frac{d}{ds}\boldsymbol{\nabla}_k^{H^1}\mathcal{J}=0\qquad\text{for } s=T_a,T_b. \tag{2.28b}$$

On the other hand, in the second approach we construct the Sobolev gradients $\boldsymbol{\nabla}_k^{H^1}\mathcal{J}$ by first assuming that $\mathcal{X}=H^1(\mathcal{I})$, where the Sobolev space $H^1(\mathcal{I})$ is endowed with an inner product analogous to (2.25), except that integration is now from T_α to T_β. Proceeding as above and imposing the homogeneous Neumann boundary conditions at the end points of the identifiability interval $\mathcal{I}$ we obtain the gradient $\boldsymbol{\nabla}_k^{H^1}\mathcal{J}$ as a solution of the following inhomogeneous elliptic boundary–value problem

$$\boldsymbol{\nabla}_k^{H^1}\mathcal{J}-\ell^2\frac{d^2}{ds^2}\boldsymbol{\nabla}_k^{H^1}\mathcal{J}=\boldsymbol{\nabla}_k^{L^2}\mathcal{J}\qquad\text{on }(T_\alpha,T_\beta), \tag{2.29a}$$

$$\frac{d}{ds}\boldsymbol{\nabla}_k^{H^1}\mathcal{J}=0\qquad\text{for } s=T_\alpha,T_\beta. \tag{2.29b}$$

In order to be able to reconstruct the relation $k(T)$ over the entire interval $\mathcal{L}$ we need to extend the Sobolev gradient defined in (2.29) onto $\mathcal{L}$. We do this

by prescribing

$$\nabla_k^{H^1}\mathcal{J}(s) = \nabla_k^{H^1}\mathcal{J}(T_\alpha) \qquad \text{for } s \in [T_a, T_\alpha], \tag{2.30a}$$

$$\nabla_k^{H^1}\mathcal{J}(s) = \nabla_k^{H^1}\mathcal{J}(T_\beta) \qquad \text{for } s \in [T_\beta, T_b] \tag{2.30b}$$

which preserves the continuity of the Sobolev gradient. Extraction of gradients in spaces of smoother functions, such as the Sobolev spaces considered here, is a well–known device in adjoint–based optimization of PDEs [38, 39] where it is often regarded as a form of preconditioning. We also emphasize that by changing the value of the length–scale parameter ℓ we can control the smoothness of the gradient $\nabla_k^{H^1}\mathcal{J}(k)$, and therefore also the relative smoothness of the resulting reconstruction of $k(T)$. More specifically, as it was shown in [38], a clear interpretation of this approach can be made in Fourier space. Using $\hat{\cdot}$ to denote the corresponding Fourier coefficient at wavenumber m and applying Fourier transform to either (2.28a) or (2.29a), we obtain

$$\widehat{\nabla_k^{H^1}\mathcal{J}} = \mathcal{F}_{lp}(m)\widehat{\nabla_k^{L_2}\mathcal{J}}, \tag{2.31}$$

where $\mathcal{F}_{lp}(m) \triangleq \dfrac{m_0^2}{m_0^2 + m^2}$ is a low–pass filter applied to the L_2 gradient with the quantity ℓ^{-2} representing the "cut-off" scale by setting $m_0 = 1/\ell$, cf. Figure 2.2.

In addition, both approaches described by (2.28) and (2.29)–(2.30) can be considered as a special case of *data extrapolation* in regard to reconstruction of the constitutive relations outside the identifiability region $\mathcal{I}$, as no additional measurement data is provided to construct Sobolev gradients $\nabla_k^{H^1}\mathcal{J}(k)$. In Section 2.6 we will compare the computational performance of the two approaches proposed and will discuss certain additional reasons why Sobolev

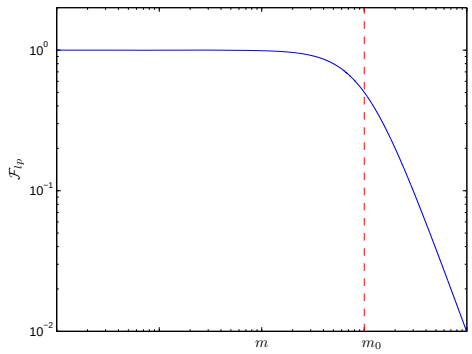

Figure 2.2: Interpretation of the preconditioning techniques (2.28)–(2.29) in Fourier space as a low–pass filter; m_0 represents the cut–off wavenumber $m_0 = 1/\ell$ [38].

gradients are a useful device for the present problem.

We finally conclude that iterative reconstruction of the constitutive relation $k(T)$ involves the computations described in Algorithm 1.

2.4 Reconstruction in the Presence of Measurement Noise

In this Section we discuss the important issue of reconstruction in the presence of noise in the measurements. As can be expected based on the general properties of parameter estimation problems [5], and as will be confirmed in Section 2.6.3, incorporation of random noise in the measurements leads to an instability in the form of small–scale oscillations appearing in the reconstructed constitutive relations. In the optimization framework a standard approach to mitigate this problem is Tikhonov regularization [40] in which original cost

Algorithm 1 Algorithm for reconstructing $k(T)$ on a single identifiability interval $\mathcal{I}$

- set $n = 0$
- set k_0 as the initial guess

repeat

- set $n = n + 1$
- obtain the solution for direct problem (2.3)
- obtain the solution for adjoint problem (2.14)
- compute the cost functional gradient $\boldsymbol{\nabla}_k^{L_2}\mathcal{J}(k^{(n)})$ following (2.24)
- compute the cost functional gradient $\boldsymbol{\nabla}_k^{H_1}\mathcal{J}(k^{(n)})$ following the preconditioning scheme (2.28) or (2.29)–(2.30)
- determine step length $\tau^{(n)}$ in (2.9) via line minimization
- update the reconstructed property $k^{(n)}$ following gradient descent algorithm (2.9)

until the termination condition on $k^{(n)}$ is satisfied

functional (2.6) is replaced with a regularized expression of the form

$$\mathcal{J}_\lambda(k) \triangleq \mathcal{J}(k) + \frac{\lambda}{2}\|k - \overline{k}\|^2_{\mathcal{Y}(I)}, \tag{2.32}$$

where $\lambda \in \mathbb{R}^+$ is an adjustable regularization parameter, $\overline{k}(T)$ represents a constitutive relation which our reconstruction $k(T)$ should not differ too much from, whereas $\|\cdot\|_{\mathcal{Y}(\mathcal{I})}$ is the Hilbert space norm in which we measure the deviation $(k - \overline{k})$. Thus, the regularization term in (2.32), i.e., the second one on the RHS, involves some additional information which needs to be specified a priori, namely, the choice of the reference constitutive relation $\overline{k}(T)$ and the space $\mathcal{Y}(\mathcal{I})$. As regards the reference function $\overline{k}(T)$, one natural possibility is to consider a constant value corresponding to a linearized version of constitutive relation (2.1). As regards the choice of the space $\mathcal{Y}(\mathcal{I})$, we will consider the following two possibilities:

1. $\mathcal{Y}(I) = L_2(\mathcal{I})$, so that the regularization term in (2.32) becomes ($\lambda = \lambda_1$)

$$\frac{\lambda_1}{2}\|k - \overline{k}\|^2_{L_2(I)} = \frac{\lambda_1}{2}\int_{T_\alpha}^{T_\beta}(k - \overline{k})^2 ds \tag{2.33}$$

yielding the following L_2 gradient of the regularized cost functional

$$\begin{aligned}\boldsymbol{\nabla}_k^{L_2}\mathcal{J}_{\lambda_1}(s) = &\int_\Omega \chi_{[T_\alpha, T(\mathbf{x})]}(s)\Delta T^* \, d\mathbf{x} \\ &- \int_{\partial\Omega} \chi_{[T_\alpha, T(\mathbf{x})]}(s)\frac{\partial T^*}{\partial n}\, d\sigma + \lambda_1(k - \overline{k}),\end{aligned} \tag{2.34}$$

2. $\mathcal{Y}(I) = \dot{H}^1(\mathcal{I})$, where $\dot{H}^1(\mathcal{I})$ denotes the Sobolev space equipped with the semi–norm $\|z\|_{\dot{H}^1(\mathcal{I})} \triangleq \int_{T_\alpha}^{T_\beta}\left(\frac{\partial z}{\partial s}\right)^2 ds$, $\forall_{z\in H^1(\mathcal{I})}$; the regularization term in (2.32) becomes ($\lambda = \lambda_2$)

$$\frac{\lambda_2}{2}\|k - \overline{k}\|^2_{\dot{H}^1(I)} = \frac{\lambda_2}{2}\int_{T_\alpha}^{T_\beta}\left(\frac{dk}{ds} - \frac{d\bar{k}}{ds}\right)^2 ds \tag{2.35}$$

yielding the following L_2 gradient of the regularized cost functional

$$\begin{aligned}\boldsymbol{\nabla}_k^{L_2}\mathcal{J}_{\lambda_2}(s) = &\int_\Omega \chi_{[T_\alpha, T(\mathbf{x})]}(s)\Delta T^* \, d\mathbf{x} \\ &- \int_{\partial\Omega} \chi_{[T_\alpha, T(\mathbf{x})]}(s)\frac{\partial T^*}{\partial n}\, d\sigma - \lambda_2\frac{d^2k}{ds^2}|_{s\in[T_\alpha, T_\beta]};\end{aligned} \tag{2.36}$$

we remark that in obtaining (2.36) integration by parts was applied to the directional derivative of the regularization term together with boundary conditions (2.29b).

Expressions (2.34) and (2.36) can now be used to obtain suitable Sobolev gradients as discussed in Section 2.3. Computational tests illustrating the performance of the two forms of the Tikhonov regularization on a problem with noisy data will be presented in Section 2.6.3. In that Section we will also

analyze the effect of the regularization parameters λ_1 and λ_2. We add that the stability and convergence of Tikhonov regularization using the Sobolev norm H^1 in the regularization term and applied to a very similar inverse problem was established rigorously in [19].

2.5 Shifting the Identifiability Interval

In Section 2.3 it was argued that the sensitivity of the cost functional $\mathcal{J}$ is essentially available on the identifiability interval $\mathcal{I}$ only, cf. Figure 2.1. The cost functional gradient may be formally extended outside this interval using the "extrapolation" techniques described at the end of Section 2.3, however, in the absence of additional measurement data these techniques merely ensure that the gradient is defined on the desired interval $\mathcal{L}$ and as such do not generate any new sensitivity information. Since, as demonstrated by our computational results reported in Section 2.6, such techniques are not capable of accurately reconstructing the relation $k(T)$ on an interval larger than the identifiability region, in the present Section we propose an approach to "shift" the identifiability region, so that the relation $k(T)$ can be reconstructed on a larger interval. We note that this method in fact cannot be related to any data extrapolation techniques discussed earlier, as it relies on the availability of additional experimental measurements corresponding to a suitably modified experimental set–up, such as the heat source distribution and boundary conditions. We also add that the "shifting" technique, described in detail below, may be hard to employed if there exist some limitations on generating new measurements in actual experiments.

In the limit, after performing several such shifts, the constitutive relation $k(T)$ can be reconstructed on the entire interval $\mathcal{L}$ which is of interest

in a given problem. The idea behind shifting the identifiability region is to modify the data, such as the RHS source term and the boundary conditions, in problem (2.3), so that the solution of the modified problem spans a shifted interval $\mathcal{I}_{(1)} = [T_\alpha + h, T_\beta + h]$, where $h \in \mathbb{R}$. Hereafter we will adhere to the convention that the indices enumerating shifts of the identifiability interval will appear as subscripts. This will allow us to distinguish them from the indices enumerating iterations in the solution of the optimization problem on a given identifiability region, cf. (2.9), which appear as superscripts. If the index representing the shifts of the identifiability region is skipped, the interval $\mathcal{I}_{(0)}$ is implied. Our approach is motivated by the following experimental procedure, described in Algorithm 2, designed to reconstruct the constitutive relation $k(T)$ on an interval $\mathcal{L}$ larger than an individual identifiability interval.

Algorithm 2 Algorithm for shifting the identifiability region $\mathcal{I}$

- apply the heat sources $g_{(0)}(\mathbf{x}) = g(\mathbf{x})$ and the boundary conditions $T_{0,(0)} = T_0$ to the actual experimental system and obtain the measurements $\tilde{T}_{(0)}(\mathbf{x})$, $\mathbf{x} \in \Sigma$; use these measurements to reconstruct $k(T)$ on the identifiability region $\mathcal{I}_{(0)} = \mathcal{I}$ using relations (2.9), (2.21), (2.29) and (2.30)
- set $j = 0$

repeat

- set $j = j + 1$
- determine new heat source distribution $g_{(j)}(\mathbf{x})$ and boundary conditions $T_{0,(j)}$
- apply the new heat source distribution and boundary conditions to the experimental system and obtain new measurements $\tilde{T}_{(j)}(\mathbf{x})$, $\mathbf{x} \in \Sigma$
- use the new measurements $\tilde{T}_{(j)}(\mathbf{x})$, $\mathbf{x} \in \Sigma$ to reconstruct $k(T)$ on a new identifiability interval $\mathcal{I}_{(j)}$ using (2.9), (2.21), (2.29) and (2.30)

until $\bigcup_{p=1}^{j} \mathcal{I}_{(p)} \supset \mathcal{L}$, i.e., until the union of all shifted identifiability regions $\mathcal{I}_{(0)}, \ldots, \mathcal{I}_{(j)}$ covers the interval $\mathcal{L}$ where we seek to reconstruct the constitutive relation

This sequence of steps is illustrated schematically in Figure 2.3. While all other elements of Algorithm 2 should be obvious, the goal of the present Section is to show how to choose the RHS source term $g_{(j)}(\mathbf{x})$ and the boundary condition $T_{0,(j)}$, so that the identifiability interval $\mathcal{I}_{(j)}$ will be approximately shifted by a prescribed value h. Let us suppose that $T_{(0)}$ is a known solution of problem (2.3) spanning the identifiability interval $\mathcal{I}_{(0)}$ which we now want to shift by $h > 0$. We thus obtain

$$-\boldsymbol{\nabla} \cdot \left[k(T_{(0)} + h)\, \boldsymbol{\nabla}(T_{(0)} + h)\right] = \; g_{(1)} \qquad \text{in } \Omega, \tag{2.37a}$$

$$T_{0,(0)} + h = T_{0,(1)} \qquad \text{on } \partial\Omega, \tag{2.37b}$$

which can be regarded as equations defining the new source distribution $g_{(1)}$ and new boundary condition $T_{0,(1)}$ required for this shift. Since the function $g_{(1)}$ depends on the magnitude h of the shift, for small values $|h| \ll 1$ we can bypass this inconvenience using the Taylor series expansion

$$k(T_{(0)}(\mathbf{x}) + h) = k\,\left(T_{(0)}(\mathbf{x})\right) + h\,\frac{dk}{dT}\,\left(T_{(0)}(\mathbf{x})\right) + \mathcal{O}(h^2) \tag{2.38}$$

which holds for all $\mathbf{x} \in \Omega$, so that (2.37a) becomes

$$-\boldsymbol{\nabla} \cdot \left[k\,\left(T_{(0)}\right)\,\boldsymbol{\nabla} T_{(0)}\right] - h\boldsymbol{\nabla} \cdot \left[\frac{dk}{dT}\,\left(T_{(0)}\right)\,\boldsymbol{\nabla} T_{(0)}\right] = g_{(1)} + \mathcal{O}(h^2). \tag{2.39}$$

Thus, the source distribution corresponding to the shifted identifiability region $\mathcal{I}_{(1)}$ can be approximated to the leading order as

$$g_{(1)}(\mathbf{x}) \approx g_{(0)}(\mathbf{x}) - h\Delta\left[k\,\left(T_{(0)}(\mathbf{x})\right)\right], \tag{2.40}$$

where $g_{(0)}(\mathbf{x})$ is the source distribution corresponding to the original ("un-

shifted") identifiability interval. Expression (2.40) can be used in Algorithm 2 employing the most up–to–date estimate of the relation $k(T)$ resulting in

$$g_{(j+1)}(\mathbf{x}) \approx g_{(j)}(\mathbf{x}) - h\Delta\left[k_{(j)}\ \left(T_{(j)}(\mathbf{x})\right)\right]. \tag{2.41}$$

We note that in general the distance h may be allowed to vary from one shift to another. Shifting the identifiability interval has the effect of generating the sensitivity information over a different range of the state variable T. This might potentially have a detrimental effect on the reconstruction of $k(T)$ obtained on "earlier" identifiability intervals. In order for the reconstructions carried out on shifted intervals $\mathcal{I}_{(j)}$, $j \geq 1$, not to destroy the earlier reconstructions on $\mathcal{I}_{(0)}, \ldots, \mathcal{I}_{(j-1)}$, optimization on shifted intervals will be performed using a cost functional augmented with a Tikhonov–type penalty term, namely,

$$\mathcal{J}_{(j)}(k) \triangleq \mathcal{J}(k) + \frac{\gamma}{2}\int_{T_{\alpha,(0)}}^{T_{\beta,(j-1)}-\delta}[k(s) - k_{(j-1)}(s)]^2 ds, \tag{2.42}$$

where $\mathcal{J}(k)$ is defined in (2.6) and $\gamma, \delta \in \mathbb{R}^+$ are parameters. The purpose of including this additional term is to ensure that the reconstruction performed on the new (shifted) identifiability interval $\mathcal{I}_{(j)}$ preserves the estimate already constructed on the union of the previous intervals $\mathcal{I}_{(0)}, \ldots, \mathcal{I}_{(j-1)}$. It will also have the additional effect of regularizing the reconstruction procedure against measurement noise (cf. Section 2.4). We remark that if all the measurements $\{\tilde{T}_{(j)}\}_{j=1}^{P}$ were available from the beginning, then at least in principle one could consider an alternative approach based on solution of a single optimization problem on the union $\bigcup_{j=1}^{P}\mathcal{I}_j$ of all identifiability intervals. However, the difficulty with such an approach is that there would not be unique heat sources and boundary conditions defined on the composite identifiability interval. The

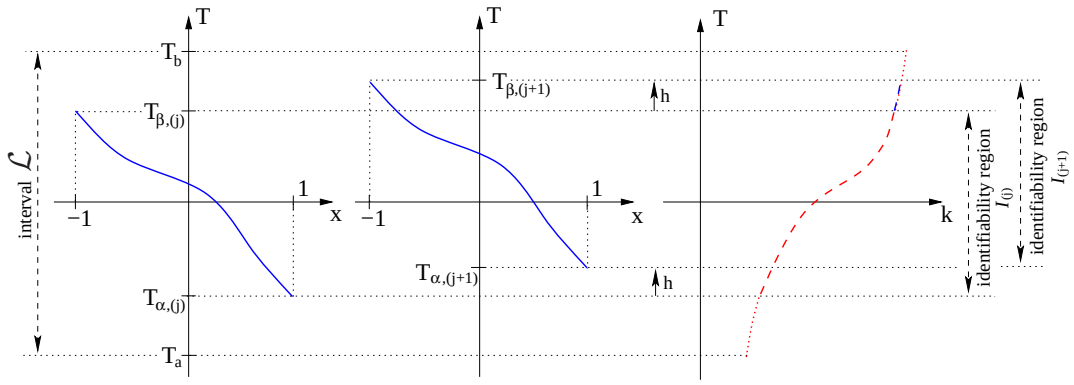

Figure 2.3: Schematic illustrating the procedure for shifting the identifiability region. Notation is the same as in Figure 2.1. The left and middle graphs correspond to reconstructions performed at two consecutive intervals $\mathcal{I}_{(j)}$ and $\mathcal{I}_{(j+1)}$.

methodology proposed in this Section is in our opinion well suited for an actual experimental procedure, as the experimental conditions (represented by the heat sources $g_{(j)}(\mathbf{x})$ and boundary conditions $T_{0,(j)}$) are adjusted in an *adaptive* fashion devised to produce temperature measurements in a desired identifiability region. Computational results illustrating Algorithm 2 combined with update formula (2.41) and augmented functional (2.42) will be presented in Section 2.6.4.

2.6 Computational Results

In this Section we describe the computational results obtained with our proposed method. Following a brief description of the numerical approaches used to solve the governing and the adjoint problem, we present some diagnostic tests concerning computation of the gradient at a given iteration. Next, we present the solution of the parameter estimation problem on a single identifiability interval with and without noise. Finally, we discuss the solution of a

sequence of parameter estimation problems on a set of identifiability regions shifted with respect to each other using the algorithm described in Section 2.5. For the sake of simplicity, our sample computations will be performed for a one–dimensional (1D) version of problem (2.3) with $\Omega = (-1, 1)$.

Governing system (2.3) and adjoint system (2.14) are discretized on a uniform grid with $N_x = 100$ grid points using the second–order central differences combined with the cubic spline interpolation of the function $k(T(x))$. For the purpose of this interpolation the interval $\mathcal{L}$ is discretized using an equispaced grid with $N_T = 200$ points, unless stated otherwise. The actual constitutive relation we seek to reconstruct is given by the function

$$\tilde{k}(T) = \arctan(T - 2.5) + b, \quad b = 2, \tag{2.43}$$

whose locally steep slope makes it representative of a range of constitutive relations typically encountered in thermodynamic systems. In parallel with discretization of the governing PDE, we also discretize the continuous measurements using pointwise measurement data which is typically available in actual experiments. We will assume that such pointwise measurements, denoted $\{\tilde{T}_i\}_{i=1}^M$, are available at a set of measurement points $\{\mathbf{x}_i\}_{i=1}^M$. We will in addition assume that the sensing domain can be regarded as a union $\Sigma = \bigcup_{i=1}^M \Sigma_i$ of disjoint subdomains $\Sigma_i \ni \mathbf{x}_i$, $i = 1, \ldots, M$, whose sizes $|\Sigma_i|$ are of the order of the grid size $\Delta x = \frac{2}{N_x - 1}$, so that $\int_{\Sigma_i} [\tilde{T}(\mathbf{x}) - T(\mathbf{x})]^2 \, d\mathbf{x} \approx [\tilde{T}(\mathbf{x}) - T(\mathbf{x})]^2 \, |\Sigma_i|$, $i = 1, \ldots, M$ (see Figure 2.4). In the computational tests reported below we used $M = 10$ (tests performed with different values of M yielded qualitatively similar results). To mimic an actual experimental procedure, on each identifiability interval $\mathcal{I}_{(j)}$, $j > 0$, relation (2.43) is used in combination with governing system (2.3) to obtain pointwise measurements $\{\tilde{T}_{i,(j)}\}_{i=1}^M$. Relation (2.43) is

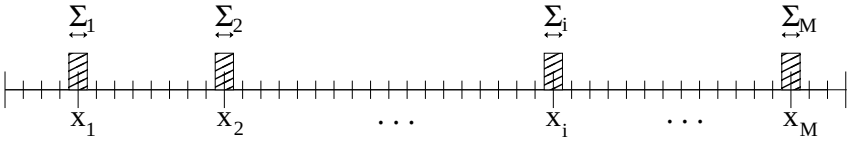

Figure 2.4: Schematic showing discretization of continuous measurements $\tilde{T}(\mathbf{x})$, $\mathbf{x} \in \Sigma$ with pointwise measurements available at the discrete points $\mathbf{x}_1, \ldots, \mathbf{x}_M$. Hatched areas represent the individual sensing domains Σ_i, $i = 1, \ldots, M$.

then "forgotten" and is reconstructed using gradient–based algorithm (2.9) on a single (Section 2.6.2), or several identifiability intervals (Section 2.6.4). We also notice that for the sake of simplicity all our computations used equispaced measurement locations $\{\mathbf{x}_i\}_{i=1}^{M}$ which coincide with the grid points of the discretized domain Ω. In a general case one may consider more flexibility in choosing sensor locations. One may also consider the question of determining optimal locations of the measurement points. While this problem is outside the scope of the present work, it might be worthwhile to consider it in future research.

While in the calculations validating our basic formulation (presented in Sections 2.6.1, 2.6.2 and 2.6.4) no noise was present in the measurements, its effect is addressed systematically in Section 2.6.3. In terms of the initial guess on the first identifiability region $\mathcal{I}_{(0)}$ we take a constant approximation k_0 to (2.43), whereas for the reconstruction problems on the shifted identifiability regions $\mathcal{I}_{(j)}$ we take $\hat{k}_{(j-1)}(T)$, i.e., the approximation of the constitutive relation obtained with the data on the interval $\mathcal{I}_{(j-1)}$. The initial distribution of the heat sources was $g_{(0)} = -\frac{(e^x-2x)^2}{1+(e^x-x^2-0.5)^2} - [\arctan(e^x - x^2 - 0.5) + 2]\,(e^x - 2)$ resulting in the identifiability region $\mathcal{I}_{(0)} = [1.3679, 3.7183]$. The interval over which we seek to reconstruct the constitutive relation is $\mathcal{L} = [0, 5.0862]$.

2.6.1 Validation of Gradients

In this Section we present results demonstrating the consistency of the cost functional gradients obtained with the approach described in Section 2.3. In Figure 2.5 we present the L_2 and several Sobolev H^1 gradients obtained at the first iteration. In the first place, we observe that as discussed in Section 2.3 the L_2 gradients do indeed exhibit discontinuities which makes them unsuitable for the reconstruction of constitutive relations with required properties, cf. (2.4). On the other hand, the gradients extracted in the Sobolev space H^1 are characterized by the required smoothness and therefore hereafter we will solely use the Sobolev gradients. We also observe that the two techniques for extending the gradients discussed in Section 2.3 [equations (2.28) and (2.29)–(2.30)] result in quite different behavior of the Sobolev gradients outside the identifiability region $\mathcal{I}$. These different behaviors will result in different quality of reconstruction of the constitutive relation. Next, in Figure 2.6 we present the results of a diagnostic test commonly employed to verify the correctness of the cost functional gradient [43]. It consists in computing directional differential (2.12) in two different ways, namely, using a finite–difference approximation and using the adjoint field, and then examining the ratio of the two results

$$\kappa(\epsilon) \triangleq \frac{\epsilon^{-1}\left[\mathcal{J}(k+\epsilon k') - \mathcal{J}(k)\right]}{\int_{T_a}^{T_b} \boldsymbol{\nabla}_k \mathcal{J}(s)\, k'(s)\, ds} \tag{2.44}$$

for a range of values of ϵ. We emphasize that in view of Riesz identity (2.12) it does not matter which inner product (i.e., L_2 vs. H^1) is adopted in the expression in the numerator in (2.44). If the gradient $\boldsymbol{\nabla}_k \mathcal{J}(k)$ is computed correctly, then for intermediate values of ϵ, $\kappa(\epsilon)$ should be close to the unity. Remarkably, this behavior can be observed in Figure 2.6 over a range of ϵ

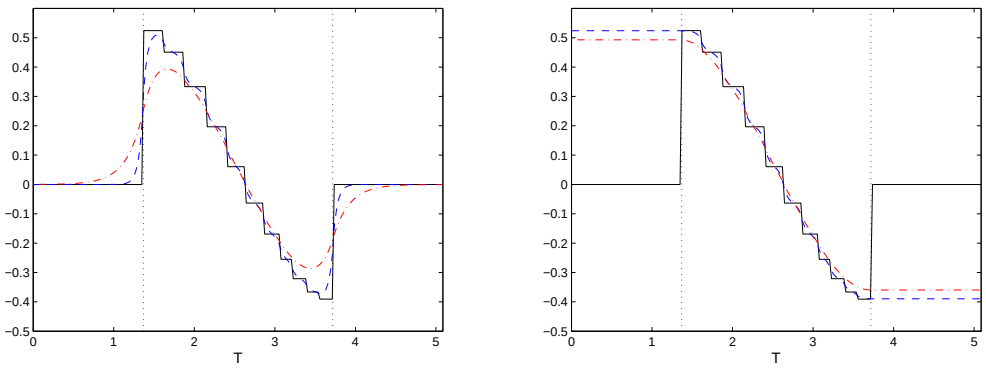

(a) (b)

Figure 2.5: Comparison of (solid line) the L_2 gradient $\boldsymbol{\nabla}^{L_2}\mathcal{J}$ and the Sobolev gradients $\boldsymbol{\nabla}^{H^1}\mathcal{J}$ defined (a) in (2.28) and (b) in (2.29)–(2.30) for different values of the smoothing coefficient (dashed line) $\ell = 0.05$ and (dash–dotted line) $\ell = 0.2$ at the first iteration with the initial guess $k_0 = const = 2.13$. The vertical dotted lines represent the boundaries of the identifiability interval $\mathcal{I}_{(0)}$.

spanning about 10 orders of magnitude for two different perturbations $k'(T)$. Furthermore, we also emphasize that refining the discretization of the interval $\mathcal{L}$ yields values of $\kappa(\epsilon)$ much closer to the unity. As can be expected, the quantity $\kappa(\epsilon)$ deviates from the unity for very small values of ϵ, which is due to the subtractive cancelation (round–off) errors, and also for large values of ϵ, which is due to the truncation errors.

2.6.2 Reconstruction on a Single Identifiability Interval

We solve minimization problem (2.7) using the BFGS (Broyden–Fletcher–Goldfarb–Shanno) algorithm [33] and, unless indicated otherwise, Sobolev gradients computed with $\ell = 0.2$ which was found by trial–and–error to maximize the rate of convergence of iterations (2.9). The termination condition used

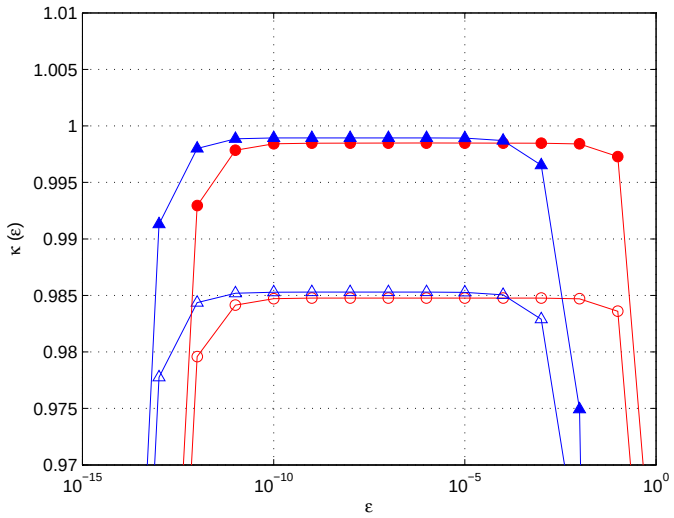

Figure 2.6: The behavior of $\kappa(\epsilon)$ for different perturbations (circles) $k'(T) = \exp(-T^2/10)$ and (triangles) $k'(T) = -0.1T^2 + 10$ using different discretizations of the interval $\mathcal{L}$: (empty symbols) $N_T = 200$ and (filled symbols) $N_T = 2000$.

was $\left|\frac{\mathcal{J}(k^{(n)})-\mathcal{J}(k^{(n-1)})}{\mathcal{J}(k^{(n-1)})}\right| < 10^{-6}$. The behavior of the cost functional $\mathcal{J}(k^{(n)})$ as a function of the iteration count n is shown in Figure 2.7a for the Sobolev gradients defined in (2.28) and in (2.29)–(2.30). We note that while in both cases a decrease over several orders of magnitude is observed in just a few iterations, in the first case the cost functional eventually drops to very small values. The effect of the different values of the constant initial guess k_0 on the decrease of the cost functional is illustrated in Figure 2.7b. We note that the cost functional $\mathcal{J}(k^{(n)})$ decreases rapidly for all investigated values of the constant k_0, although the iterations saturate at different levels. It is interesting to observe that the best results were obtained for the initial guess $k_0 = \frac{1}{M}\sum_{i=1}^{M} \tilde{k}(\tilde{T}_i) = 2.1499$ which is the algebraic mean of the values of the true constitutive relation $\tilde{k}(T)$ evaluated at the "measured" temperatures. Reconstructions $\hat{k}(T)$ of the constitutive relation obtained using the Sobolev gradients defined in (2.28) and in (2.29)–(2.30) are shown in Figures 2.8 and 2.9, respectively. We note that while the quality of the reconstruction on the identifiability region $\mathcal{I}$ is comparable in the two cases, outside the identifiability region the second approach clearly offers superior accuracy. In Figure 2.10 we show the reconstructions $\hat{k}(T)$ of the constitutive relation obtained for different values of the constant initial guess k_0 (the same values as used in Figure 2.7b). We conclude that, since the reconstructed relations are quite different, the iterations starting from different initial guesses converge in fact to different local minimizers. However, these differences notwithstanding, all reconstructions shown in Figure 2.10 capture the main features of the true constitutive relation (2.43). We also emphasize that there is a range of values of the initial guess k_0 for which the quality of reconstruction is excellent (cf. Figure 2.9 and 2.10d). Next, in Figure 2.11a we show the solutions $T(x;k)$ to problem (2.3)

corresponding to the reconstructed conductivity $\hat{k}(T)$, cf. Figure 2.9, and the true conductivity $\tilde{k}(T)$, cf. (2.43), together with the measurements $\{\tilde{T}_i\}_{i=1}^{10}$ used as data in the solution of the problem. We note excellent agreement of the solutions obtained based on the reconstructed and measured constitutive relations. Since the solutions $T(x)$ corresponding to the reconstructed and true constitutive relations cannot be distinguished in Figure 2.11a, in Figure 2.11b we show the error $|T(x;\hat{k}) - T(x;\tilde{k})|$ corresponding to the reconstruction $\hat{k}$ obtained using the two definitions of the Sobolev gradients given in Section 2.3. Finally, we remark that, although the Sobolev gradients defined in (2.28) resulted in a larger decrease of the cost functional in Figure 2.7a and smaller errors evident in Figure 2.11b, this is in fact offset by the more favorable behavior of the Sobolev gradients defined in (2.29)–(2.30) outside the identifiability region. Thus, this second approach will be used in the sequel to perform reconstruction on shifted identifiability regions.

2.6.3 Reconstruction in the Presence of Noise

In this Section we first assess the effect of noise on the reconstruction without Tikhonov regularization and then study the efficiency of the regularization techniques introduced in Section 2.4. In Figure 2.12 we revisit the case presented first in Figure 2.9, now for measurements contaminated with 1%, 3%, 5% and 10% uniformly distributed noise and without Tikhonov regularization. To incorporate noise, say of ξ%, into the measurements $\{\tilde{T}_i\}_{i=1}^{M}$, we replace these measurements with a new set $\{\tilde{T}_i^{\xi}\}_{i=1}^{M}$, where the random variables $\tilde{T}_i^{\xi}$ have a uniform distribution with the mean $\tilde{T}_i$ and the standard deviation $\Delta\xi = \dfrac{1}{M}\sum_{i=1}^{M}\tilde{T}_i \cdot \dfrac{\xi}{100\%}$. As expected, we see that increasing levels of noise lead to oscillatory instabilities developing in the reconstructed con-

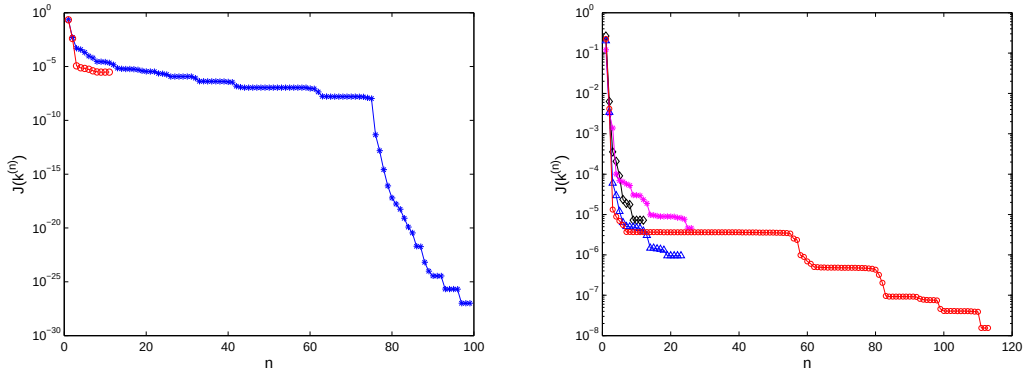

(a) (b)

Figure 2.7: (a) Decrease of the cost functional $\mathcal{J}(k^{(n)})$ with iterations n using the Sobolev gradient $\boldsymbol{\nabla}^{H^1}\mathcal{J}$ defined (asterisks) in (2.28) and (circles) in (2.29)–(2.30) with $\ell = 0.2$; the initial guess was $k_0 = 2.13$, (b) decrease of the cost functional $\mathcal{J}(k^{(n)})$ with iterations n for different initial guesses: (diamonds) $k_0 = 2.5$, (asterisks) $k_0 = 1.5$, (triangles) $k_0 = 2$, and (circles) $k_0 = \dfrac{1}{M}\sum_{i=1}^{M}\tilde{k}(\tilde{T}_i) = 2.1499$ obtained with the Sobolev gradients defined in (2.29)–(2.30).

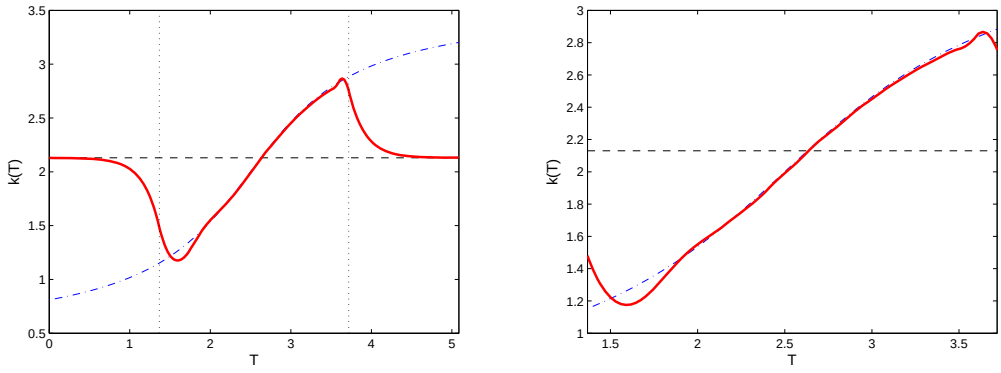

(a) (b)

Figure 2.8: Reconstruction $\hat{k}(T)$ of the constitutive relation obtained using the Sobolev gradients defined in (2.28) on (a) the interval $\mathcal{L}$ and (b) close–up view showing the identifiability interval $\mathcal{I}_{(0)}$. The dash–dotted line represents the true constitutive relation (2.43), the solid line is the reconstruction, whereas the dashed line represents the initial guess $k_0 = 2.13$; the vertical dotted lines in the figure on the left represent the boundaries of the identifiability interval $\mathcal{I}_{(0)}$.

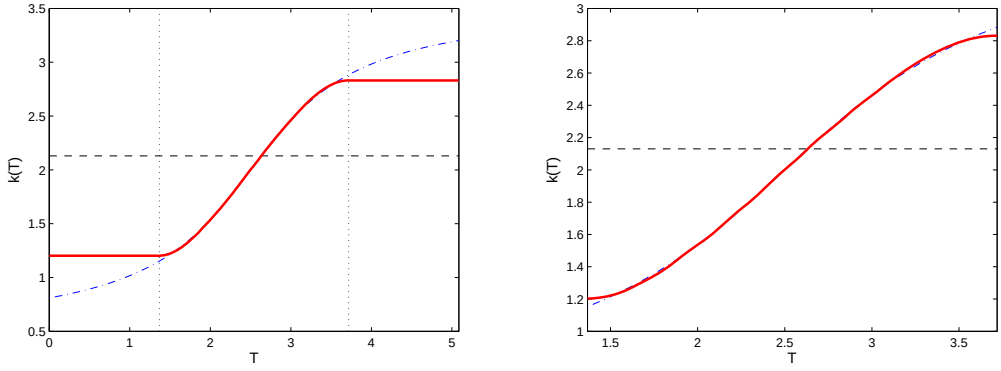

(a) (b)

Figure 2.9: Reconstruction $\hat{k}(T)$ of the constitutive relation obtained using the Sobolev gradients defined in (2.29)–(2.30) on (a) the interval $\mathcal{L}$ and (b) close–up view showing the identifiability interval $\mathcal{I}_{(0)}$. The dash–dotted line represents the true constitutive relation (2.43), the solid line is the reconstruction, whereas the dashed line represents the initial guess $k_0 = 2.13$; the vertical dotted lines in the figure on the left represent the boundaries of the identifiability interval $\mathcal{I}_{(0)}$.

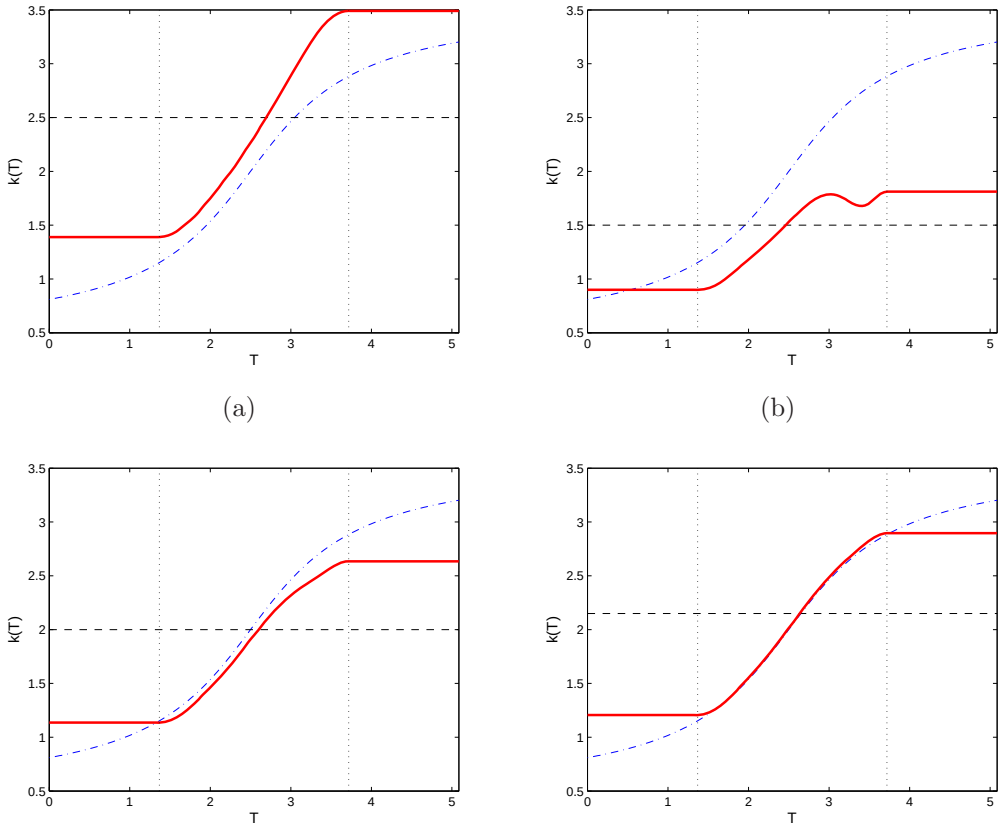

Figure 2.10: Reconstruction $\hat{k}(T)$ of the constitutive relation obtained using different initial guesses (a) $k_0 = 2.5$, (b) $k_0 = 1.5$, (c) $k_0 = 2$ and (d) $k_0 = \frac{1}{M}\sum_{i=1}^{M} \tilde{k}(\tilde{T}_i) = 2.1499$, and the Sobolev gradients defined in (2.29)–(2.30). The dash–dotted lines represent the true constitutive relation (2.43), the solid lines are the reconstructions, whereas the dashed lines represent initial guesses; the vertical dotted lines represent the boundaries of the identifiability interval $\mathcal{I}_{(0)}$.

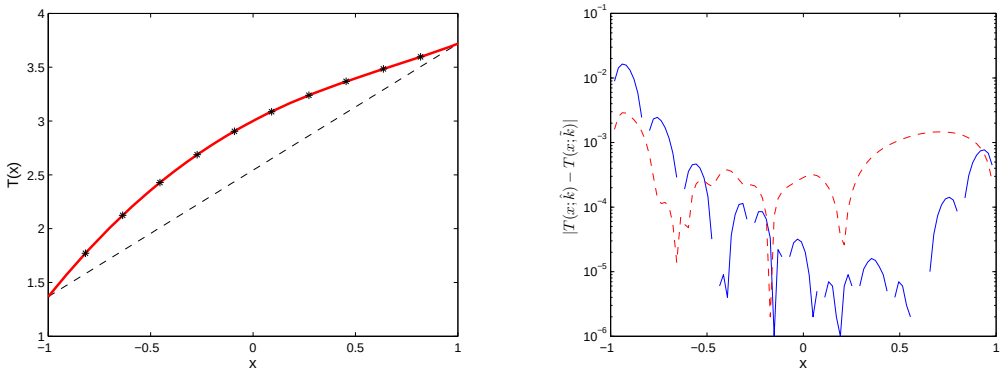

(a) (b)

Figure 2.11: (a) Solution $T(x,k)$ of governing equation (2.3) corresponding to (solid line) the reconstructed constitutive relation $\hat{k}$, (dashed line) the initial guess $k_0 = 2.13$, and (dash–dotted line) the true constitutive relation $\tilde{k}$; asterisks represent the measurement data $\{\tilde{T}_i\}_{i=1}^{10}$, (b) the error $|T(x;\hat{k}) - T(x;\tilde{k})|$ between the solution of governing equation (2.3) corresponding to $\hat{k}$ obtained using the Sobolev gradients defined (solid line) in (2.28) and (dashed line) in (2.29)–(2.30), and the solution corresponding to the true constitutive relation (2.43). Irregularity visible in Figure (b) is an artefact of "log–log" plotting at the points where the error $|T(x;\hat{k}) - T(x;\tilde{k})|$ becomes close to zero.

stitutive relations $k(T)$. We further observe that this instability is somewhat less pronounced in reconstructions performed with "smoother" gradients [i.e., corresponding to larger values of the length–scale parameter ℓ in (2.29a)]. This regularizing effect of the Sobolev gradients was already discussed in [38].

The effect of the Tikhonov regularization is studied in Figure 2.13 where we illustrate the performance of the two techniques described in Section 2.4, cf. (2.33) and (2.35), on the reconstruction problem with 10% noise in the measurement data (i.e., the "extreme" case presented in Figure 2.12). We conclude that regularization with the Sobolev $\dot{H}^1(\mathcal{I})$ term tends to give somewhat better results than regularization with the L_2 term, cf. Figures 2.13(a,b) and 2.13(c,d). In both cases, with increasing values of the regularization parameters λ_1 and λ_2 the reconstructed constitutive relations become smoother at the price however of larger reconstruction errors which is a well–known trade–off involved in Tikhonov regularization. Systematic methods for determining optimal values of regularization parameters are discussed for instance in [40–42]. Finally, in Figure 2.14 we present the relative reconstruction errors $\|\hat{k} - \tilde{k}\|_{L_1(\mathcal{I})} \,/\, \|\tilde{k}\|_{L_1(\mathcal{I})}$ obtained using the approaches discussed in Section 2.4 for data with different noise levels and averaged over 100 noise samples. We note that on the whole regularization with the Sobolev $\dot{H}^1(\mathcal{I})$ term performs slightly better than regularization with the $L_2(\mathcal{I})$ term. Reconstructions employing the Sobolev gradients alone with no Tikhonov regularization produce significantly poorer results especially for larger noise amplitudes. We close this Section by concluding that Tikhonov regularization performs as expected in problems with significant noise levels in the measurement data. To improve the performance further one may use

- different norms $\|\cdot\|_{\mathcal{Y}(\mathcal{I})}$ in (2.32),

- different reference fields $\bar{k}(T)$ and
- more rigorously chosen regularization parameters λ, cf. [40–42].

2.6.4 Reconstruction on Shifted Identifiability Intervals

In this Section we implement the approach for shifting the identifiability region described in Section 2.5. We reiterate that the goal is to extend the range of the state variable T on which one can accurately reconstruct the constitutive relation so as to cover the entire interval $\mathcal{L}$. As implied by Algorithm 2, we do this by solving a sequence of reconstruction problems, each with the cost functional, the RHS source term and boundary conditions in governing equation (2.3) chosen as described in Section 2.5. From the practical point of view, this mimics performing a sequence of laboratory experiments, each in suitably chosen conditions represented by $g_{(j)}$ and $T_{0,(j)}$, to generate the data for the reconstruction process on different identifiability intervals. Results obtained with this approach and performing shifts in one direction only, i.e., towards larger values of T, are shown in Figures 2.15 and 2.16 for $P = 12$ and $P = 50$ shifts, respectively. The shifts were performed assuming $h = 0.1$ in (2.41) and $\gamma = 12$ in (2.42). The parameter δ in (2.42) was equal to 6% and 3% of the width of the current identifiability interval respectively in the problems with 12 and 50 shifts. All of these parameters were chosen empirically to maximize the quality of the reconstruction. We observe that, as compared to the reconstruction performed on $\mathcal{I}_{(0)}$ only, now a good estimate of the constitutive relation $k(T)$ is obtained for a much broader range of T, although the quality of this reconstruction slowly degrades as the number of shifts is increased. Moreover, as is evident from Figures 2.9b, 2.15c, and 2.16c, this is achieved at the cost of a

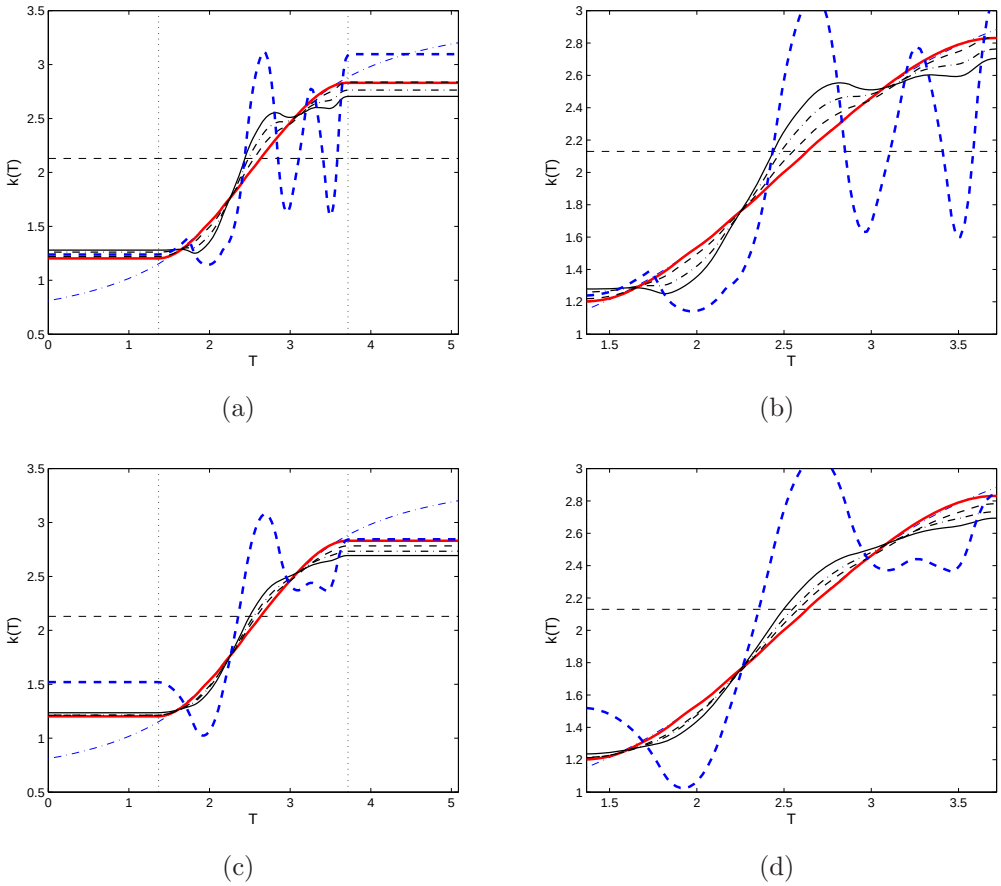

Figure 2.12: Reconstruction $\hat{k}(T)$ of the constitutive relation obtained using the Sobolev gradients defined in (2.29)–(2.30) with (a,b) $\ell = 0.2$ and (c,d) $\ell = 0.4$ and different noise levels in the measurement data: (thick solid line) no noise, (dashed line) 1%, (dash–dotted line) 3%, (thin solid line) 5%, and (thick dashed line) 10%. The dashed horizontal line represents the initial guess $k_0 = 2.13$, whereas the vertical dotted lines in the figures on the left represent the boundaries of the identifiability interval $\mathcal{I}_{(0)}$. Figures (a) and (c) correspond to the interval $\mathcal{L}$, whereas figures (b) and (d) show a close–up view of the identifiability interval $\mathcal{I}_{(0)}$.

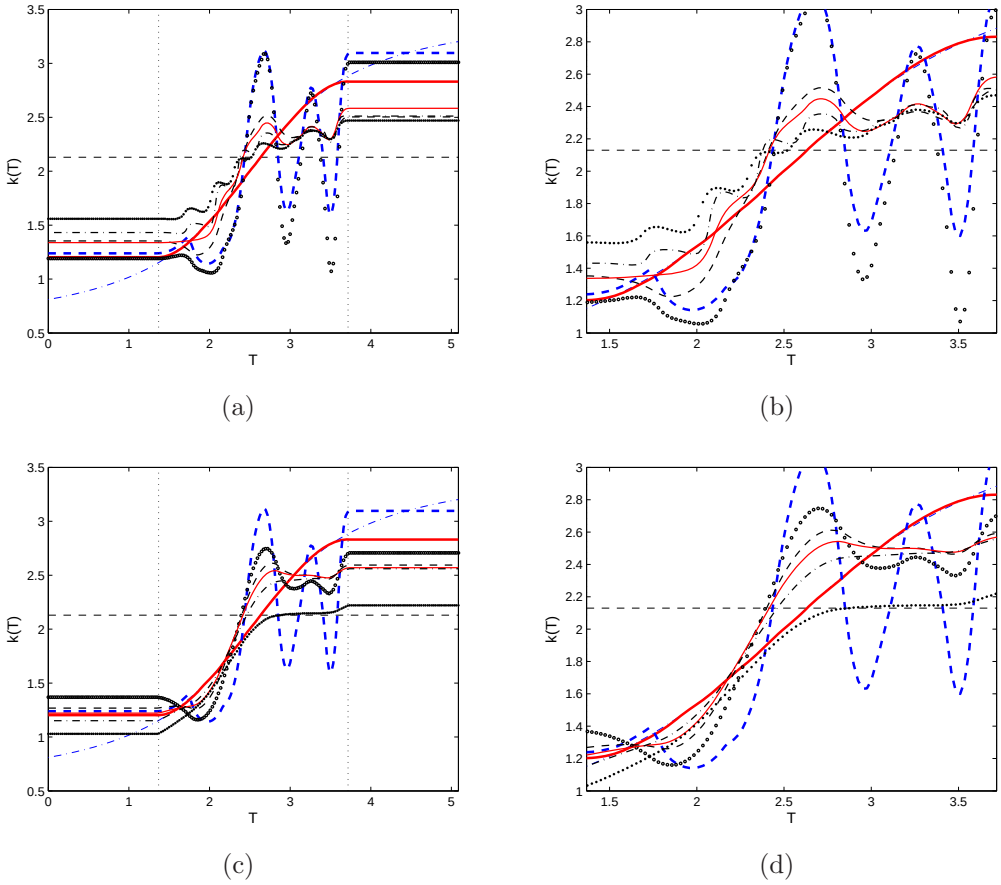

Figure 2.13: Effect of Tikhonov regularization on the reconstruction from the measurement data with 10% noise using (a,b) regularization term (2.33) and (c,d) regularization term (2.35). In Figures (a) and (b) the following values of the regularization parameter were used: (thick dashed line) $\lambda_1 = 0$, (circles) $\lambda_1 = 0.01$, (dashed line) $\lambda_1 = 0.05$, (thin solid line) $\lambda_1 = 0.1$, (dash–dotted line) $\lambda_1 = 0.2$, and (dots) $\lambda_1 = 0.4$. In Figures (c) and (d) the following values of the regularization parameter were used: (thick dashed line) $\lambda_2 = 0$, (circles) $\lambda_2 = 0.001$, (dashed line) $\lambda_2 = 0.003$, (thin solid line) $\lambda_2 = 0.005$, (dash–dotted line) $\lambda_2 = 0.01$, and (dots) $\lambda_2 = 0.02$. The dashed horizontal line represents the initial guess $k_0 = 2.13$, whereas the vertical dotted lines in the figures on the left represent the boundaries of the identifiability interval $\mathcal{I}_{(0)}$. Figures (a) and (c) correspond to the interval $\mathcal{L}$, whereas figures (b) and (d) show a close–up view of the identifiability interval $\mathcal{I}_{(0)}$.

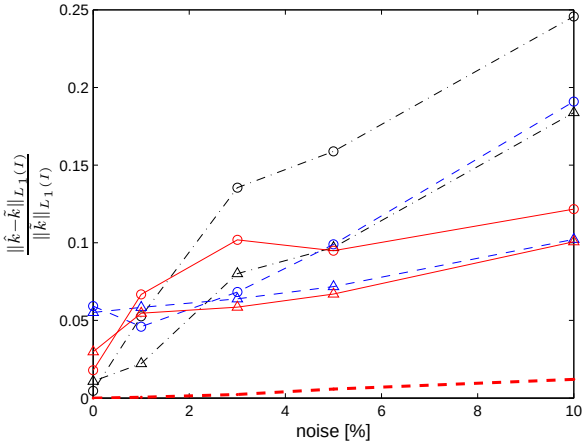

Figure 2.14: Relative L_1 reconstruction errors $\|\hat{k} - \tilde{k}\|_{L_1(\mathcal{I})} / \|\tilde{k}\|_{L_1(\mathcal{I})}$ obtained in the presence of noise with the amplitude indicated and averaged over 100 samples: (dash–dotted line) reconstruction with Sobolev gradients and without Tikhonov regularization [(circles) $\ell = 0.2$, (triangles) $\ell = 0.4$], (dashed line) reconstruction with L_2 Tikhonov regularization term (2.33) [(circles) $\lambda_1 = 0.01$, (triangles) $\lambda_1 = 0.1$], and (solid line) reconstruction with $\dot{H}^1$ Tikhonov regularization term (2.35) [(circles) $\lambda_2 = 0.005$, (triangles) $\lambda_2 = 0.003$]. The thick dashed line represents the "error" in the exact constitutive relation (2.43) obtained by adding noise to T.

slight deterioration of the final reconstruction $\hat{k}_{(P)}(T)$ on the original identifiability interval $\mathcal{I}_{(0)}$ as compared to the reconstruction $\hat{k}_{(0)}(T)$ obtained without any shifts. Finally, in Figure 2.17 we present the reconstruction $\hat{k}_{(2P)}(T)$ of the constitutive relation obtained by shifting the identifiability region in both directions. This is achieved by performing the shifts towards larger and smaller values of T in an interchanging manner. The parameters used were $h = 0.1$, $\gamma = 8$ and $\delta = 4\% \times$ [width of the current identifiability region]. We observe that in this problem as well good reconstruction of the constitutive relation $k(T)$ was obtained on the entire interval $\mathcal{L}$.

2.7 Summary of Results for the Simplified Model

In this Chapter we investigated a novel computational approach to reconstruction of constitutive relations based on incomplete measurement data. This parameter estimation problem is solved using a gradient–based optimization technique in which the sensitivities of the cost functional with respect to the form of the constitutive relation are computed using a suitably–defined adjoint system. We studied the problem in the context of the "optimize–then–discretize" approach to PDE–constrained optimization and demonstrated how using the Kirchhoff transformation one can obtain an expression of the cost functional gradient more convenient from the computational point of view than derived in earlier studies [11]. We also argued that the traditional L_2 cost functional gradients are discontinuous and therefore unsuitable for reconstruction of smooth constitutive relations. It was shown that this difficulty can be resolved by using the Sobolev gradients defined consistently with the functional setting of the problem in the optimization algorithm. Finally, we proposed and validated a procedure allowing one to shift the identifiability re-

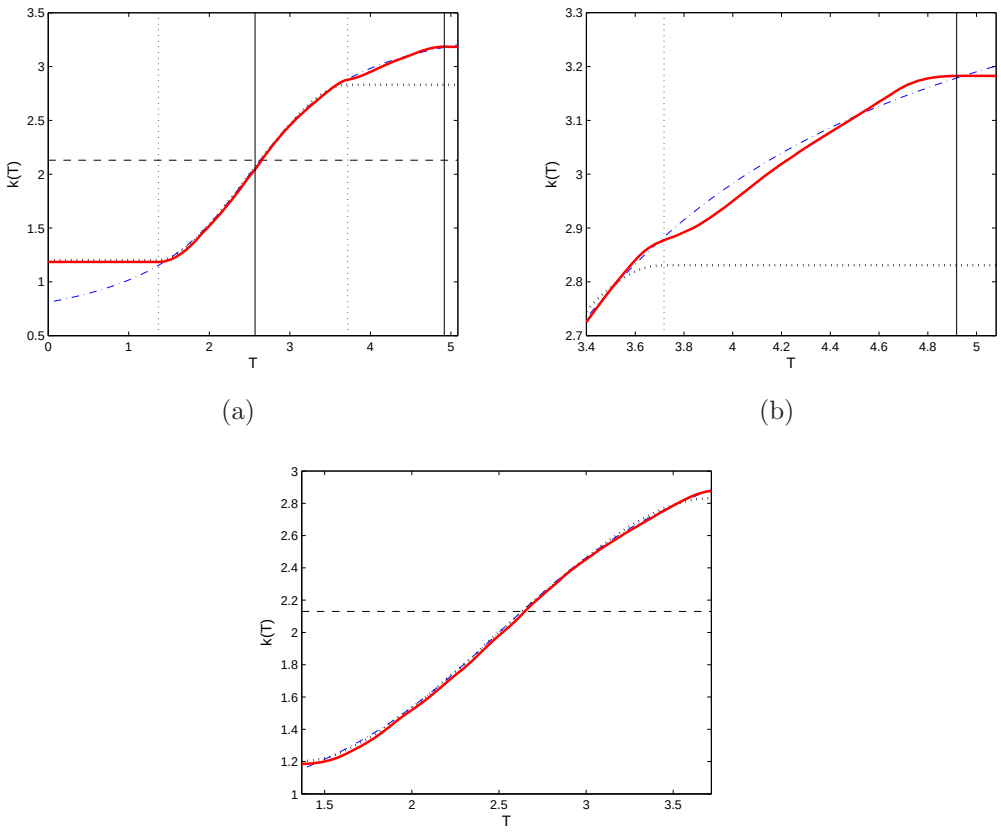

Figure 2.15: Reconstruction $\hat{k}_{(P)}(T)$ of the constitutive relation on an union of $P = 12$ shifted identifiability regions: (a) the interval $\mathcal{L}$, (b) magnification of the region where the different identifiability intervals overlap, and (c) the initial identifiability interval $\mathcal{I}_{(0)}$. The dash–dotted line represents the true constitutive relation (2.43), the solid line is the reconstruction $\hat{k}_{(P)}(T)$ after $P = 12$ shifts, whereas the dotted line represents the reconstruction $\hat{k}_{(0)}(T)$ obtained without any shifts; the vertical lines represent the boundaries of (dotted) the interval $\mathcal{I}_{(0)}$ and (solid) the interval $\mathcal{I}_{(12)}$.

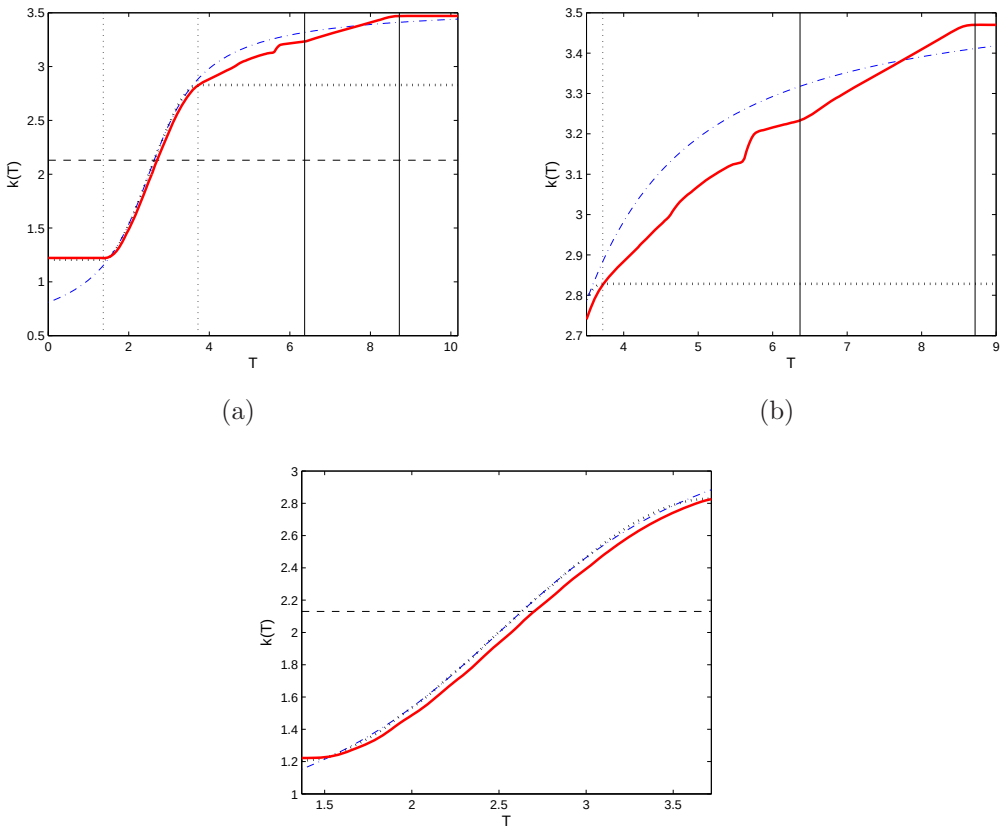

Figure 2.16: Reconstruction $\hat{k}_{(P)}(T)$ of the constitutive relation on an union of $P = 50$ shifted identifiability regions: (a) the interval $\mathcal{L}$, (b) magnification of the region where the different identifiability intervals overlap, and (c) the initial identifiability interval $\mathcal{I}_{(0)}$. The dash–dotted line represents the true constitutive relation (2.43), the solid line is the reconstruction $\hat{k}_{(P)}(T)$ after $P = 50$ shifts, whereas the dotted line represents the reconstruction $\hat{k}_{(0)}(T)$ obtained without any shifts; the vertical lines represent the boundaries of (dotted) the interval $\mathcal{I}_{(0)}$ and (solid) the interval $\mathcal{I}_{(50)}$.

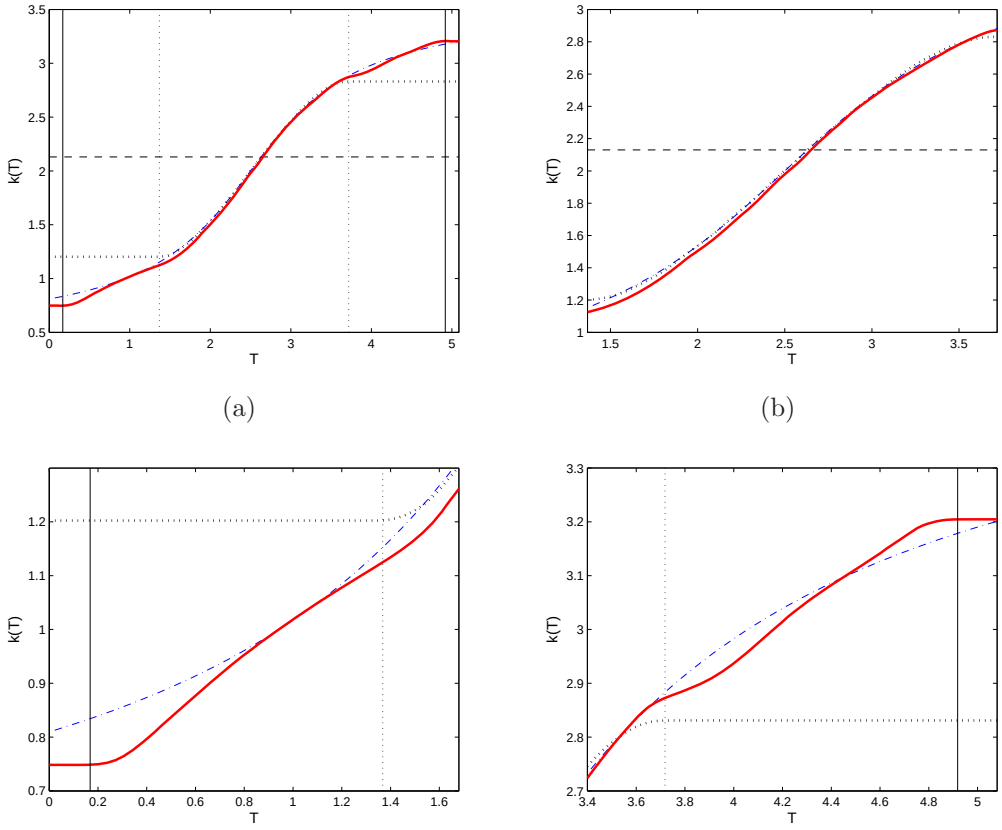

Figure 2.17: Reconstruction $\hat{k}_{(2P)}(T)$ of the constitutive relation obtained with the original identifiability region shifted interchangeably towards larger and smaller values of T: (a) interval $\mathcal{L}$, (b) the initial identifiability interval $\mathcal{I}_{(0)}$, and (c,d) magnification of the regions where the different identifiability intervals overlap. The dash–dotted line represents the true constitutive relation (2.43), the solid line is the reconstruction $\hat{k}_{(2P)}(T)$ after $P = 12$ shifts in each direction, whereas the dotted line represents the reconstruction $\hat{k}_{(0)}(T)$ obtained without any shifts; the vertical lines represent the boundaries of (dotted) the interval $\mathcal{I}_{(0)}$ and (solid) the union $\cup_{j=0}^{2P}\mathcal{I}_{(j)}$.

gion, and in this way reconstruct the constitutive relation over a much broader range of the state variable. Computational tests demonstrated the feasibility of the proposed approach on a simple 1D model problem, and constitute a proof of concept for the method.

Chapter 3

Extension of the Proposed Approach to a 2D Time–Dependent Multiphysics Problem

In this Chapter we extend the computational approach introduced earlier in Chapter 2 to the reconstruction of material properties in complex multiphysics phenomena based on incomplete and possibly noise measurements. By the "multiphysics" aspect we mean situations in which the material property used in one conservation equation is a function of a state variable governed by a different conservation equation, e.g., reconstruction of the temperature dependence of the viscosity coefficient used in the momentum equation, where the temperature is governed by a separate energy equation, which is the specific model problem investigated in this study. We preserve the way of solving such inverse problem as to formulate it as optimization problem focusing on the

"optimize–then–discretize" paradigm in which the optimality conditions are formulated at the continuous (PDE) level and only then discretized. The goal of the current investigation is to extend the approach formulated in Chapter 2 for a simple model to a multiphysics problem involving time–dependent fluid flow in a two–dimensional (2D) domain.

As a key contribution of this work we address a number of computational challenges related to accurate and efficient evaluation of cost functional gradients which are critical to the implementation of the approach. More specifically, these gradients are given in terms of integrals of expressions involving state and adjoint variables defined on a grid over contours given by the level sets of the temperature field. A number of techniques have been proposed for the numerical evaluation of integrals defined over manifolds defined by level–set functions. Some of them rely on regularized Dirac delta and Heaviside functions [44, 45], or discretization of the Dirac delta function [46–48]. Similar approaches based on approximations of the Dirac delta functions obtained using the level–set function and its gradient computed via finite differences were developed by Towers [49, 50]. A family of geometric approaches, proposed by Min and Gibou in [51, 52], relies on a decomposition of the entire domain into simplices. We emphasize that the problem discussed here is in fact more complicated, as the computation of cost functional gradients requires evaluation of the corresponding integrals for the level–set values spanning the entire state space of interest, hence there are additional issues related to the discretization of the state space which are outside the scope of references [44–52]. In order to address these questions and assess the different trade–offs we will compare the computational performance of three different methods for the evaluation of cost functional gradients.

3.1 Description of the Model

Let $\Omega \subset \mathbb{R}^d$, $d = 2, 3$, be the spatial domain on which our model problem is formulated. To fix attention, but without loss of generality, in the present investigation we focus on the problem of a reconstruction of the temperature dependence of the viscosity coefficient $\mu : \mathbb{R} \to \mathbb{R}^+$ in the momentum equation (Navier-Stokes equation) where the temperature T is governed by a separate energy equation (in 2D or 3D):

$$\partial_t \mathbf{u} + \mathbf{u} \cdot \boldsymbol{\nabla} \mathbf{u} + \boldsymbol{\nabla} p - \boldsymbol{\nabla} \cdot \left[\mu(T) [\boldsymbol{\nabla} \mathbf{u} + (\boldsymbol{\nabla} \mathbf{u})^T] \right] = 0 \qquad \text{in } \Omega, \tag{3.1a}$$

$$\boldsymbol{\nabla} \cdot \mathbf{u} = 0 \qquad \text{in } \Omega, \tag{3.1b}$$

$$\partial_t T + \mathbf{u} \cdot \boldsymbol{\nabla} T - \boldsymbol{\nabla} \cdot [k \boldsymbol{\nabla} T] = 0 \qquad \text{in } \Omega, \tag{3.1c}$$

subject to appropriate Dirichlet (or Neumann) boundary and initial conditions

$$\mathbf{u} = \mathbf{u}_b \qquad \text{on } \partial\Omega, \tag{3.2a}$$

$$T = T_b \qquad \text{on } \partial\Omega, \tag{3.2b}$$

$$\mathbf{u}(\cdot, 0) = \mathbf{u}_0, \ T(\cdot, 0) = T_0 \qquad \text{in } \Omega. \tag{3.2c}$$

The specific inverse problem we address in this investigation is formulated as follows. Given a set of time–dependent "measurements" $\{\tilde{T}_i(\tau, \mathbf{x})\}_{i=1}^M$ of the state variable (temperature) T at a number of points $\{\mathbf{x}_i\}_{i=1}^M$ in the domain Ω (or along the boundary $\partial\Omega$) and obtained within the time window $\tau \in [0, t_f]$, we seek to reconstruct the constitutive relation $\mu = \mu(T)$ such that solutions of problem (3.1) obtained with this reconstructed function will fit best the available measurements.

In regard to reconstruction of constitutive relations in general, it is important that such relations be consistent with the second principle of thermodynamics [28]. There exist two mathematical formalisms, one due to Coleman and Noll [29] and another one due to Liu [30], developed to ensure in a very general setting that a given form of the constitutive relation does not violate the second principle of thermodynamics. In continuous thermodynamical and mechanical systems this principle is expressed in terms of the Clausius–Duhem inequality [31] which in the case of our present model problem (3.1)–(3.2) reduces to the statement that $\mu(T) > 0$ for all values of T.

In our discussion below we will also need definitions of the following intervals, cf. Figure 3.1:

- $[T_\alpha, T_\beta] \triangleq [\min_{\mathbf{x}\in\overline{\Omega}} T(\mathbf{x}), \max_{\mathbf{x}\in\overline{\Omega}} T(\mathbf{x})]$ which represents the temperature range spanned by the solution of problem (3.1); thus, following [19], we will refer to the interval $\mathcal{I} \triangleq [T_\alpha, T_\beta]$ as the *identifiability interval*,

- $\mathcal{L} \triangleq [T_a, T_b]$, where $T_a \leq T_\alpha$ and $T_b \geq T_\beta$; this will be the temperature interval on which we will seek to obtain a reconstruction of the material property; we note that in general the interval $\mathcal{L}$ will be larger than the identifiability interval, i.e., $\mathcal{I} \subseteq \mathcal{L}$, and

- $\mathcal{M} \triangleq [\min_{1\leq i\leq M} \min_{0<t\leq t_f} \tilde{T}_i(t), \max_{1\leq i\leq M} \max_{0<t\leq t_f} \tilde{T}_i(t)]$ which defines the temperature range spanned by the measurements $\{\tilde{T}_i\}_{i=1}^M$; this interval is always contained the identifiability interval $\mathcal{I}$, i.e., $\mathcal{M} \subseteq \mathcal{I}$; we will refer to the interval $\mathcal{M}$ as the *measurement span*.

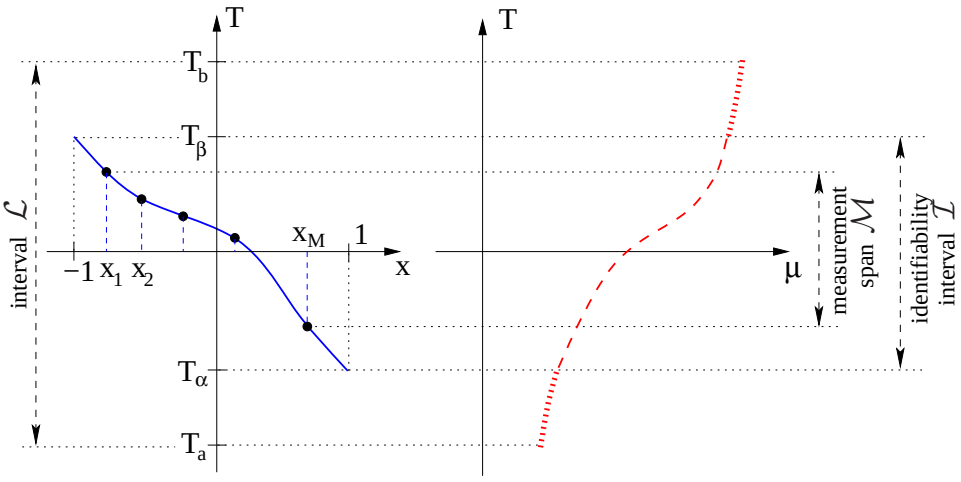

Figure 3.1: Schematic showing (left) the solution $T(t_0, x)$ at some fixed time t_0 and (right) the corresponding constitutive relation $\mu(T)$ defined over their respective domains, i.e., $\Omega = (-1, 1)$ and the identifiability region $\mathcal{I}$. The thick dotted line represents the extension of the constitutive relation $\mu(T)$ from $\mathcal{I}$ to the interval $\mathcal{L}$. In the Figure on the right the horizontal axis is to be interpreted as the ordinate.

3.2 Statement of Optimization Problem

3.2.1 Parameter Estimation as an Optimization Problem

It is assumed that the constitutive relations $\mu(T)$ are differentiable functions of the state variable (temperature) and belong to the following set

$$\mathcal{S}_\mu = \{\mu(T) \text{ piecewise } C^1 \text{ on } \mathcal{L};\ 0 < m_\mu \leq \mu(T) \leq M_\mu,\ \forall\, T \in \mathcal{L}\}, \qquad (3.3)$$

where $m_\mu, M_\mu \in \mathbb{R}^+$. We will also assume that the set $\mathcal{S}_\mu$ consisting of constitutive relations $\mu(T)$ defined on $\mathcal{L}$ is embedded in a Hilbert (function) space $\mathcal{X}$ to be specified below. Solving our parameter estimation problem is therefore

equivalent to finding a solution to the operator equation

$$\mathcal{F}(\mu) = T, \tag{3.4}$$

where $\mathcal{F} : \mathcal{S}_\mu \to L_2(\Omega)$ is the map from the constitutive relations to the measurements. An approach commonly used to solve such problems consists in reformulating them as least–squares minimization problems which in the present case can be done by defining the cost functional $\mathcal{J} : \mathcal{X} \to \mathbb{R}$ as

$$\mathcal{J}(\mu) \triangleq \frac{1}{2} \int_0^{t_f} \sum_{i=1}^{M} \left[T(\tau, \mathbf{x}_i; \mu) - \tilde{T}_i(\tau) \right]^2 d\tau, \tag{3.5}$$

where the dependence of the temperature field $T(\cdot; \mu)$ on the form of the constitutive relation $\mu = \mu(T)$ is given by governing system (3.1). We will assume that the functions $\mu = \mu(T)$ characterizing the constitutive relation are defined for $T \in \mathcal{L}$ and belong to a Hilbert (function) space $\mathcal{X}$. The optimal reconstruction $\hat{\mu}$ is obtained as an unconstrained minimizer of cost functional (3.5), i.e.,

$$\hat{\mu} = \underset{\mu \in \mathcal{X}}{\operatorname{argmin}} \, \mathcal{J}(\mu). \tag{3.6}$$

We recall that the constitutive property is required to satisfy the additional positivity condition $\mu(T) > 0$ for all $T \in \mathcal{L}$. Therefore, the optimal reconstruction $\hat{\mu}$ should in fact be obtained as an *inequality*–constrained minimizer of cost functional (3.5), i.e.,

$$\hat{\mu} = \underset{\substack{\mu \in \mathcal{X}, \\ \mu(T) > 0, \ T \in \mathcal{L}}}{\operatorname{argmin}} \, \mathcal{J}(\mu). \tag{3.7}$$

We add that in problems involving constitutive relations depending on several state variables the inequality constraint $\mu(T) > 0$ will be replaced with a more general form of the Clausius–Duhem inequality [31]. Different computational approaches for converting inequality–constrained optimization problems to unconstrained formulations are surveyed in [4,34]. Here we follow a straightforward approach based on the so-called "slack" variable [53]. We define a new function $\theta(T) : \mathbb{R} \to \mathbb{R}$ such that

$$\mu(T) = \theta^2(T) + m_\mu, \tag{3.8}$$

where m_μ is a lower bound for $\mu(T)$, cf. (3.3). This change of variables allows us to transform the *inequality*–constrained optimization problem (3.7) to a new unconstrained one

$$\hat{\theta} = \underset{\theta \in \mathcal{X}}{\operatorname{argmin}}\, \mathcal{J}(\theta) \tag{3.9}$$

where the constraint $\mu(T) > 0$ is satisfied automatically when minimization is performed with respect to the new variable $\theta(T)$. In a view of (3.3), we note that the new optimization variable θ belongs to the following set

$$\mathcal{S}_\theta = \{\theta(T) \text{ piecewise } C^1 \text{ on } \mathcal{L};\ |\theta(T)| < \sqrt{M_\mu - m_\mu},\ \forall\, T \in \mathcal{L}\}. \tag{3.10}$$

The governing PDE system (3.1) can thus be rewritten in the form

$$\partial_t \mathbf{u} + \mathbf{u}\cdot\boldsymbol{\nabla}\mathbf{u} + \boldsymbol{\nabla} p - \boldsymbol{\nabla}\cdot\left[(\theta^2(T)+m_\mu)[\boldsymbol{\nabla}\mathbf{u} + (\boldsymbol{\nabla}\mathbf{u})^T]\right] = 0 \qquad \text{in } \Omega, \tag{3.11a}$$

$$\boldsymbol{\nabla}\cdot\mathbf{u} = 0 \qquad \text{in } \Omega, \tag{3.11b}$$

$$\partial_t T + \mathbf{u}\cdot\boldsymbol{\nabla} T - \boldsymbol{\nabla}\cdot[k\boldsymbol{\nabla} T] = 0 \qquad \text{in } \Omega, \tag{3.11c}$$

subject to Dirichlet boundary and initial conditions (3.2). The new problem (3.9) requires redefining cost functional (3.5) in terms of the new variable

$$\mathcal{J}(\theta) \triangleq \frac{1}{2}\int_0^{t_f}\sum_{i=1}^{M}\left[T(\mathbf{x}_i;\theta) - \tilde{T}_i\right]^2 d\tau. \tag{3.12}$$

Problem (3.9) is characterized by the first–order optimality condition which requires the Gâteaux differential of cost functional (3.12), defined as $\mathcal{J}'(\theta;\theta') = \lim_{\epsilon\to 0}\epsilon^{-1}[\mathcal{J}(\theta+\epsilon\theta') - \mathcal{J}(\theta)]$, to vanish for all perturbations $\theta' \in \mathcal{X}$ [32], i.e.,

$$\forall_{\theta'\in\mathcal{X}} \quad \mathcal{J}'(\hat{\theta};\theta') = 0. \tag{3.13}$$

The (local) optimizer $\hat{\theta}$ can be computed with the following gradient descent algorithm as $\hat{\theta} = \lim_{n\to\infty}\theta^{(n)}$, where

$$\begin{cases} \theta^{(n+1)} = \theta^{(n)} - \tau^{(n)}\boldsymbol{\nabla}_\theta\mathcal{J}(\theta^{(n)}), & n = 1,\dots, \\ \theta^{(1)} \quad = \theta_0, \end{cases} \tag{3.14}$$

in which $\boldsymbol{\nabla}_\theta\mathcal{J}(\theta)$ represents the *gradient* of cost functional $\mathcal{J}(\theta)$ with respect to the control variable θ (we will adopt the convention that a subscript on

the operator $\boldsymbol{\nabla}$ will be used when differentiation is performed with respect to variables other than $\mathbf{x}$), $\tau^{(n)}$ is the length of the step along the descent direction at the n–th iteration, whereas $\theta_0 = \sqrt{\mu_0 - m_\mu}$ is the initial guess taken, for instance, corresponding to a constant μ_0, or some other approximate theoretical prediction. For the sake of clarity, formulation (3.14) represents the steepest–descent algorithm, however, in practice one typically uses more advanced minimization techniques, such as the conjugate gradient method, or one of the quasi–Newton techniques [33]. We note that, since minimization problem (3.9) is in general nonconvex, condition (3.13) characterizes only a *local*, rather than *global*, minimizer.

The key ingredient of minimization algorithm (3.14) is computation of the cost functional gradient $\boldsymbol{\nabla}_\theta \mathcal{J}(\theta)$. We emphasize that, since $\theta = \theta(T)$ is a continuous variable, the gradient $\boldsymbol{\nabla}_\theta \mathcal{J}(\theta)$ represents in fact an infinite–dimensional sensitivity of $\mathcal{J}(\theta)$ to perturbations of $\theta(T)$. This gradient can be determined based on suitably defined *adjoint variables* (Lagrange multipliers) obtained from the solution of the corresponding *adjoint system*. Since this derivation differs in a number of imported technical details from analogous derivations in "standard" PDE–constrained optimization problems, it will be reviewed in Section 3.2.2. The expression for the gradient is then validated for consistency in Section 4.3.

3.2.2 Cost Functional Gradients via Adjoint–based Analysis

Since the new variable $\theta(T)$ belongs to set $\mathcal{S}_\theta$, cf. (3.10), we will seek to reconstruct $\theta(T)$ as elements of the Sobolev space $H^1(\mathcal{L})$, so that the gradient $\boldsymbol{\nabla}_\theta \mathcal{J}$ will need to be obtained with respect to the corresponding inner product.

However, in order to make the derivation procedure easier to follow, we will first obtain an expression for the gradient in the space $L_2(\mathcal{L})$, and only then will obtain the Sobolev gradients which will be eventually used in the solution of optimization problem (3.9). In all these steps our transformations will be formal. We begin by computing the directional (Gâteaux) differential of cost functional (3.12) which yields

$$\mathcal{J}'(\theta;\theta') = \int_0^{t_f} \sum_{i=1}^{M} [T(\mathbf{x}_i;\theta) - \tilde{T}_i]\, T'(\mathbf{x}_i;\theta,\theta') d\tau, \tag{3.15}$$

where the perturbation variable $T'(\mathbf{x}_i;\theta,\theta')$ satisfies the perturbation system obtained from (3.11). Next, we invoke the Riesz representation theorem [35] for the directional differential $\mathcal{J}'(\theta;\cdot)$, which yields

$$\mathcal{J}'(\theta;\theta') = \left\langle \boldsymbol{\nabla}_\theta \mathcal{J}, \theta' \right\rangle_{\mathcal{X}}, \tag{3.16}$$

where $\langle\cdot,\cdot\rangle_{\mathcal{X}}$ represents an inner product in the Hilbert space $\mathcal{X}$ (we will first set $\mathcal{X} = L_2(\mathcal{L})$ and afterwards change that to $\mathcal{X} = H^1(\mathcal{L})$). We note that the expression on the right–hand side (RHS) in (3.15) is not consistent with Riesz representation (3.16), since, as will be shown below, the perturbation variable θ' is hidden in the system defining $T'(\theta,\theta')$. However, this expression can be transformed to Riesz form (3.16) with the help of a suitably–defined adjoint variable which is stated in the form of the following theorem. The main aspect in which this derivation differs from standard adjoint analysis [6] is that the inner product in Riesz identity (3.16) is defined using the state variable (temperature) as the integration variable, whereas the variational formulation is defined using integration with respect to the independent variables ($\mathbf{x}$ and t).

Theorem 3.1 *Let Ω be a sufficiently regular open bounded domain and $\theta' \in \mathcal{X} = H^1(\mathcal{L})$. We assume that the solutions $\mathbf{u}$ and T of (3.11) are sufficiently smooth. Then, the Riesz representation of directional differential (3.15) has the form*

$$\mathcal{J}'(\theta;\theta') = -2\int_{-\infty}^{\infty}\int_{\Omega}\delta(T(\mathbf{x})-s)\,\theta(s)\,\left[\int_0^{t_f}[\boldsymbol{\nabla}\mathbf{u}+(\boldsymbol{\nabla}\mathbf{u})^T]:\boldsymbol{\nabla}\mathbf{u}^*\,d\tau\right]\theta'(s)\,d\mathbf{x}\,ds, \tag{3.17}$$

where $\delta(\cdot)$ denotes Dirac delta function and the adjoint state $\{\mathbf{u}^*, T^*\}$ is defined as the solution of the system

$$-\partial_t\mathbf{u}^* - \mathbf{u}\cdot\boldsymbol{\nabla}\mathbf{u}^* - \boldsymbol{\nabla}\cdot\boldsymbol{\sigma}^* + \mathbf{u}^*\cdot(\boldsymbol{\nabla}\mathbf{u})^T + T^*\boldsymbol{\nabla}T = 0 \qquad \text{in } \Omega, \tag{3.18a}$$

$$\boldsymbol{\nabla}\cdot\mathbf{u}^* = 0 \qquad \text{in } \Omega, \tag{3.18b}$$

$$-\partial_t T^* - \mathbf{u}\cdot\boldsymbol{\nabla}T^* - \boldsymbol{\nabla}\cdot[k\boldsymbol{\nabla}T^*] + 2\theta(T)\frac{d\theta}{dT}(T)[\boldsymbol{\nabla}\mathbf{u}+(\boldsymbol{\nabla}\mathbf{u})^T]:\boldsymbol{\nabla}\mathbf{u}^* = \sum_{i=1}^{M}[T(\mathbf{x}_i;\theta)-\tilde{T}_i]\delta(\mathbf{x}-\mathbf{x}_i) \qquad \text{in } \Omega, \tag{3.18c}$$

where $\boldsymbol{\sigma}^* \triangleq -p^*\mathcal{I}+(\theta^2(T)+m_\mu)\left[\boldsymbol{\nabla}\mathbf{u}^*+(\boldsymbol{\nabla}\mathbf{u}^*)^T\right]$, with the following boundary and terminal conditions

$$\begin{aligned} \mathbf{u}^* &= 0 && \text{on } \partial\Omega,\\ T^* &= 0 && \text{on } \partial\Omega,\\ \mathbf{u}^*(\cdot;t_f) = 0,\ T^*(\cdot;t_f) &= 0 && \text{in } \Omega. \end{aligned} \tag{3.19}$$

Proof. We will denote the stress tensor $\boldsymbol{\sigma} \triangleq -p\mathcal{I}+(\theta^2(T)+m_\mu)\left[\boldsymbol{\nabla}\mathbf{u}+(\boldsymbol{\nabla}\mathbf{u})^T\right]$ and rewrite the governing system (3.11) as

$$\begin{aligned} \partial_t \mathbf{u} + \mathbf{u}\cdot\boldsymbol{\nabla}\mathbf{u} - \boldsymbol{\nabla}\cdot\boldsymbol{\sigma} &= 0 \qquad \text{in } \Omega, \\ \boldsymbol{\nabla}\cdot\mathbf{u} &= 0 \qquad \text{in } \Omega, \\ \partial_t T + \mathbf{u}\cdot\boldsymbol{\nabla}T - \boldsymbol{\nabla}\cdot[k\boldsymbol{\nabla}T] &= 0 \qquad \text{in } \Omega \end{aligned} \tag{3.20}$$

with the boundary and initial conditions as described previously in (3.2). Perturbing the state variables $\mathbf{u}$, p and T, which are functions of time and space, we get

$$\begin{aligned} \mathbf{u} &= \mathbf{u}_0 + \epsilon\mathbf{u}' + \mathcal{O}(\epsilon^2), \\ p &= p_0 + \epsilon p' + \mathcal{O}(\epsilon^2), \\ T &= T_0 + \epsilon T' + \mathcal{O}(\epsilon^2), \end{aligned} \tag{3.21}$$

so that the corresponding expansion of the constitutive relation $\theta(T)$ will have the following form

$$\theta(T) = \theta_0(T) + \epsilon\theta'(T) + \mathcal{O}(\epsilon^2) = \theta_0(T_0) + \epsilon\frac{d\theta}{dT}(T_0)\,T' + \epsilon\theta'(T_0) + \mathcal{O}(\epsilon^2), \tag{3.22}$$

where the subscript "0" is used to denote the unperturbed (reference) material property, whereas the prime denotes the corresponding perturbation. We also have

$$\theta^2(T) = \theta_0^2(T_0) + 2\epsilon\theta_0(T_0)\,\frac{d\theta}{dT}(T_0)\,T' + 2\epsilon\theta_0(T_0)\theta'(T_0) + \mathcal{O}(\epsilon^2). \tag{3.23}$$

Substituting (3.21) and (3.23) into (3.20), collecting terms corresponding to ϵ in different powers and denoting

$$\hat{\boldsymbol{\sigma}} \triangleq -p'\mathcal{I} + (\theta^2(T) + m_\mu)\left[\boldsymbol{\nabla}\mathbf{u}' + (\boldsymbol{\nabla}\mathbf{u}')^T\right]$$
$$\tilde{\boldsymbol{\sigma}} \triangleq \left(2\theta(T)\,\frac{d\theta}{dT}(T)\,T' + 2\theta(T)\,\theta'(T)\right)\left[\boldsymbol{\nabla}\mathbf{u} + (\boldsymbol{\nabla}\mathbf{u})^T\right],$$

we now obtain the perturbation (sensitivity) system corresponding to (3.11)

$$\partial_t \mathbf{u}' + \mathbf{u}' \cdot \boldsymbol{\nabla}\mathbf{u} + \mathbf{u} \cdot \boldsymbol{\nabla}\mathbf{u}' - \boldsymbol{\nabla} \cdot (\hat{\boldsymbol{\sigma}} + \tilde{\boldsymbol{\sigma}}) = 0 \qquad \text{in } \Omega, \tag{3.24a}$$
$$\boldsymbol{\nabla} \cdot \mathbf{u}' = 0 \qquad \text{in } \Omega, \tag{3.24b}$$
$$\partial_t T' + \mathbf{u}' \cdot \boldsymbol{\nabla} T + \mathbf{u} \cdot \boldsymbol{\nabla} T' - \boldsymbol{\nabla} \cdot [k \boldsymbol{\nabla} T'] = 0 \qquad \text{in } \Omega, \tag{3.24c}$$

with the following boundary and initial conditions

$$\mathbf{u}' = 0 \qquad \text{on } \partial\Omega, \tag{3.25a}$$
$$T' = 0 \qquad \text{on } \partial\Omega, \tag{3.25b}$$
$$\mathbf{u}'(\cdot, 0) = 0,\ T'(\cdot, 0) = 0 \qquad \text{in } \Omega. \tag{3.25c}$$

Then, integrating equation (3.24a) against $\mathbf{u}^*$, equation (3.24b) against p^*, and equation (3.24c) against T^* over the space domain Ω and time $[0, t_f]$, integrating by parts and factorizing $\mathbf{u}'$, T' and p', we arrive at the following

relation

$$\begin{aligned}
&\int_0^{t_f}\int_\Omega \left[-\partial_t \mathbf{u}^* + \mathbf{u}^*\cdot(\boldsymbol{\nabla}\mathbf{u})^T - \mathbf{u}\cdot\boldsymbol{\nabla}\mathbf{u}^* - \boldsymbol{\nabla}\cdot\boldsymbol{\sigma}^* + T^*\boldsymbol{\nabla}T\right]\cdot\mathbf{u}' d\mathbf{x}\, d\tau \\
&-\int_0^{t_f}\int_\Omega (\boldsymbol{\nabla}\cdot\mathbf{u}^*)p' d\mathbf{x}\, d\tau \\
&+\int_0^{t_f}\int_\Omega \Big[-\partial_t T^* - \mathbf{u}\cdot\boldsymbol{\nabla}T^* - \boldsymbol{\nabla}\cdot(k\boldsymbol{\nabla}T^*) \\
&+2\theta(T)\frac{d\theta}{dT}(T)[\boldsymbol{\nabla}\mathbf{u} + (\boldsymbol{\nabla}\mathbf{u})^T] : \boldsymbol{\nabla}\mathbf{u}^*\Big] T' d\mathbf{x}\, d\tau \\
&+\int_0^{t_f}\int_\Omega 2\theta(T)\theta'(T)[\boldsymbol{\nabla}\mathbf{u} + (\boldsymbol{\nabla}\mathbf{u})^T] : \boldsymbol{\nabla}\mathbf{u}^* d\mathbf{x}\, d\tau = 0.
\end{aligned} \tag{3.26}$$

We now require that the adjoint variables $\mathbf{u}^*$, p^* and T^* satisfy system (3.18)–(3.19). We also note that owing to the judicious choice of the RHS term in (3.18c), the last term in relation (3.26) is in fact equal to the directional differential $\mathcal{J}'(\theta;\theta')$, so that we have

$$\begin{aligned}
&\mathcal{J}'(\theta;\theta') = \\
&-2\int_0^{t_f}\int_\Omega \theta(T(\mathbf{x},\tau))\theta'(T(\mathbf{x},\tau))\,[\boldsymbol{\nabla}\mathbf{u}(\mathbf{x},\tau) + (\boldsymbol{\nabla}\mathbf{u}(\mathbf{x},\tau))^T] : \boldsymbol{\nabla}\mathbf{u}^*(\mathbf{x},\tau)\, d\mathbf{x}\, d\tau,
\end{aligned} \tag{3.27}$$

where, for emphasis, we indicated the integration variables as arguments of the state and adjoint variables. We note that this expression is still not in Riesz form (3.16), where integration must be performed with respect to the state variable (temperature T). Thus, we proceed to express for any given function $f(T)$ its pointwise evaluation at $T(\mathbf{x})$ through the following integral transform. We define a "change–of–variable" operator, denoted Π, such that for given functions $f : \mathbb{R}\to\mathbb{R}$ and $T : \Omega\to\mathbb{R}$, we have

$$f(T(\mathbf{x})) = \int_{-\infty}^{+\infty} \delta(T(\mathbf{x}) - s) f(s)\, ds \triangleq (\Pi f)(\mathbf{x}). \tag{3.28}$$

Using this transform to express $f(T(\mathbf{x})) = \theta(T(\mathbf{x},\tau))\theta'(T(\mathbf{x},\tau))$ in (3.27) and changing the order of integration (Fubini's Theorem) we obtain expression (3.17) which is the required Riesz representation (3.16) of directional differential (3.15). □

We remark that we were able to prove an analogous result using a simpler approach based on the Kirchhoff transform in Chapter 2, where both the constitutive relation and the state variable were governed by the same equation (i.e. the problem was not of the "multiphysics" type). We also add that even though the result proved in the Theorem 3.1 is a bit similar to the results obtained by means of Theorem 2.1 in Chapter 2, the method we used here for the proof is in fact quite different as the Kirchhoff transform is not possible in a view of the current multiphysics problem.

With the Riesz representation established in (3.17), we now proceed to identify expressions for the cost functional gradient $\boldsymbol{\nabla}_\theta \mathcal{J}$ according to (3.16) using different spaces $\mathcal{X}$. While this is not the gradient that we will use in actual computations, we analyze first the "simplest" case when $\mathcal{X} = L_2(\mathcal{L})$, i.e., the space of functions square integrable on $[T_a, T_b]$, as it already offers some interesting insights into the structure of the problem. The L_2 gradient of the cost functional hence takes the form

$$\boldsymbol{\nabla}_\theta^{L_2} \mathcal{J}(s) = -2 \int_0^{t_f} \int_\Omega \delta(T(\mathbf{x}) - s)\, \theta(s)\, [\boldsymbol{\nabla}\mathbf{u} + (\boldsymbol{\nabla}\mathbf{u})^T] : \boldsymbol{\nabla}\mathbf{u}^*\, d\mathbf{x}\, d\tau. \quad (3.29)$$

As was discussed at length in Section 2, the L_2 gradients are not suitable for the reconstruction of material properties in the present problem, because in addition to lacking necessary smoothness, they are not defined outside the identifiability region (other than perhaps through a trivial extension with zero). Given the regularity required of the constitutive relations, cf. (3.10), the cost func-

tional gradients should be elements of the Sobolev space $H^1(\mathcal{L})$ of functions with square–integrable derivatives on $\mathcal{L}$. Using (3.16), now with $\mathcal{X} = H^1(\mathcal{L})$, we obtain

$$\begin{aligned} \mathcal{J}'(\theta;\theta') &= \langle \boldsymbol{\nabla}_\theta^{L_2}\mathcal{J}, \theta' \rangle_{L_2(\mathcal{L})} = \langle \boldsymbol{\nabla}_\theta^{H^1}\mathcal{J}, \theta' \rangle_{H^1(\mathcal{L})} \\ &= \int_{T_a}^{T_b} \left[\boldsymbol{\nabla}_\theta^{H^1}\mathcal{J}\,\theta' + \ell^2 \frac{d(\boldsymbol{\nabla}_\theta^{H^1}\mathcal{J})}{ds}\frac{d\theta'}{ds} \right] ds \end{aligned} \tag{3.30}$$

in which $\ell \in \mathbb{R}$ is a parameter with the meaning of a length–scale [we note that the L_2 inner product is recovered by setting $\ell = 0$ in (3.30)]. Performing integration by parts with the assumption that the Sobolev gradient $\boldsymbol{\nabla}_\theta^{H^1}\mathcal{J}$ satisfies the homogeneous Neumann boundary conditions at $T = T_a, T_b$ and noting that relation (3.30) must be satisfied for any arbitrary θ', we conclude that the Sobolev gradient can be determined as a solution of the following inhomogeneous elliptic boundary–value problem where the state variable acts as the independent variable

$$\boldsymbol{\nabla}_\theta^{H^1}\mathcal{J} - \ell^2 \frac{d^2}{ds^2}\boldsymbol{\nabla}_\theta^{H^1}\mathcal{J} = \boldsymbol{\nabla}_\theta^{L_2}\mathcal{J} \qquad \text{on } (T_a, T_b), \tag{3.31a}$$

$$\frac{d}{ds}\boldsymbol{\nabla}_\theta^{H^1}\mathcal{J} = 0 \qquad \text{for } s = T_a, T_b. \tag{3.31b}$$

We recall that by changing the value of the length–scale parameter ℓ we can control the smoothness of the gradient $\boldsymbol{\nabla}_\theta^{H^1}\mathcal{J}(\theta)$, and therefore also the relative smoothness of the resulting reconstruction of $\theta(T)$, and hence also the regularity of $\mu(T)$. More specifically, as was discussed earlier at the end of Section 2.3, extracting cost functional gradients in the Sobolev spaces H^p, $p > 0$, is equivalent to applying a low–pass filter to the L_2 gradient with the quantity ℓ representing the "cut-off" length scale. There are also other ways of defining the Sobolev gradients in the present problem which result in gradients characterized by a different behavior outside the identifiability region. As we stated

earlier, these methods can be interpreted as a special case of *data extrapolation*, as no additional measurement data is provided to construct Sobolev gradients $\boldsymbol{\nabla}_k^{H^1}\mathcal{J}(k)$. These approaches were thoroughly investigated in Chapter 2, and since they typically lead to inferior results, they will not be considered here. We finally conclude that iterative reconstruction of the constitutive relation $\mu(T)$ involves the following computations

1. solution of direct problem (3.11) with boundary and initial conditions (3.2),
2. solution of adjoint problem (3.18)–(3.19),
3. evaluation of expression (3.29) for the cost functional gradient,
4. computation of the smoothed Sobolev gradients by solving (3.31).

While steps (1), (2) and (4) are fairly straightforward, step (3) is not and will be thoroughly investigated in Section 3.3.1. We finally conclude that iterative reconstruction of the constitutive relation $\mu(T)$ involves the computations described in detail in Algorithm 3.

As we discussed in detail in Chapter 2, while the Sobolev gradient $\boldsymbol{\nabla}_\theta^{H^1}\mathcal{J}$ may be defined on an arbitrary interval $\mathcal{L} \supset \mathcal{I}$, the actual sensitivity information is essentially available only on the identifiability interval $\mathcal{I}$ (see Figure 3.1). In other words, extension of the gradient outside $\mathcal{I}$ via (3.31) does not generate new sensitivity information. Since, as demonstrated by our computational results reported in Chapter 2, such techniques are not capable of accurately reconstructing the relation $\mu(T)$ on an interval larger than the identifiability region, here we mention a different possibility to "extend" the identifiability region, so that the relation $\mu(T)$ can be reconstructed on a larger interval. This can be done simply by choosing suitable time–dependent

Algorithm 3 Algorithm for reconstructing $\mu(T)$ on a single identifiability interval $\mathcal{I}$

- set $n = 0$
- setup μ_0 as the initial guess
- compute θ_0 using change of variable formula (3.8)

repeat

- set $n = n + 1$
- obtain the solution of direct problem (3.11) with boundary and initial conditions (3.2)
- obtain the solution of adjoint problem (3.18)–(3.19)
- compute the cost functional gradient $\boldsymbol{\nabla}_\theta^{L_2}\mathcal{J}(\theta^{(n)})$ following (3.29)
- compute the cost functional gradient $\boldsymbol{\nabla}_\theta^{H^1}\mathcal{J}(\theta^{(n)})$ following the preconditioning scheme (3.31)
- determine step length $\tau^{(n)}$ in (3.14) via line minimization
- update the reconstructed property $\theta^{(n)}$ following gradient descent algorithm (3.14)

until the termination condition on $\theta^{(n)}$ is satisfied

- compute the final reconstruction $\hat{\mu}(T)$ based on $\theta^{(n)}$ using (3.8)

boundary conditions for temperature T_b in (3.2b), so that one can have essentially any arbitrary identifiability region $\mathcal{I}$ and the measurement span $\mathcal{M}$. Computational results illustrating the performance of our approach with different identifiability regions will be presented in Section 4.4.1. We remark that extending the identifiability region in this way is not possible in time–independent problems where more computational iterative approaches have to be used, cf. Chapter 2.

3.2.3 Reconstruction in the Presence of Measurement Noise

In this Section we discuss the important issue of reconstruction in the presence of noise in the measurements. As can be expected based on the general properties of parameter estimation problems [5], and as will be confirmed in Section 4.4.2, incorporation of random noise into the measurements leads to an instability in the form of small–scale oscillations appearing in the reconstructed constitutive relations. In the optimization framework a standard approach to mitigate this problem is Tikhonov regularization [40] in which original cost functional (3.12) is replaced with a regularized expression of the form

$$\mathcal{J}_\lambda(\theta) \triangleq \mathcal{J}(\theta) + \frac{\lambda}{2}\big\|\theta - \bar{\theta}\big\|^2_{\mathcal{Y}(\mathcal{I})}, \tag{3.32}$$

where $\lambda \in \mathbb{R}^+$ is an adjustable regularization parameter, $\bar{\theta}(T)$ represents a constitutive relation which our reconstruction $\theta(T)$ should not differ too much from, whereas $\|\cdot\|_{\mathcal{Y}(\mathcal{I})}$ is the Hilbert space norm in which we measure the deviation $(\theta - \bar{\theta})$. Thus, the regularization term in (3.32), i.e., the second one on the RHS, involves some additional information which needs to be specified a priori, namely, the choice of the reference relation $\bar{\theta}(T)$ and the space $\mathcal{Y}(\mathcal{I})$. As regards the reference function $\bar{\theta}(T)$, one natural possibility is to consider a constant value corresponding to a constant material property, and this is the solution we will adopt below. We recall here that $\theta(T)$ is in fact a "slack" variable and is related to the actual constitutive relation via (3.8). As regards the choice of the space $\mathcal{Y}(\mathcal{I})$, we will follow the discussion in Chapter 2 and consider a regularization term involving derivatives, namely $\mathcal{Y}(\mathcal{I}) = \dot{H}^1(\mathcal{I})$, where $\dot{H}^1(\mathcal{I})$ denotes the Sobolev space equipped with

the semi–norm $\|z\|_{\dot{H}^1(\mathcal{I})} \triangleq \int_{T_\alpha}^{T_\beta} \left(\frac{\partial z}{\partial s}\right)^2 ds$, $\forall_{z\in H^1(\mathcal{I})}$; the regularization term in (3.32) then becomes

$$\frac{\lambda}{2}\left\|\theta-\bar{\theta}\right\|^2_{\dot{H}^1(\mathcal{I})} = \frac{\lambda}{2}\int_{T_\alpha}^{T_\beta}\left(\frac{d\theta}{ds}-\frac{d\bar{\theta}}{ds}\right)^2 ds \tag{3.33}$$

yielding the following L_2 gradient of the regularized cost functional

$$\begin{aligned}\boldsymbol{\nabla}^{L_2}_{\theta}\mathcal{J}_\lambda(s) = &-2\int_0^{t_f}\int_\Omega \delta(T(\mathbf{x})-s)\,\theta(s)\left[\boldsymbol{\nabla}\mathbf{u}+(\boldsymbol{\nabla}\mathbf{u})^T\right]:\boldsymbol{\nabla}\mathbf{u}^*\,d\mathbf{x}\,d\tau \\ &+\lambda\left\{\frac{d\theta}{ds}\left[\delta(s-T_\beta)-\delta(s-T_\alpha)\right]-\frac{d^2\theta}{ds^2}\right\}.\end{aligned} \tag{3.34}$$

We remark that in obtaining (3.34) integration by parts was applied to the directional derivative of the regularization term. Expression (3.34) can now be used to compute the Sobolev gradients as discussed in Section 3.2.2. We add that penalty term (3.33) is defined on the identifiability interval $\mathcal{I}$ which is contained in the interval $\mathcal{L}$ on which the Sobolev gradients are computed. Computational tests illustrating the performance of the Tikhonov regularization on a problem with noisy data will be presented in Section 4.4.2. In that Section we will also briefly analyze the effect of the regularization parameter λ. We add that the stability and convergence of Tikhonov regularization using the Sobolev norm H^1 in the regularization term and applied to an inverse problem with similar mathematical structure, but formulated for a simpler PDE than (3.1), was established rigorously in [19].

3.3 Computational Aspects

3.3.1 Numerical Approaches to Gradient Evaluation

Without loss of generality, hereafter we will focus our discussion on the 2D case. For some technical reasons we will also assume that

$$\forall_{t\in[0,t_f]}\ \text{meas}\,\{\mathbf{x}\in\Omega,\ |\boldsymbol{\nabla}T(t,\mathbf{x})|=0\}=0, \tag{3.35}$$

i.e., that temperature gradient may not vanish on subregions with finite area. (This assumption is naturally satisfied when the temperature evolution is governed by equation of the parabolic type (3.1c).

A key element of reconstruction algorithm (3.14) is evaluation of the cost functional gradients given, in the L_2 case, by expression (3.29). The difficulty consists in the fact that, for every value of s (i.e., the dependent variable), one has to compute a line integral defined on the level set

$$\Gamma_s \triangleq \{\mathbf{x}\in\Omega,\ T(\mathbf{x})=s\} \tag{3.36}$$

of the temperature field $T(\mathbf{x})$. The integrand expression in such integrals is given in terms of solutions of the direct and adjoint problems (3.1)–(3.2) and (3.18)–(3.19) which are approximated on a grid. As will be shown below, this problem is closely related to approximation of one–dimensional Dirac measures in $\mathbb{R}^d$, an issue which has received some attention in the literature [44–52]. We will compare different computational approaches to this problem, and in order to better assess their accuracy, we will first test them on the generic expression

$$f(s)=\int_\Omega \delta(\phi(s,\mathbf{x}))g(\mathbf{x})\,d\mathbf{x} \tag{3.37}$$

for which the actual formula for the cost functional gradient (3.29) is a special case (except for the time integration). In (3.37) the function $\phi(s, \mathbf{x}) : \mathbb{R} \times \Omega \rightarrow \mathbb{R}$ represents the field whose s-level sets define the contours of integration Γ_s, whereas the function $g(\mathbf{x}) : \Omega \rightarrow \mathbb{R}$ represents the actual integrand expression. We note that by setting $\phi(s, \mathbf{x}) = T(\mathbf{x}) - s$, $g(\mathbf{x}) = 2\theta(T(\mathbf{x}))[\boldsymbol{\nabla}\mathbf{u}(\mathbf{x}) + (\boldsymbol{\nabla}\mathbf{u}(\mathbf{x}))^T] : \boldsymbol{\nabla}\mathbf{u}^*(\mathbf{x})$ and adding time integration in (3.37), we recover the original expression (3.29) for the cost functional gradient. We emphasize, however, that the advantage of using (3.37) with some simple closed–form expressions for $\phi(s, \mathbf{x})$ and $g(\mathbf{x})$ as a testbed is that this will make our assessment of the accuracy of the proposed methods independent of the accuracy involved in the numerical solution of the governing and adjoint PDEs (needed to approximate $\mathbf{u}$, T and $\mathbf{u}^*$).

In anticipation of one of the proposed numerical approaches, it is useful to rewrite (3.37) explicitly as a line integral

$$f(s) = \int_{\Gamma_s} \frac{g(\mathbf{x})}{|\boldsymbol{\nabla}\phi|}\, d\sigma \tag{3.38}$$

which is valid provided $|\boldsymbol{\nabla}\phi| \neq 0$ for every $\mathbf{x} \in \Gamma_s$ (proof of the equivalence of expressions (3.37) and (3.38) is provided in Appendix C). Formula (3.38) makes it clear that for a fixed value of s expression (3.29) for the cost functional gradient can be interpreted as a sum of line integrals defined on the instantaneous s–level sets of the temperature field $T(t, \mathbf{x})$.

The problem of accurate numerical evaluation of the expressions given by either (3.37) or (3.38) has received much attention, especially since the invention of the level-set approach by Osher and Sethian [54]. Traditionally, the problem of integration over codimension–1 manifolds defined by a level–set function $\phi(\mathbf{x})$ is studied in terms of the numerical evaluation of either the left–

hand side or right–hand side expression in the following relation, analogous to (3.37)–(3.38),

$$\int_{\Gamma:\ \phi(\mathbf{x})=0} h(\mathbf{x}) d\sigma = \int_{\Omega} \delta(\phi(\mathbf{x})) |\boldsymbol{\nabla}\phi(\mathbf{x})| h(\mathbf{x})\, d\mathbf{x}, \tag{3.39}$$

where, by absorbing the factor $|\boldsymbol{\nabla}\phi(\mathbf{x})|^{-1}$ into the definition of the function $h\ :\ \Omega \to \mathbb{R}$, one bypasses the problem of the points $\mathbf{x} \in \Gamma_s$ where $|\boldsymbol{\nabla}\phi(\mathbf{x})| = 0$. These approaches fall into two main groups:

A reduction to a *line (contour) integral*, cf. (3.38), or the left–hand side of (3.39), and

B evaluation of an *area integral*, cf. (3.37), or the right–hand side of (3.39).

In the context of this classification, the methods of geometric integration developed by Min and Gibou [51, 52] fall into the first category. This approach is based on decomposing the domain Ω into simplices, which in the simplest 2D case can be achieved via a regular triangulation, and then approximating the level–sets given by $\phi(\mathbf{x}) = 0$ with piecewise splines inside each simplex. Expression (3.38) then breaks up into a number of definite integrals which can be evaluated using standard quadratures.

In practice, however, area integration techniques seem to have become more popular. One family of such techniques relies on regularization δ_ϵ of the Dirac delta function with a suitable choice of the regularization parameter ϵ which characterizes the size of the support. While in the simplest case in which the parameter ϵ is determined based on the mesh size the error is $\mathcal{O}(1)$ [45], recently developed approaches [44, 45] achieve higher accuracy by adjusting ϵ based on the local gradient $|\boldsymbol{\nabla}\phi|$ of the level–set function. Another family of area integration approaches is represented by the work of Mayo [47]

further developed by Smereka [46] where an approximation $\tilde{\delta}$ of the Dirac delta function is obtained by analyzing the truncation error resulting from the application of the discrete Laplacian to Green's function. This approach can also be regarded as yet another way to regularize delta function $\delta(\phi(\mathbf{x}))$ using a fixed compact support in the one–dimensional (1D) space of values $\phi(\mathbf{x})$. In the second group of approaches we also mention consistent approximations to delta function obtained by Towers in [49, 50] using the level–set function and its gradient computed via finite differences.

In our present reconstruction problem, we have to evaluate the gradient expression (3.29) for the whole range of $T \in \mathcal{L}$, hence the discretization of the interval $\mathcal{L}$ will also affect the overall accuracy of the reconstruction, in addition to the accuracy characterizing evaluation of the gradient for a particular value of T. This is an aspect of the present problem which is outside the scope of earlier investigations concerning evaluation of the contour integrals of grid–based data [44–52]. Thus, we need to understand how the interplay of the discretizations of the physical space Ω and the state space s affects the accuracy of the reconstruction the respective step sizes will denoted h and h_T. In principle, one could also consider the effect of discretizing the time interval $[0, t_f]$, however, the corresponding step size is linked to h via the CFL condition, hence this effect will not be separately analyzed here. There are also questions concerning the computational complexity of the different approaches. Therefore, we will consider the following three methods to evaluate expression (3.37), or equivalently (3.38), which are representative of the different approaches mentioned above

#1 line integration over approximate level sets which is a method from group A based on a simplified version of the geometric integration developed

by Min and Gibou in [51, 52],

#2 approximation of Dirac delta measures developed by Smereka in [46] which is an example of a regularization technique and utilizes the area integration strategy group B, and

#3 approximation of contour integrals with area integrals, a method which also belongs to group B and combines some properties of regularization and discretization of Dirac delta measures discussed above [44–46]; more details about this approach, including an analysis for its accuracy, are provided in Section 3.3.1.

To fix attention, we now introduce two different finite–element (FEM) discretizations of the domain Ω

- using triangular elements $\Omega_i^{\triangle}$, $i = 1, \ldots, N_{\triangle}$, such that

$$\Omega = \bigcup_{i=1}^{N_{\triangle}} \Omega_i^{\triangle}, \quad \text{and} \tag{3.40}$$

- quadrilateral elements $\Omega_i^{\square}$, $i = 1, \ldots, N_{\square}$, such that

$$\Omega = \bigcup_{i=1}^{N_{\square}} \Omega_i^{\square}, \tag{3.41}$$

where $N_{\triangle}$ and $N_{\square}$ are the total numbers of the elements for each type of discretization (in case of uniform triangulation one has $N_{\triangle} = 2N_{\square}$). In our computational tests we will assume that the functions $\phi(s, \mathbf{x})$ and $g(\mathbf{x})$ are given either analytically or in terms of the following FEM representations

$$\phi(s, \mathbf{x})|_{\Omega_i^{\triangle}} = \Sigma_{k=1}^{3} \phi_k^i \psi_k^i(\mathbf{x}), \quad g(\mathbf{x})|_{\Omega_i^{\triangle}} = \Sigma_{k=1}^{3} g_k^i \psi_k^i(\mathbf{x}), \quad i = 1, \ldots, N_{\triangle}, \tag{3.42}$$

$$\phi(s,\mathbf{x})|_{\Omega_i^\square} = \Sigma_{k=1}^4 \phi_k^i \psi_k^i(\mathbf{x}), \quad g(\mathbf{x})|_{\Omega_i^\square} = \Sigma_{k=1}^4 g_k^i \psi_k^i(\mathbf{x}), \quad i = 1,\dots,N_\square, \quad (3.43)$$

where ϕ_k^i and g_k^i are the given nodal values of the functions $\phi(s,\mathbf{x})$ and $g(\mathbf{x})$, whereas $\psi_k^i(\mathbf{x})$ are the basis functions (linear in (3.42) and bilinear in (3.43) [55]). We also discretize reconstruction interval (solution space) $\mathcal{L} = [T_a, T_b]$ with the step size h_T as follows

$$T_i = T_a + i\, h_T, \quad i = 0,\dots,N_T, \quad h_T = \frac{T_b - T_a}{N_T}. \quad (3.44)$$

Line Integration Over Approximate Level Sets

This approach is a variation of the geometric integration technique developed by Min and Gibou [51, 52]. The main idea behind both methods is decomposition of the domain Ω into simplices, which in our simplest 2D case is represented by triangulation (3.40), and then approximating the level-sets given by $\phi(s,\mathbf{x}) = 0$ with piecewise linear splines inside each simplex (triangle). While in the geometric integration approach of Min and Gibou uses linear interpolation to refine locally the simplices which contain the level sets $\phi(s,\mathbf{x}) = 0$ and then the second–order midpoint rule for approximating line integrals over the selected simplices, in the present method we employ these approximations of the level–sets to reduce line integral (3.38) to a 1D definite integral which is then evaluated using standard quadratures.

The starting point for this approach is formula (3.38). For a fixed value of s the corresponding level set can be described as

$$\Gamma_s = \bigcup_{j=1}^{M(s)} \Gamma_s^j, \quad (3.45)$$

where $\Gamma_s^j \subset \Omega_j^\triangle$ and $M(s)$ is the total number of the finite elements containing

segments of the level set Γ_s. We thus need to approximate $\int_{\Gamma_s^j} \dfrac{g(\mathbf{x})}{|\boldsymbol{\nabla}\phi(s,\mathbf{x})|}\, d\sigma$, i.e., the line integral over the part of the level–set curve contained in the j-th finite element $\Omega_j^{\triangle}$. In view of (3.42) the integrand expression $\varrho(s,\mathbf{x}) \triangleq \dfrac{g(\mathbf{x})}{|\boldsymbol{\nabla}\phi(s,\mathbf{x})|}$ can be approximated as

$$\tilde{\varrho}(s,\mathbf{x})|_{\Omega_i^{\triangle}} \cong \Sigma_{k=1}^{3} \varrho_k^i \psi_k^i(\mathbf{x}),$$

where ϱ_k^i are the known nodal values of the function $\varrho(s,\mathbf{x})$. An approximation $\tilde{\Gamma}_s^j$ of the part of the level–set Γ_s^j corresponding to the j-th finite element can be obtained in an explicit form $y = y(x)$, $x \in [x', x'']$, or a parameterized form $x = x(t)$, $y = y(t)$ with $t \in [t', t'']$, based on representation (3.42) of the level–set function $\phi(s,\mathbf{x})$. This leads to the following two possible reductions of the line integral to a definite integral

$$\int_{\tilde{\Gamma}_s^j} \tilde{\varrho}(s,\mathbf{x}) d\sigma = \int_{x'}^{x''} \tilde{\varrho}(x, y(x)) \sqrt{\left(\frac{dy}{dx}\right)^2 + 1}\, dx \tag{3.46a}$$

$$\int_{\tilde{\Gamma}_s^j} \tilde{\varrho}(s,\mathbf{x}) d\sigma = \int_{t'}^{t''} \tilde{\varrho}(x(t), y(t)) \sqrt{\left(\frac{dx}{dt}\right)^2 + \left(\frac{dy}{dt}\right)^2}\, dt \tag{3.46b}$$

which can be evaluated using standard quadratures for 1D definite integrals. We then have

$$f(s) \approx \Sigma_{j=1}^{M(s)} \int_{\tilde{\Gamma}_s^j} \tilde{\varrho}(s,\mathbf{x})\, d\sigma. \tag{3.47}$$

We note that the accuracy of this approach is mainly determined by the order of integration used to represent the level set $\tilde{\Gamma}_s^j$ and the integrand expression $\tilde{\varrho}(s,\mathbf{x})$ which tend to depend on the type of the finite element (simplex) used [55]. (The error of the quadrature employed to evaluate (3.46) does not have a dominating effect.) As was mentioned in [51], the use of triangulation (3.40)

together with linear interpolation of $\phi(s, \mathbf{x})$ and $\varrho(s, \mathbf{x})$ results in the second–order accuracy of this method.

Approximation of Dirac Delta Measures

This approach has formula (3.37) for its starting point and relies on a discrete approximation of the Dirac delta function obtained by Smereka in [46]. It is derived via truncation of the discrete Laplacian of the corresponding Green's function. Suppose the domain Ω is covered with a uniform Cartesian grid corresponding to (3.41), i.e., $x_i = x_0 + ih$, $y_j = y_0 + jh$, where i, j are integer indices, $x_0, y_0 \in \mathbb{R}$ and h is the step size. The first–order accurate approximation of the discrete Dirac delta function at the node (x_i, y_j) is

$$\tilde{\delta}(\phi_{i,j}) = \tilde{\delta}^{(+x)}_{i,j} + \tilde{\delta}^{(-x)}_{i,j} + \tilde{\delta}^{(+y)}_{i,j} + \tilde{\delta}^{(-y)}_{i,j}, \tag{3.48}$$

where

$$\tilde{\delta}^{(+x)}_{i,j} \triangleq \begin{cases} \dfrac{|\phi_{i+1,j} D^0_x \phi_{i,j}|}{h^2 |D^+_x \phi_{i,j}| |\boldsymbol{\nabla}^\epsilon_0 \phi_{i,j}|} & \text{if } \phi_{i,j}\phi_{i+1,j} \le 0, \\ 0, & \text{otherwise,} \end{cases}$$

$$\tilde{\delta}^{(-x)}_{i,j} \triangleq \begin{cases} \dfrac{|\phi_{i-1,j} D^0_x \phi_{i,j}|}{h^2 |D^-_x \phi_{i,j}| |\boldsymbol{\nabla}^\epsilon_0 \phi_{i,j}|} & \text{if } \phi_{i,j}\phi_{i-1,j} < 0, \\ 0, & \text{otherwise,} \end{cases}$$

$$\tilde{\delta}^{(+y)}_{i,j} \triangleq \begin{cases} \dfrac{|\phi_{i,j+1} D^0_y \phi_{i,j}|}{h^2 |D^+_y \phi_{i,j}| |\boldsymbol{\nabla}^\epsilon_0 \phi_{i,j}|} & \text{if } \phi_{i,j}\phi_{i,j+1} \le 0, \\ 0, & \text{otherwise,} \end{cases}$$

$$\tilde{\delta}^{(-y)}_{i,j} \triangleq \begin{cases} \dfrac{|\phi_{i,j-1} D^0_y \phi_{i,j}|}{h^2 |D^-_y \phi_{i,j}| |\boldsymbol{\nabla}^\epsilon_0 \phi_{i,j}|} & \text{if } \phi_{i,j}\phi_{i,j-1} < 0, \\ 0, & \text{otherwise,} \end{cases}$$

where for the discretized level set function $\phi_{i,j} \triangleq \phi(s, x_i, y_j)$ we have the following definitions

$$D_x^+\phi_{i,j} \triangleq \frac{\phi_{i+1,j} - \phi_{i,j}}{h}, \quad D_x^-\phi_{i,j} \triangleq \frac{\phi_{i,j} - \phi_{i-1,j}}{h}, \quad D_x^0\phi_{i,j} \triangleq \frac{\phi_{i+1,j} - \phi_{i-1,j}}{2h}$$

and

$$|\boldsymbol{\nabla}_0^\epsilon \phi_{i,j}| \triangleq \sqrt{(D_x^0\phi_{i,j})^2 + (D_y^0\phi_{i,j})^2 + \varepsilon},$$

in which $\varepsilon \ll 1$ is used for regularization. The expressions $D_y^+\phi_{i,j}$, $D_y^-\phi_{i,j}$, $D_y^0\phi_{i,j}$ are defined analogously. Using the definition of the discrete delta function from (3.48), the value $f(s)$ in (3.37) can be thus approximated in the following way

$$f(s) \approx h^2 \sum_{i,j} \tilde{\delta}_{i,j}\, g_{i,j}, \tag{3.49}$$

where $g_{i,j}$ are the nodal values of the function $g(\mathbf{x})$. We note that this method was validated in [46] exhibiting the theoretically predicted first order of accuracy only in cases in which the level sets Γ_s do not intersect the domain boundary $\partial\Omega$, a situation which may occur in the present reconstruction problem.

Approximation of Contour Integrals with Area Integrals

Our third method, in which the level–set integral (3.37) is approximated with an area integral defined over a region containing the level set Γ_s, cf. (3.36), is a new approach and will be presented in some detail here. It consists of the following three steps

1. for a fixed value of the state variable $s = T_i$ we define the interval

$[T_{i-\frac{1}{2}}, T_{i+\frac{1}{2}}] = [s - \frac{1}{2}h_T, s + \frac{1}{2}h_T] \subset \mathcal{L}$; then we have

$$f(s) \approx \frac{1}{h_T} \int_{s-\frac{1}{2}h_T}^{s+\frac{1}{2}h_T} f(\zeta)\, d\zeta. \tag{3.50}$$

2. now we define a subdomain $\Omega_{s,h_T} \subset \Omega$ which contains all the points of Ω that lie between the two level–set curves $\Gamma_{s-\frac{1}{2}h_T}$ and $\Gamma_{s+\frac{1}{2}h_T}$

$$\Omega_{s,h_T} \triangleq \left\{ \mathbf{x} \in \Omega,\, T(\mathbf{x}) \in \left[s - \frac{1}{2}h_T, s + \frac{1}{2}h_T \right] \right\}, \tag{3.51}$$

see Figure 3.2a; we then approximate Ω_{s,h_T} with the region

$$\tilde{\Omega}_{s,h_T} \triangleq \bigcup_{j=1}^{N_{s,h_T}} \Omega^{\square}_{s,h_T;j}, \quad T(\mathbf{x}_j^0) \in \left[s - \frac{1}{2}h_T, s + \frac{1}{2}h_T \right], \quad \mathbf{x}_j^0 \in \Omega^{\square}_{s,h_T;j}, \tag{3.52}$$

see Figure 3.2b, which consists of the quadrilateral finite elements $\Omega^{\square}_{s,h_T;j}$, $j = 1, \ldots, N_{s,h_T}$, with the center points $\mathbf{x}_j^0$ satisfying the condition $T(\mathbf{x}_j^0) \in [s - (1/2)h_T, s + (1/2)h_T]$,

3. in view of (3.50), expression (3.37) is approximated with an area integral over the region contained between the level–set curves $\Gamma_{s-\frac{1}{2}h_T}$ and $\Gamma_{s+\frac{1}{2}h_T}$, which is in turn approximated by the FEM region $\tilde{\Omega}_{s,h_T}$ given by (3.52); finally, the integral over this region is approximated using the standard 2D compound midpoint rule as

$$f(s) \approx \frac{1}{h_T} \int_{s-\frac{1}{2}h_T}^{s+\frac{1}{2}h_T} \int_{\Omega} \delta(s(\mathbf{x}) - \zeta) g(\mathbf{x})\, d\mathbf{x}\, d\zeta \approx \frac{h^2}{h_T} \sum_{j=1}^{N_{s,h_T}} g(\mathbf{x}_j^0). \tag{3.53}$$

As regards the accuracy of this approach, we have the following

Theorem 3.2 *Formula* (3.53) *is second order accurate with respect to the discretization of the space domain and first order accurate with respect to the discretization of the state domain, i.e.,*

$$f(s) = \int_{\Omega} \delta(T(\mathbf{x}) - s) g(\mathbf{x})\ d\mathbf{x} = \frac{h^2}{h_T} \sum_{j=1}^{N_{s,h_T}} g(\mathbf{x}_j^0) + \mathcal{O}(h^2) + \mathcal{O}(h_T). \tag{3.54}$$

Proof. We start by integrating both sides of (3.37) over the interval $[T_{i-\frac{1}{2}}; T_{i+\frac{1}{2}}] = [s - \frac{1}{2}h_T; s + \frac{1}{2}h_T]$ obtaining

$$\begin{aligned} \int_{s-\frac{1}{2}h_T}^{s+\frac{1}{2}h_T} f(\zeta)\ d\zeta &= \int_{\Omega} \left[\int_{s-\frac{1}{2}h_T}^{s+\frac{1}{2}h_T} \delta(T(\mathbf{x}) - \zeta)\ d\zeta \right] g(\mathbf{x})\ d\mathbf{x} \\ &= \int_{\Omega} \chi_{[s-\frac{1}{2}h_T, s+\frac{1}{2}h_T]}(T(\mathbf{x}))\ g(\mathbf{x})\ d\mathbf{x}, \end{aligned} \tag{3.55}$$

where the characteristic function

$$\chi_{[T',T'']}(T(\mathbf{x})) = \begin{cases} 1 & \text{for } T(\mathbf{x}) \in [T', T''], \\ 0 & \text{for } T(\mathbf{x}) \notin [T', T''], \end{cases}$$

describes the subdomain Ω_{s,h_T} introduced earlier in (3.51), cf. Figure 3.2a. Now, using a second–order accurate midpoint rule for 1D integration, we can express the LHS of (3.55) as

$$\int_{s-\frac{1}{2}h_T}^{s+\frac{1}{2}h_T} f(\zeta)\ d\zeta = f\left(\frac{T_{i-\frac{1}{2}} + T_{i+\frac{1}{2}}}{2} \right) \cdot h_T + \mathcal{O}(h_T^2) = f(s)h_T + \mathcal{O}(h_T^2). \tag{3.56}$$

Approximation of the RHS in (3.55) takes place in two steps. In the first step we approximate the actual integration domain Ω_{s,h_T} with the union of the

finite elements $\tilde{\Omega}_{s,h_T}$, cf. (3.52). In order to estimate the error

$$E_1 \triangleq \left| \int_{\Omega_{s,h_T}} g(\mathbf{x})\ d\mathbf{x} - \int_{\tilde{\Omega}_{s,h_T}} g(\mathbf{x})\ d\mathbf{x} \right|$$

of this step, we divide the set of cells $\tilde{\Omega}_{s,h_T}$ into two subsets, see Figure 3.2b,

$$\tilde{\Omega}_{s,h_T} = \tilde{\Omega}^*_{s,h_T} \cup \tilde{\Omega}'_{s,h_T},$$

where $\tilde{\Omega}^*_{s,h_T}$ consists of the cells with all 4 vertices $\{\mathbf{x}_k\}_{k=1}^4$ satisfying the condition $T(\mathbf{x}_k) \in [s - \frac{1}{2}h_T, s + \frac{1}{2}h_T]$. The subregion $\tilde{\Omega}'_{s,h_T}$, defined as the compliment of $\tilde{\Omega}^*_{s,h_T}$ in $\tilde{\Omega}_{s,h_T}$, represents the union of "truncated" cells, i.e., cells which have at least one node outside Ω_{s,h_T}. This region is in turn further subdivided into two subsets, i.e.,

$$\tilde{\Omega}'_{s,h_T} = \tilde{\Omega}'_{s,h_T;in} \cup \tilde{\Omega}'_{s,h_T;out},$$

where

$$\tilde{\Omega}'_{s,h_T;in} \triangleq \left\{ \mathbf{x} \in \tilde{\Omega}'_{s,h_T},\ T(\mathbf{x}) \in \left[s - \frac{1}{2}h_T, s + \frac{1}{2}h_T \right] \right\},$$

$$\tilde{\Omega}'_{s,h_T;out} \triangleq \left\{ \mathbf{x} \in \tilde{\Omega}'_{s,h_T},\ T(\mathbf{x}) \notin \left[s - \frac{1}{2}h_T, s + \frac{1}{2}h_T \right] \right\}.$$

We have to define one more set $\tilde{\Omega}''_{s,h_T}$ which consists of the cells with at least one vertex $\{\mathbf{x}_k\}_{k=1}^4$ satisfying the condition $T(\mathbf{x}_k) \in [s - \frac{1}{2}h_T, s + \frac{1}{2}h_T]$, but whose the center points $\mathbf{x}_j^0$ lie outside Ω_{s,h_T}. We also further subdivide this set into two subsets

$$\tilde{\Omega}''_{s,h_T} = \tilde{\Omega}''_{s,h_T;in} \cup \tilde{\Omega}''_{s,h_T;out},$$

where

$$\tilde{\Omega}''_{s,h_T;in} \triangleq \left\{ \mathbf{x} \in \tilde{\Omega}''_{s,h_T},\, T(\mathbf{x}) \in \left[s - \frac{1}{2}h_T, s + \frac{1}{2}h_T \right] \right\},$$

$$\tilde{\Omega}''_{s,h_T;out} \triangleq \left\{ \mathbf{x} \in \tilde{\Omega}''_{s,h_T},\, T(\mathbf{x}) \notin \left[s - \frac{1}{2}h_T, s + \frac{1}{2}h_T \right] \right\}.$$

We thus have

$$\int_{\Omega_{s,h_T}} g(\mathbf{x})\, d\mathbf{x} = \int_{\tilde{\Omega}^*_{s,h_T}} g(\mathbf{x})\, d\mathbf{x} + \int_{\tilde{\Omega}'_{s,h_T;in}} g(\mathbf{x})\, d\mathbf{x} + \int_{\tilde{\Omega}''_{s,h_T;in}} g(\mathbf{x})\, d\mathbf{x}, \quad (3.57)$$

$$\begin{aligned} \int_{\tilde{\Omega}_{s,h_T}} g(\mathbf{x})\, d\mathbf{x} &= \int_{\tilde{\Omega}^*_{s,h_T}} g(\mathbf{x})\, d\mathbf{x} + \int_{\tilde{\Omega}'_{s,h_T}} g(\mathbf{x})\, d\mathbf{x} \\ &= \int_{\tilde{\Omega}^*_{s,h_T}} g(\mathbf{x})\, d\mathbf{x} + \int_{\tilde{\Omega}'_{s,h_T;in}} g(\mathbf{x})\, d\mathbf{x} + \int_{\tilde{\Omega}'_{s,h_T;out}} g(\mathbf{x})\, d\mathbf{x}, \end{aligned} \quad (3.58)$$

so that the domain approximation error can be estimated as follows

$$\begin{aligned} E_1 &= \left| \int_{\tilde{\Omega}'_{s,h_T;out}} g(\mathbf{x})\, d\mathbf{x} - \int_{\tilde{\Omega}''_{s,h_T;in}} g(\mathbf{x})\, d\mathbf{x} \right| \\ &\le \left| \int_{\tilde{\Omega}'_{s,h_T;out}} g(\mathbf{x})\, d\mathbf{x} \right| + \left| \int_{\tilde{\Omega}''_{s,h_T;in}} g(\mathbf{x})\, d\mathbf{x} \right| \\ &\le \max_{\mathbf{x}\in\Omega} |g(\mathbf{x})| \ \left(\left| \tilde{\Omega}'_{s,h_T} \right| + \left| \tilde{\Omega}''_{s,h_T} \right| \right) = \mathcal{O}(h^2), \end{aligned} \quad (3.59)$$

where $|\Omega| \triangleq$ meas Ω. The second error in the approximation of the RHS of (3.55) is related to the accuracy of the quadrature applied to $\int_{\tilde{\Omega}_{s,h_T}} g(\mathbf{x})\, d\mathbf{x}$ and for the spatial 2D compound midpoint rule is $E_2 = \mathcal{O}(h^2)$, so that we obtain

$$\left| \int_{\Omega_{s,h_T}} g(\mathbf{x})\, d\mathbf{x} - \sum_{j=1}^{N_{s,h_T}} g(\mathbf{x}_j^0)\, h^2 \right| = \mathcal{O}(h^2). \quad (3.60)$$

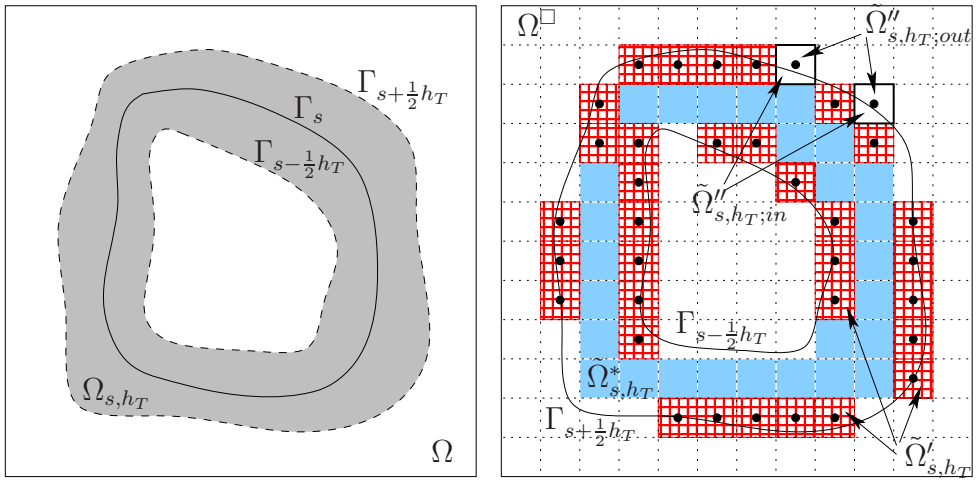

(a) (b)

Figure 3.2: Illustration of the third approach where the contour (line) integral (3.37) is approximated with an area integral (see Section 3.3.1): (a) region Ω_{s,h_T} which lies between the two level–set curves $\Gamma_{s-\frac{1}{2}h_T}$ and $\Gamma_{s+\frac{1}{2}h_T}$ and (b) its approximation with the region $\tilde{\Omega}_{s,h_T} = \tilde{\Omega}^*_{s,h_T} \cup \tilde{\Omega}'_{s,h_T}$; (checked) $\tilde{\Omega}'_{s,h_T}$ and (shaded) $\tilde{\Omega}^*_{s,h_T}$. Figure (b) also shows a part of region $\tilde{\Omega}''_{s,h_T} = \tilde{\Omega}''_{s,h_T;in} \cup \tilde{\Omega}''_{s,h_T;out}$ represented by 2 elements in the top right corner.

Comparing (3.53) with (3.56) and dividing both sides into h_T we finally obtain (3.54) which completes the proof. □

So far, we have considered the discretizations of the physical and state spaces, Ω and s, as independent. We remark that using the identity

$$\min_{\mathbf{x}\in\Omega} |\boldsymbol{\nabla} T(\mathbf{x})| \cdot h \leq h_T \leq \max_{\mathbf{x}\in\Omega} |\boldsymbol{\nabla} T(\mathbf{x})| \cdot h. \tag{3.61}$$

one could relate the corresponding discretization parameters h and h_T to each other.

Chapter 4

Computational Results

4.1 General Model Settings and Solver Validation

4.1.1 Models for Constitutive Relations

For validation purposes one needs an algebraic expression to represent the dependence of the viscosity coefficient on temperature which could serve as the "true" material property we will seek to reconstruct. The dynamic viscosity in liquids is usually approximated by exponential relations [56] and one of the most common expression for the coefficient of the dynamic viscosity is the law of Andrade (also referred to as the Nahme law) which is given in the dimensional form valid for T expressed in Kelvins in (4.1) below

$$\tilde{\mu}(T) = C_1 e^{C_2/T}, \tag{4.1}$$

where $C_1,\ C_2 > 0$ are constant parameters. As regards the thermal conductivity k, since it typically reveals a rather weak dependence on the temperature,

for the sake of simplicity we will treat it as a constant setting $k = 0.002$ in all computations presented in the present Chapter.

4.1.2 Solver, Flow Geometry and Model Parameters

We start by defining the following functional spaces $\mathcal{V} = [H^1(\Omega)]^2$, $\mathcal{V}_0 = [H^1_{\partial\Omega}(\Omega)]^2 = \{\mathbf{v} \in \mathcal{V},\ \mathbf{v} = \mathbf{0} \text{ on } \partial\Omega\}$, $\mathcal{Q} = L^2(\Omega)$, $\mathcal{W} = H^1(\Omega)$, $\mathcal{W}_0 = H^1_{\partial\Omega}(\Omega) = \{\vartheta \in \mathcal{W},\ \vartheta = 0 \text{ on } \partial\Omega\}$. We look for the solution of system (3.1)–(3.2) given by $\{\mathbf{u}(t), p(t), T(t)\} \in \mathcal{V}_b \times \mathcal{Q} \times \mathcal{W}_b$, where the functional spaces are defined as $\mathcal{V}_b = \{\mathbf{u} \in \mathcal{V},\ \mathbf{u} = \mathbf{u}_b \text{ on } \partial\Omega\}$ and $\mathcal{W}_b = \{T \in \mathcal{W},\ T = T_b \text{ on } \partial\Omega\}$, where $\mathbf{u}_b$ and T_b are the boundary conditions defined in (3.2). To solve the governing system numerically we first obtain a weak formulation for (3.1)–(3.2) which takes the following form

$$\int_\Omega (\partial_t \mathbf{u} + \mathbf{u}\cdot\boldsymbol{\nabla}\mathbf{u})\cdot\mathbf{v}\,d\mathbf{x} + 2\int_\Omega \mu(T)\mathbf{D}(\mathbf{u}) : \boldsymbol{\nabla}\mathbf{v}\,d\mathbf{x}$$

$$- \int_\Omega p(\boldsymbol{\nabla}\cdot\mathbf{v})\,d\mathbf{x} = 0 \qquad \text{in } \Omega, \qquad (4.2a)$$

$$\int_\Omega q(\boldsymbol{\nabla}\cdot\mathbf{u})\,d\mathbf{x} = 0 \qquad \text{in } \Omega, \qquad (4.2b)$$

$$\int_\Omega (\partial_t T + \mathbf{u}\cdot\boldsymbol{\nabla}T)\ \vartheta\,d\mathbf{x} + \int_\Omega k\boldsymbol{\nabla}T\cdot\boldsymbol{\nabla}\vartheta\,d\mathbf{x}\ = 0 \qquad \text{in } \Omega, \qquad (4.2c)$$

$\forall\{\mathbf{v}, q, \vartheta\} \in \mathcal{V}_0\times\mathcal{Q}\times\mathcal{W}_0$. We denote the strain rate tensor $\mathbf{D}(\mathbf{u}) \triangleq \frac{1}{2}\left[\boldsymbol{\nabla}\mathbf{u} + (\boldsymbol{\nabla}\mathbf{u})^T\right]$. We note that weak formulation (4.2) incorporates boundary conditions (3.2) via definition of the solution spaces $\mathcal{V}_b$ and $\mathcal{W}_b$. Next, we discretize system (4.2) in time using a semi-implicit approach which yields the following set of

equations defined at the time instant t_i

$$\int_\Omega \left(\frac{3\mathbf{u}_i - 4\mathbf{u}_{i-1} + \mathbf{u}_{i-2}}{2\Delta t} + \mathbf{u}_{i-1} \cdot \boldsymbol{\nabla} \mathbf{u}_i \right) \cdot \mathbf{v} \, d\mathbf{x}$$

$$+2 \int_\Omega \mu(T_{i-1}) \mathbf{D}(\mathbf{u}_i) : \boldsymbol{\nabla} \mathbf{v} \, d\mathbf{x} - \int_\Omega p_i (\boldsymbol{\nabla} \cdot \mathbf{v}) \, d\mathbf{x} = 0 \qquad \text{in } \Omega, \tag{4.3a}$$

$$\int_\Omega q (\boldsymbol{\nabla} \cdot \mathbf{u}_i) \, d\mathbf{x} = 0 \qquad \text{in } \Omega, \tag{4.3b}$$

$$\int_\Omega \left(\frac{3T_i - 4T_{i-1} + T_{i-2}}{2\Delta t} + \mathbf{u}_i \cdot \boldsymbol{\nabla} T_i \right) \vartheta \, d\mathbf{x}$$

$$+ \int_\Omega k \boldsymbol{\nabla} T_i \cdot \boldsymbol{\nabla} \vartheta \, d\mathbf{x} \; = 0 \qquad \text{in } \Omega, \tag{4.3c}$$

where the subscripts i, $i-1$ and $i-2$ denote, respectively, the quantities defined at the current time t_i and previous time instants t_{i-1} and t_{i-2}. Space discretization is carried out using triangular finite elements (3.40) and the P2 piecewise quadratic (continuous) representations for the velocity $\mathbf{u}$ and the temperature T fields, and the P1 piecewise linear (continuous) representation for the pressure p field. Applying such spatial discretization to system (4.3) we thus obtain a system of algebraic equations which at every time step is solved with `UMFPACK`, a direct solver for nonsymmetric sparse linear systems. We add that incompressibility is ensured by solving equation (4.3b) simultaneously with (4.3a). The choice of the time step Δt ensures stability by satisfying the following CFL condition

$$\left| \Delta t \left(\frac{u_{max}}{h_x} + \frac{v_{max}}{h_y} \right) \right| \leq 1. \tag{4.4}$$

The same numerical technique is used for discretizing and solving the adjoint problem (3.18)–(3.19).

To fix attention, all our computations are performed using a 2D square

domain $\Omega = [0,1]^2$, cf. Figure 4.1. Governing system (3.1)–(3.2) and adjoint system (3.18)–(3.19) are discretized on a uniform mesh with $N = N_x = N_y = 32$ grid points in every direction using triangular finite elements combined with the cubic spline interpolation of the function $\mu(T(\mathbf{x}))$. The rather modest spatial resolution used is a consequence of the fact that in a single reconstruction problem the governing and adjoint systems need to be solved $\mathcal{O}(10^3 - 10^4)$ times. Unless stated otherwise, the interval $\mathcal{L} = [100.0, 700.0]$ is discretized using an equispaced grid with $N_T = 600$ points. The actual constitutive relation $\tilde{\mu}(T)$ we seek to reconstruct is given by Andrade law (4.1) with $C_1 = 0.001$ and $C_2 = 10^3$.

In the computational tests reported below we used $M = 9$ measurement points distributed uniformly inside the cavity (Figure 4.1). To mimic an actual experimental procedure, relation (4.1) is used in combination with governing system (3.1) to obtain pointwise temperature measurements $\{\tilde{T}_i\}_{i=1}^M$. Relation (4.1) is then "forgotten" and is reconstructed using gradient–based algorithm (3.14). As in the simplified problem considered in Chapter 2, here as well we consider equispaced measurement locations $\{\mathbf{x}_i\}_{i=1}^M$ which coincide with the grid points of the discretized domain Ω. In general, more flexibility is possible in determining sensor locations, and these choices do not have any effect on the formulation of the algorithm. In terms of the initial guess in (3.14), unless stated otherwise, we take a constant approximation μ_0 to (4.1), given by $\mu_0 = \frac{1}{2}\left(\tilde{\mu}(T_\alpha) + \tilde{\mu}(T_\beta)\right) = \frac{C_1}{2}\left(e^{C_2/T_\alpha} + e^{C_2/T_\beta}\right)$ which translates into the following expression for the new optimization variable θ, cf. (3.8), $\theta_0 = \sqrt{\mu_0 - m_\mu}$, where $m_\mu = \frac{1}{2}\tilde{\mu}(T_\beta) = \frac{C_1}{2}e^{C_2/T_\beta}$. Since in the present problem the viscosity $\mu(T)$ is a function of the temperature, the Reynolds number is defined locally (both in space and in time) and varies in the range $Re = 0.05 \div 240$.

Unless stated otherwise, the boundary conditions for the temperature

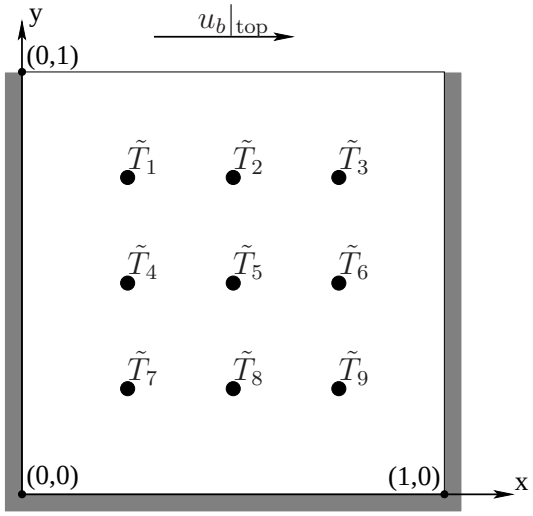

Figure 4.1: Geometry of the 2-D lid-driven (shear-driven) cavity.

are $T_b|_{\text{top}} = T_\beta = 500$ and $T_b|_{\text{else}} = T_\alpha = 300$ which result in the identifiability region $\mathcal{I} = [300.0, 500.0]$. The velocity boundary conditions $\mathbf{u}_b = [u_b, v_b]^T$ are given by $u_b|_{\text{top}} = U_0 \cos(\alpha t)$, $U_0 = 1$, $\alpha = 2\pi$ and $v_b|_{\text{top}} = 0$ on the top boundary segment and $\mathbf{u}_b|_{\text{else}} = \mathbf{0}$ on the remaining boundary segments. Their time–dependent character ensures that the obtained flow is unsteady at the values of the Reynolds number for which self–sustained oscillations do not spontaneously occur (the study of higher Reynolds numbers was restricted by the numerical resolution used, see comments above). We may also note that the CFL stability condition (4.4) still holds for time–dependent boundary conditions as the oscillation period $T_{\cos} = 1$ in the top boundary condition $u_b|_{\text{top}}$ is sufficiently large in comparison with the step size Δt in time discretization. The initial conditions $\{\mathbf{u}_0, T_0\}$ used in the reconstruction problem correspond to a developed flow obtained at $t = 10$ from the following initial and boundary conditions $T_b|_{\text{top}} = 500$, $T_b|_{\text{else}} = 300$ and $u_b|_{\text{top}} = 1$, $v_b|_{\text{top}} = 0$, $\mathbf{u}_b|_{\text{else}} = \mathbf{0}$, $T_0 = 300$, $\mathbf{u}_0 = \mathbf{0}$. We emphasize that adjoint system (3.18)–(3.19) is in fact a

terminal–value problem which needs to be integrated backwards in time, and its coefficients depend on the solution $\{\mathbf{u}, T\}$ of the direct problem around which linearization is performed at the given iteration. Our reconstructions are performed using the following time windows $[0, t_f]$, $t_f = \left\{\frac{1}{4}, \frac{1}{2}, 1\right\}$, which are all discretized with the time step $\Delta t = 5 \cdot 10^{-3}$ in both the direct and adjoint problems. The choice of the time step Δt ensures stability by satisfying the CFL condition (4.4).

In Figure 4.2 we present sample solutions of direct (3.1)–(3.2) and adjoint (3.18)–(3.19) problems for the lid–driven cavity flow with settings described in the current Section. The figures show the direct and adjoint vorticity fields $\omega \triangleq \boldsymbol{\nabla} \times \mathbf{u}$ and $\omega^* \triangleq \boldsymbol{\nabla} \times \mathbf{u}^*$, and the direct and adjoint temperature fields T and T^* at different time level inside the window $[0, 1]$. We add that the time–dependent temperature field $T(t, \mathbf{x})$ determines the level–sets on which the expression (3.29) for the cost functional gradients needs to be evaluated.

4.1.3 Validation of PDE solvers

Due to the simplicity of its geometry and boundary conditions, the lid–driven cavity flow problem has been used for a long time to validate novel solution approaches and codes [57, 58]. Numerical results are available for different aspect ratios and the problem was solved for both laminar and turbulent regimes using different numerical techniques. Thus, this problem is a useful testbed as there is a great deal of numerical data that can be used for comparison. Furthermore, it is relatively straightforward to implement the required solvers using available libraries. The code for solving direct problem (3.1)–(3.2) and adjoint problem (3.18)–(3.19) has been implemented using `FreeFem++` [59]. This is a high–level, open–source integrated development environment for the

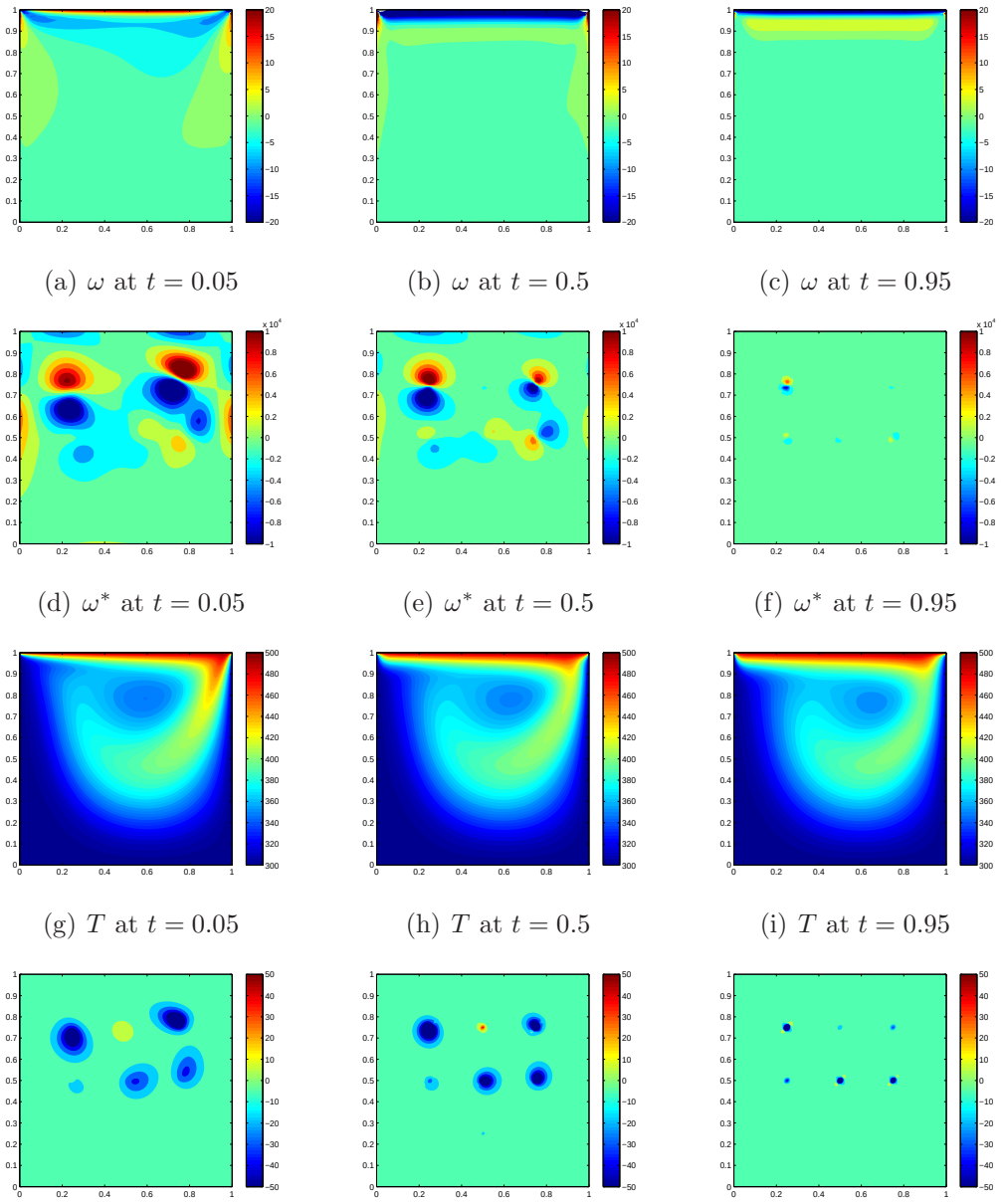

(a) ω at $t = 0.05$ (b) ω at $t = 0.5$ (c) ω at $t = 0.95$

(d) ω^* at $t = 0.05$ (e) ω^* at $t = 0.5$ (f) ω^* at $t = 0.95$

(g) T at $t = 0.05$ (h) T at $t = 0.5$ (i) T at $t = 0.95$

(j) T^* at $t = 0.05$ (k) T^* at $t = 0.5$ (l) T^* at $t = 0.95$

Figure 4.2: Direct and adjoint vorticity and temperature fields ω (a,b,c), ω^* (d,e,f), T (g,h,i), T^* (j,k,l) at the time levels $t = 0.05$ (a,d,g,j), $t = 0.5$ (b,e,h,k), $t = 0.95$ (c,f,i,l).

numerical solution of PDEs based on the Finite Element Method created by F. Hecht, O. Pironneau, J. Morice and A. Le Hyaric. The direct solver has been validated against available benchmark data from [57, 58, 60, 61] for the case when $\mu = const$, and all details are reported in the following Sections.

Solver for the Mass and Momentum Equations

For validation purposes the solution for the velocity field $\mathbf{u}$ obtained by solving (3.1) (or, more precisely, (3.11)), with boundary conditions (3.2) is compared with the benchmark data taken from Ghia et al. in [58]. Our tests consists in comparing the velocity field, namely the relative horizontal component of the velocity u/U_0, for the lid–driven cavity flow when it reaches the steady state for approximately low Reynolds numbers. As expected, using the flow geometry described in Section 4.1.2 and the time–independent boundary condition $u_b|_{\text{top}} = 1$ solutions of the initial–value problem tend to a steady–state solution for $Re = 100$ and different resolutions $N = 10, 20, 40, 80$. To qualify when the steady state is reached in the different cases, we use a criterion defined as

$$\left| \frac{d}{dt} \|\mathbf{u}\|_{L_2} \right| < \gamma, \tag{4.5}$$

where

$$\frac{d}{dt} \|\mathbf{u}\|_{L_2} \cong \frac{\|\mathbf{u}_{i+1}\|_{L_2} - \|\mathbf{u}_i\|_{L_2}}{\Delta t}$$

and $\mathbf{u}_i$ is a velocity field at discrete time t_i. The time t_s satisfying the condition (4.5) for different values of parameter γ is shown in Table 4.1. Comparison for the velocity field u/U_0 along the line $x = 0.5$ versus vertical coordinate y is shown in Figure 4.3. As is evident from the data shown in Figure 4.3, our results approach the benchmark data of Ghia et al. [58] as the resolution is

Table 4.1: Terminal time t_s satisfying the condition (4.5) for $\gamma = 0.01$ and $\gamma = 0.001$ for benchmark data test taken from [58].

$\gamma = 0.01$			$\gamma = 0.001$		
N	Δt	t_s	N	Δt	t_s
10	$5 \cdot 10^{-2}$	2.30	10	$5 \cdot 10^{-2}$	6.50
20	$1 \cdot 10^{-2}$	2.38	20	$1 \cdot 10^{-2}$	6.70
40	$5 \cdot 10^{-3}$	2.45	40	$5 \cdot 10^{-3}$	6.80
80	$1 \cdot 10^{-3}$	2.48	80	$1 \cdot 10^{-3}$	6.84

refined.

We also compare our results against the data, taken from Bruneau & Saad [57] as well as from the references [58, 60, 61], characterizing the vortex established in the cavity in the steady state at $Re = 1000$, i.e., the maximum of the stream–function ψ_{max}, vorticity ω and the location of the center x_v, y_v. The steady state is defined by the following condition

$$\frac{|\|\mathbf{u}_{i+1}\|_{L_2} - \|\mathbf{u}_i\|_{L_2}|}{\|\mathbf{u}_i\|_{L_2}} < \delta, \tag{4.6}$$

where $\delta = 10^{-12}$. The parameters characterizing the steady–state vortex in the cavity computed using our solver with different resolutions are shown in Table 4.2 where they are compared against available data from the literature. As the spatial resolution is refined a good quantitative agreement is noted with the benchmark results. The values of the time t_s satisfying condition (4.6) are not available for the results taken from [57, 58, 60, 61].

Finally, we compared the values for the global quantities obtained at the steady state in our computations, namely

- the kinetic energy $E = \frac{1}{2} \int_\Omega \|\mathbf{u}\|^2 dx$,

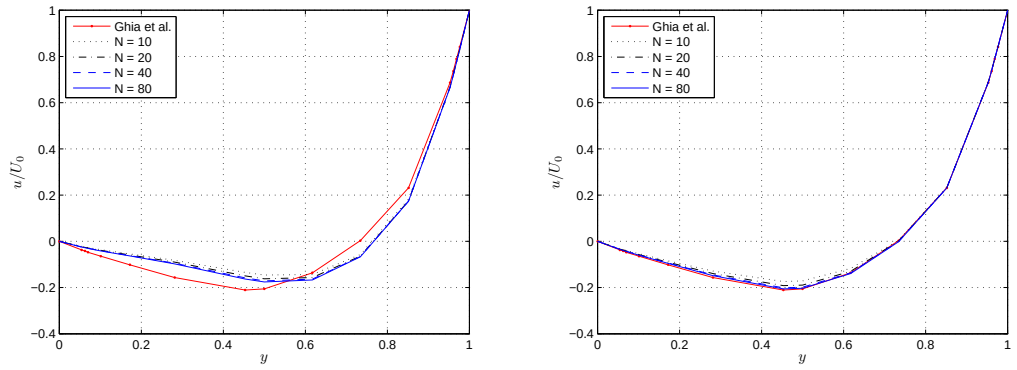

(a) (b)

Figure 4.3: The profile of the velocity field (relative horizontal component u/U_0) along the line $x = 0.5$ obtained with steady–state criterion (a) $\gamma = 0.01$ and (b) $\gamma = 0.001$ versus vertical coordinate y ($N \times N$ mesh, $N = 10, 20, 40, 80$) compared with available benchmark data in [58].

Table 4.2: Comparison of the parameters characterizing the steady–state vortex at $Re = 1000$ computed with our solver (described in Section 4.1.2) against benchmark results from the literature [57, 58, 60, 61].

Scheme	Grid	ψ_{max}	ω	x_v	y_v	t_s
Bruneau et al. [57]	128×128	0.11786	2.0508	0.46875	0.5625	N/A
Ghia et al. [58]	128×128	0.117929	2.04968	0.4687	0.5625	N/A
Schreiber et al. [60]	140×140	0.11603	2.026	0.47143	0.56429	N/A
Vanka et al. [61]	320×320	0.1173	–	0.4562	0.5625	N/A
Our solver (Section 4.1.2)	10×10	0.0900198	1.61278	0.46	0.5812	250.7
	20×20	0.0981879	1.72559	0.4624	0.5735	259.7
	40×40	0.107882	1.88543	0.4656	0.5688	253.125
	80×80	0.11327	1.97481	0.4674	0.5669	240.565
	128×128	0.115369	2.00935	0.4681	0.5663	230.632

Table 4.3: Comparison of the global quantities (total kinetic energy E, enstrophy Z, palinstrophy P) obtained with our solver against the benchmark data from [57].

Scheme	Grid	E	Z	P	t_s
Bruneau et al. [57]	64×64	0.021564	4.6458	0.56113×10^4	N/A
	128×128	0.022315	4.7711	0.70138×10^4	N/A
	256×256	0.022542	4.8123	0.78165×10^4	N/A
	512×512	0.022607	4.8243	0.82699×10^4	N/A
Our solver (Section 4.1.2)	10×10	0.0266381	4.47098	0.331354×10^4	276.35
	20×20	0.0235366	4.80921	0.621106×10^4	267.975
	40×40	0.0228494	4.85833	0.790261×10^4	258.475
	64×64	0.0227809	4.84722	0.843061×10^4	248.625
	128×128	0.0227678	4.83427	0.868976×10^4	242.24

- the enstrophy $Z = \frac{1}{2}\int_\Omega \|\omega\|^2 dx$,
- the palinstrophy $P = \frac{1}{2}\int_\Omega \|\nabla\omega\|^2 dx$

with the corresponding results reported at $Re = 1000$ by Bruneau & Saad in [57]. In contrast to previous test cases, the steady solution is obtained using a regularized velocity boundary conditions $u_b|_{\text{top}} = -16x^2(1-x)^2$. The steady state condition is the same as in the previous case and given in (4.6). The results shown in Table 4.3 demonstrate good quantitative agreement as the resolution is refined with the benchmark data from [57].

We conclude by saying that the results shown in Figure 4.3 and in Tables 4.2 and 4.3 clearly demonstrate the validity of our solution method for the mass and momentum equations.

Solver for the Coupled Mass, Momentum and Energy Equations

In the absence of any quantitative data concerning the temperature fields in the lid–driven cavity flows, we restrict our validation to a convergence study

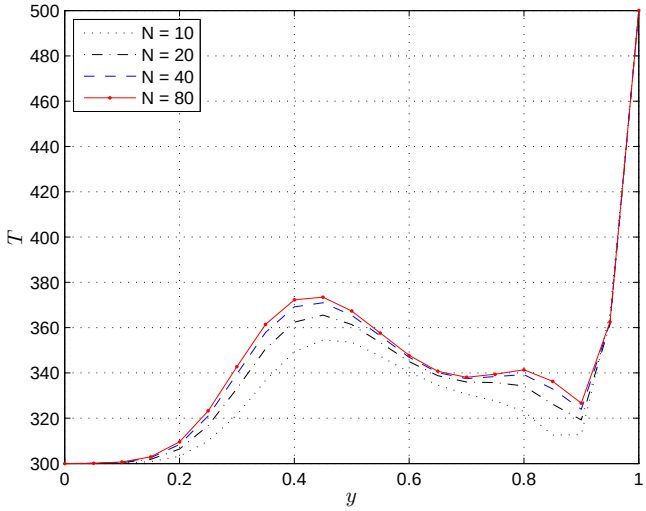

Figure 4.4: The profile of the temperature field T at the time $t_0 = 5$ along the line $x = 0.5$ versus the vertical coordinate y (for different resolutions $N \times N$ with $N = 10, 20, 40, 80$).

with respect to mesh refinement. We consider the case with $Re = 100$ and the velocity boundary conditions $u_b|_{\text{top}} = 1$, and in Figure 4.4 show the temperature profile along the line $x = 0.5$ obtained at some fixed time $t_0 = 5$ using different resolution. A clear uniform (in y) convergence to some limiting profile is observed as the resolution is refined. (We reiterate that in view of the CFL stability condition, cf. (4.4), refinement of the spatial discretization also implies the refinement of the time discretization).

4.2 Comparison of Different Approaches to Gradient Evaluation

In this Section we discuss the accuracy and efficiency of the three methods for evaluation of expression (3.37) presented in Sections 3.3.1, 3.3.1 and 3.3.1. In

order to assess their utility for the parameter reconstruction problem studied in this work, we will consider the following three test cases

(i) single (fixed) value of s with $\phi(s, \mathbf{x})$ and $g(\mathbf{x})$ given analytically,

(ii) parameter s varying over a finite range with $\phi(s, \mathbf{x})$ and $g(\mathbf{x})$ given analytically,

(iii) parameter s varying over a finite range with $\phi(s, \mathbf{x})$ and $g(\mathbf{x})$ given in terms of solutions of the direct and adjoint problem.

Tests (ii) and (iii) with s spanning the entire interval $\mathcal{L}$ are particularly relevant for the present reconstruction problem, as they help us assess the accuracy of the cost functional gradients over their entire domains of definition, including the values of s for which the level sets Γ_s intersect the domain boundary $\partial\Omega$. Results of tests (i)–(iii) are presented below.

Tests for a Single Value of s with $\phi(s, \mathbf{x})$ and $g(\mathbf{x})$ Given Analytically

Here we employ our three methods to compute numerically the value of a line integral over the circle $x^2 + y^2 = 1$

(a) in domain $\Omega_1 = [-2, 2]^2$ which contains the entire curve

$$I_{ex,1} = \int_{x^2+y^2=1} (3x^2 - y^2)\, d\sigma = 2\pi \tag{4.7}$$

(this test problem is actually borrowed from [46]),

(b) and in domain $\Omega_2 = [0, 2]^2$ which contains only a part of the curve in the first quadrant

$$I_{ex,2} = \int_{x^2+y^2=1,\, x,y>0} (3x^2 - y^2)\, d\sigma = \frac{\pi}{2}. \tag{4.8}$$

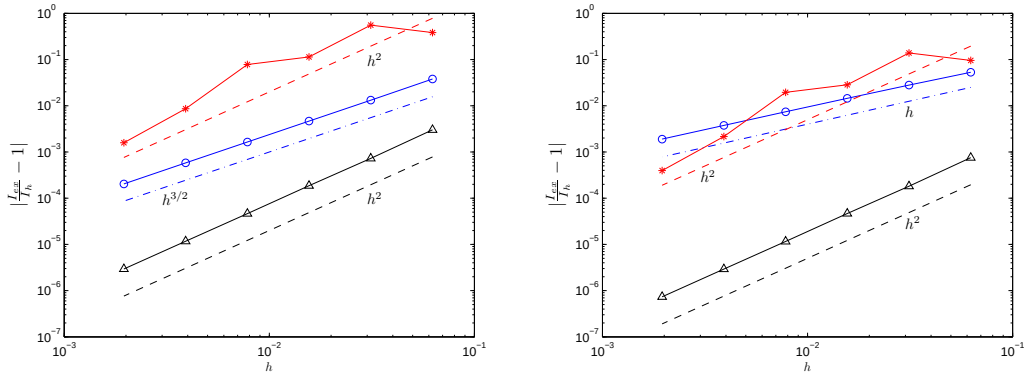

(a) (b)

Figure 4.5: Relative error $|\frac{I_{ex,i}}{I_h} - 1|$, $i = 1, 2$, versus discretization step $h = \Delta x = \Delta y$ in the numerical approximation I_h of (a) line integral (4.7) and (b) line integral (4.8) (See Section 4.2). Triangles represent the line integration approach (method #1), circles represent the results obtained using the delta function approximation (method #2), whereas asterisks show the data for the area integration approach (method #3).

The main difference between test cases (a) and (b) is that while in (a) the contour is entirely contained in the domain Ω_1, it intersects the domain boundary $\partial\Omega_2$ in case (b). As shown in Figure 4.5, methods #1 (line integration) and #3 (area integration) in both cases show the expected accuracy of $\mathcal{O}(h^2)$, where $h = \Delta x = \Delta y = 2^{-(3+i)}$, $i = 1 \ldots 6$, while method #2 (delta function approximation) is $\mathcal{O}(h^{3/2})$ accurate in case (a) and only $\mathcal{O}(h^1)$ accurate in case (b). We also add that the line integration method exhibits the smallest constant prefactor characterizing the error.

Tests for s Varying Over a Finite Range with $\phi(s,\mathbf{x})$ and $g(\mathbf{x})$ Given Analytically

In order to analyze this case we will introduce a new diagnostic quantity. We begin with the integral transform formula (3.28) applied to some perturbation $\mu'(T(\mathbf{x}))$

$$\mu'(T(\mathbf{x})) = \int_{-\infty}^{+\infty} \delta(\phi(s,\mathbf{x}))\mu'(s)\,ds, \tag{4.9}$$

where $\phi(s,\mathbf{x}) = T(\mathbf{x}) - s$. Multiplying both sides of (4.9) by $g(\mathbf{x})$, integrating over the domain Ω and changing the order of integration we obtain the following useful identity

$$\int_{\Omega} \mu'(T(\mathbf{x}))g(\mathbf{x})\,d\mathbf{x} = \int_{-\infty}^{+\infty} f(s)\mu'(s)\,ds \tag{4.10}$$

with $f(s)$ defined in (3.37), where the RHS has the structure of the Riesz identity for the Gâteaux differential of the cost functional, cf. (3.30), whereas the LHS is a simple area integral which can be easily evaluated using high–accuracy quadratures. Given the formal similarity of the RHS of (4.10) and the Riesz formula (3.30), this test is quite relevant for the optimization problem we are interested in here. We will thus use our three methods to evaluate the RHS of (4.10) and compared it to the LHS, which is evaluated with high precision on a refined grid in Ω, so that it can be considered "exact". Our tests are based on the following data

- spatial domain $\Omega = [0,1]^2$ discretized with $h = \Delta x = \Delta y = 2^{-(4+i)}$, $i = 1\ldots 7$,
- $h_T = \dfrac{T_b - T_a}{N_T}$, where $T_a = 100$, $T_b = 700$, whereas $N_T = 200; 1000; 10000$ (for methods #2 and #3) and $N_T = 200; 2000; 20000$ (for method #1),

- $T(\mathbf{x}) = 100(x^2 + y^2) + 300, \quad g(\mathbf{x}) = \cos(x) + 3\sin(2y - 1),$
- perturbations used $\mu_1'(s) = exp(-\frac{s}{1000})$, $\mu_2'(s) = \frac{10}{s^2}$ and $\mu_3'(s) = -\frac{s^2}{90000} + \frac{2s}{225} + \frac{2}{9}$, $s \in [T_a, T_b]$.

As is evident from Figure 4.6, all three methods show similar qualitative behavior, namely, the error decreases with decreasing h until it saturates which is due to the error terms depending on h_T becoming dominant. The saturation value of the error depends on the state space resolution h_T and is different for the different methods. Method #3 (area integration) reveals accuracy $\mathcal{O}(h^2)$, whereas method #2 (delta function approximation) is again only of accuracy about $\mathcal{O}(h)$ for the same discretization of the interval $\mathcal{L}$. Method #1 (line integration) performs better and shows accuracy up to $\mathcal{O}(h^5)$, but requires much finer resolution in the state space, namely $N_T > 20,000$ is needed ($h_T < 0.03$) for this behavior to be visible. On the other hand, method #3 (area integration) leads to the smallest errors for all the cases tested.

Analogous data is plotted in Figure 4.7 now as a function of the state space resolution h_T with h acting as a parameter. Similar trends are observed as in Figure 4.6, namely, the errors decrease with h_T until they eventually saturate when the error terms depending on h become dominant. Methods #1 and #2 reveal accuracy $\mathcal{O}(h_T)$, whereas method #3 has accuracy $\mathcal{O}(h_T^{1.5 \div 2})$ which is actually better than stipulated by Theorem 3.2, cf. (3.54). Method #3 is also characterized by the smallest value of the constant prefactor leading to the smallest overall errors.

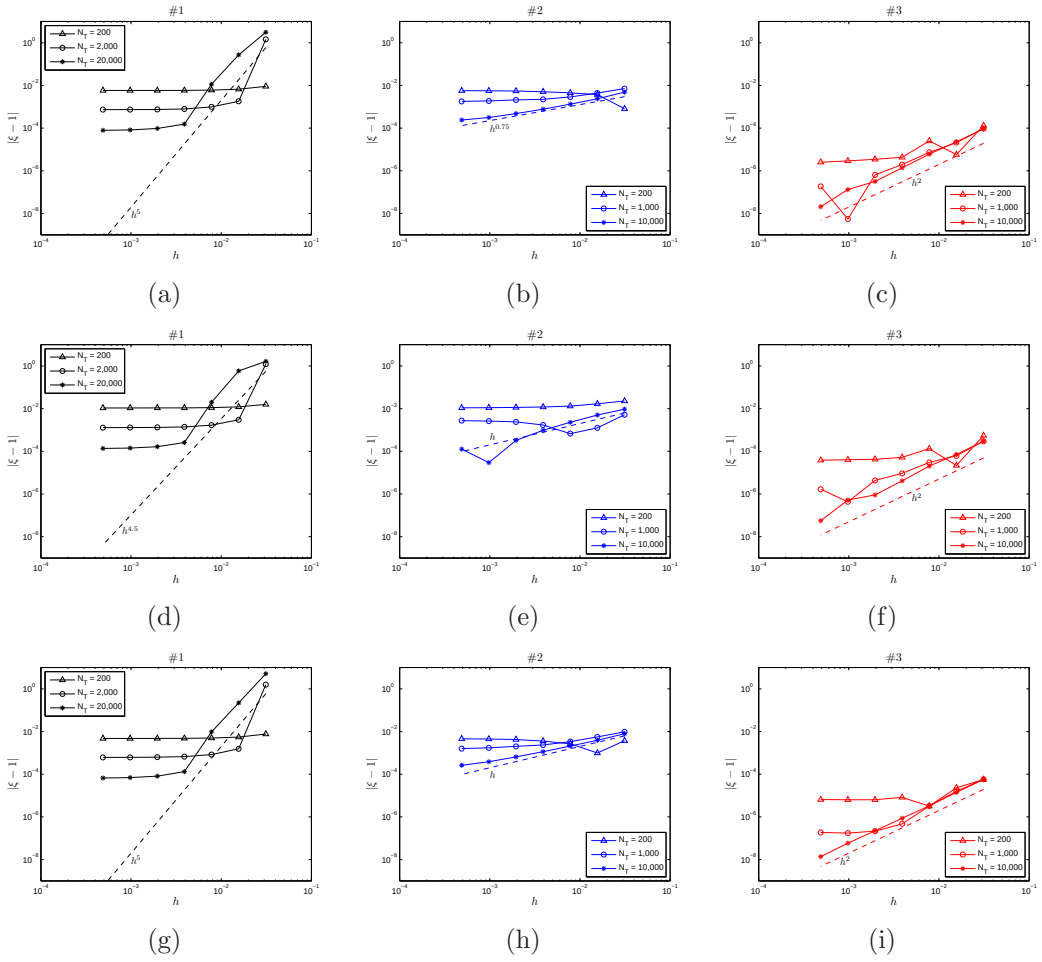

Figure 4.6: Relative error $|\xi - 1|$, where $\xi = \frac{\text{LHS of (4.10)}}{\text{RHS of (4.10)}}$, versus discretization step $h = \Delta x = \Delta y$ in approximating the RHS in (4.10). The first, second and third rows of figures show the results for μ_1', μ_2' and μ_3', respectively, while the figures in the first, second and third columns represent line integration (#1), delta function approximation (#2) and area integration (#3) methods, respectively.

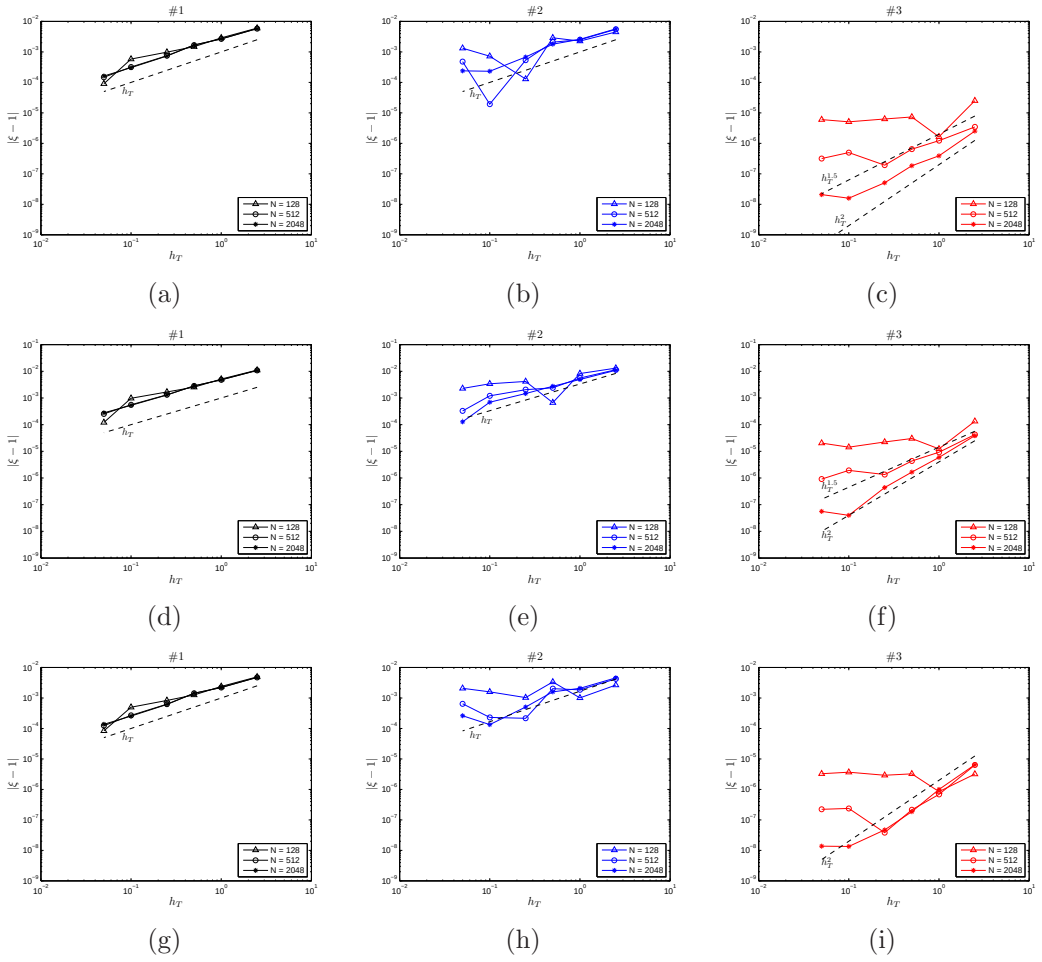

Figure 4.7: Relative error $|\xi - 1|$, where $\xi = \frac{\text{LHS of (4.10)}}{\text{RHS of (4.10)}}$, versus discretization step h_T in the state space $\mathcal{L}$ in approximating the RHS in (4.10). The first, second and third rows of figures show the results for μ_1', μ_2' and μ_3', respectively, while the figures in the first, second and third columns represent line integration (#1), delta function approximation (#2) and area integration (#3) methods, respectively.

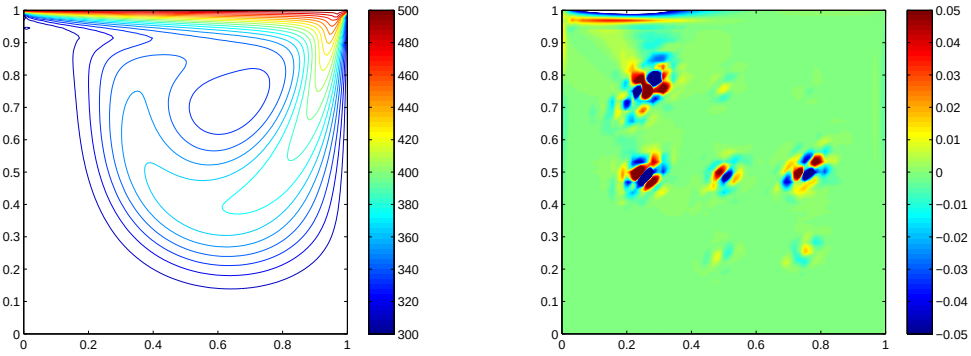

(a) (b)

Figure 4.8: The fields (a) $T(\mathbf{x})$ (level set contours) and (b) $g(\mathbf{x}) = [\boldsymbol{\nabla}\mathbf{u}(\mathbf{x}) + (\boldsymbol{\nabla}\mathbf{u}(\mathbf{x}))^T] : \boldsymbol{\nabla}\mathbf{u}^*(\mathbf{x})$ obtained by solving (3.1)–(3.2) and (3.18)–(3.19).

Tests for s Varying Over a Finite Range with $\phi(s, \mathbf{x})$ and $g(\mathbf{x})$ Given by Solutions of Direct and Adjoint Problem

We now repeat the test described in Section 4.2 using $\phi(s, \mathbf{x}) = T(\mathbf{x}) - s$ and $g(\mathbf{x}) = [\boldsymbol{\nabla}\mathbf{u}(\mathbf{x}) + (\boldsymbol{\nabla}\mathbf{u}(\mathbf{x}))^T] : \boldsymbol{\nabla}\mathbf{u}^*(\mathbf{x})$, where the fields $\mathbf{u}$, T and $\mathbf{u}^*$ come from solutions of the direct and adjoint problem (3.1)–(3.2) and (3.18)–(3.19) at some fixed time t, see Figure 4.8 (details of these computations will be given in Section 4.4.1). As before, we discretize the domain $\Omega = [0, 1]^2$ with the step $h = \Delta x = \Delta y = 2^{-(4+i)}$, $i = 1 \dots 7$, and the state space $\mathcal{L} = [T_a, T_b]$, $T_a = 100$ and $T_b = 700$, with the step $h_T = 0.06$ ($N_T = 10,000$).

The data shown in Figure 4.9 confirms our findings from Sections 4.2 and 4.2, namely, that in this case as well the error of all three methods decreases with h until it eventually saturates when the errors depending on h_T become dominant. Method #3 is again characterized by the smallest prefactor and hence leads to much smaller overall errors than in methods #1 and #2. The computational complexity of our three approaches is addressed in Figure 4.10,

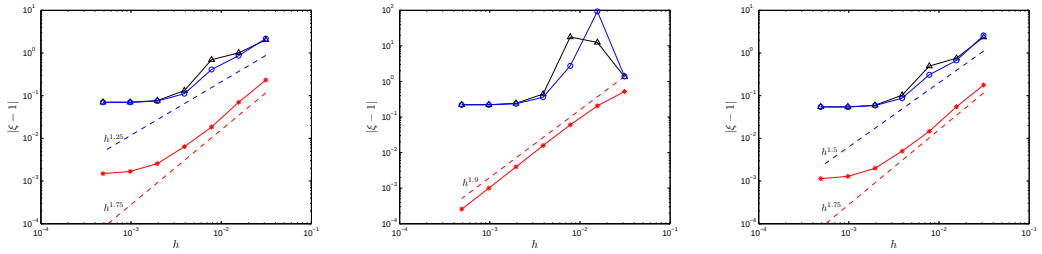

(a) (b) (c)

Figure 4.9: Relative error $|\xi - 1|$, where $\xi = \frac{\text{LHS of (4.10)}}{\text{RHS of (4.10)}}$, versus discretization step $h = \Delta x = \Delta y$ in estimating the RHS in (4.10), where $\phi(s, \mathbf{x}) = T(\mathbf{x}) - s$, and $g(\mathbf{x}) = [\boldsymbol{\nabla}\mathbf{u} + (\boldsymbol{\nabla}\mathbf{u})^T] : \boldsymbol{\nabla}\mathbf{u}^*$ obtained by solving (3.1)–(3.2) and (3.18)–(3.19). Figures (a), (b) and (c) show the results for μ_1', μ_2' and μ_3', respectively, using the same discretization of the state space $\mathcal{L}$ with $N_T = 10000$. Triangles represent the line integration approach (#1), circles show the results for the method of the delta function approximation (#2), while asterisks show the data from the area integration approach (#3).

where N_e is defined as a number of computational elements, e.g. $N_e = N_\triangle$ or $N_e = N_\square$ using (3.40) or (3.41), respectively. We see that, while the complexity of methods #1 and #2 scales as $\mathcal{O}(\sqrt{N_e})$, method #3 exhibits the scaling of $\mathcal{O}(N_e)$. On the other hand, however, method #3 has the smallest prefactor and, at least in the range of resolutions considered here, results in the shortest execution time.

In conclusion, these observations make the area integration approach (method #3) the method of choice for the present parameter reconstruction problem, and this is the approach we will use in all subsequent computations.

4.3 Validation of Gradients

In this Section we present results demonstrating the consistency of the cost functional gradients obtained with the approach described in Section 3.2.2.

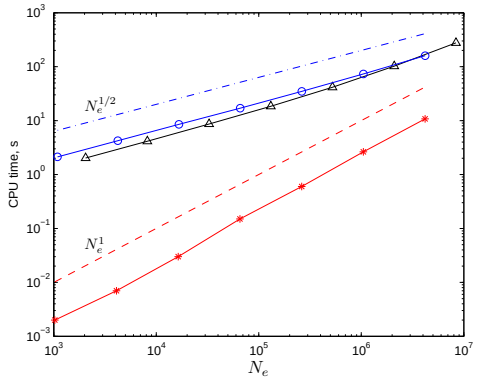

Figure 4.10: CPU time (in seconds) versus the number N_e of computational elements used in the different approaches, namely, (triangles) finite elements $\Omega_i^{\triangle}$ in the line integration approach (method #1), (circles) nodes in the method of the delta function approximation (#2) and (asterisks) finite elements $\Omega_i^{\square}$ in the area integration approach (#3). The data shown corresponds to the estimation of the RHS in (4.10) for μ_1' using the same discretization of the state space with $N_T = 10000$, $\phi(s, \mathbf{x}) = T(\mathbf{x}) - s$ and $g(\mathbf{x}) = [\boldsymbol{\nabla}\mathbf{u} + (\boldsymbol{\nabla}\mathbf{u})^T] : \boldsymbol{\nabla}\mathbf{u}^*$ obtained by solving (3.1)–(3.2) and (3.18)–(3.19).

In Figure 4.11 we present the L_2 and several Sobolev H^1 gradients obtained at the first iteration. In the first place, we observe that as anticipated in Section 3.2.2 the L_2 gradients indeed exhibit quite irregular behaviour lacking necessary smoothness which makes them unsuitable for the reconstruction of constitutive relations with required properties, cf. (3.10). On the other hand, the gradients extracted in the Sobolev space H^1 are characterized by the required smoothness and therefore hereafter we will solely use the Sobolev gradients. Next, in Figure 4.12 we present the results of a diagnostic test commonly employed to verify the correctness of the cost functional gradient [43]. It consists in computing directional Gâteaux differential $\mathcal{J}'(\theta; \theta')$ for some selected perturbations θ' in two different ways, namely, using a finite–difference approximation and using (3.29) which is based on the adjoint field, and then

examining the ratio of the two quantities, i.e.,

$$\kappa(\epsilon) \triangleq \frac{\epsilon^{-1}\left[\mathcal{J}(\theta+\epsilon\theta')-\mathcal{J}(\theta)\right]}{\int_{-\infty}^{+\infty}\boldsymbol{\nabla}_\theta\mathcal{J}(s)\,\theta'(s)\,ds} \tag{4.11}$$

for a range of values of ϵ. If the gradient $\boldsymbol{\nabla}_\theta\mathcal{J}(\theta)$ is computed correctly, then for intermediate values of ϵ, $\kappa(\epsilon)$ will be close to the unity. Remarkably, this behavior can be observed in Figure 4.12 over a range of ϵ spanning about 6 orders of magnitude for three different perturbations $\theta'(T)$. Furthermore, we also emphasize that refining the time step Δt used in the time–discretization of (3.1)–(3.2) and (3.18)–(3.19) yields values of $\kappa(\epsilon)$ closer to the unity. The reason is that in the "optimize–then–discretize" paradigm adopted here such refinement of discretization leads to a better approximation of the continuous gradient (3.29). We add that the quantity $\log_{10}|\kappa(\epsilon)-1|$ plotted in Figure 4.12b shows how many significant digits of accuracy are captured in a given gradient evaluation. As can be expected, the quantity $\kappa(\epsilon)$ deviates from the unity for very small values of ϵ, which is due to the subtractive cancelation (round–off) errors, and also for large values of ϵ, which is due to the truncation errors, both of which are well–known effects.

4.4 Reconstruction Results

4.4.1 Reconstructions on Different Identifiability Intervals

We solve minimization problem (3.9) using the Steepest Descent (SD), Conjugate Gradient (CG) and BFGS (Broyden–Fletcher–Goldfarb–Shanno) algorithms [33] and, unless indicated otherwise, using Sobolev gradients computed

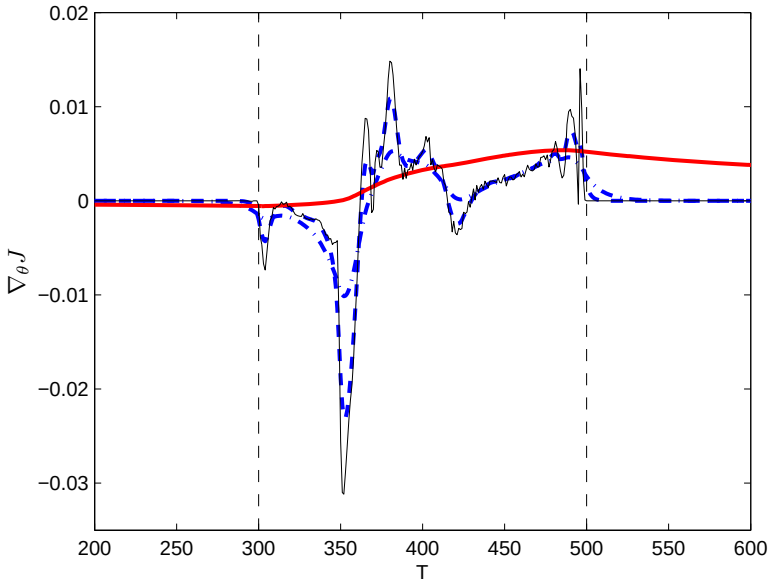

Figure 4.11: Comparison of (thin solid line) the L_2 gradient $\boldsymbol{\nabla}^{L_2}\mathcal{J}$ and the Sobolev gradients $\boldsymbol{\nabla}^{H^1}\mathcal{J}$ defined in (3.31) and for different values of the smoothing coefficient (thick dashed line) $\ell = 2.5$, (thick dash–dotted line) $\ell = 10.0$ and (thick solid line) $\ell = 200.0$ (scaled with multiplier 10) at the first iteration with the initial guess $\mu_0 = const = 0.0177$. The vertical dashed lines represent the boundaries of the identifiability interval $\mathcal{I}$.

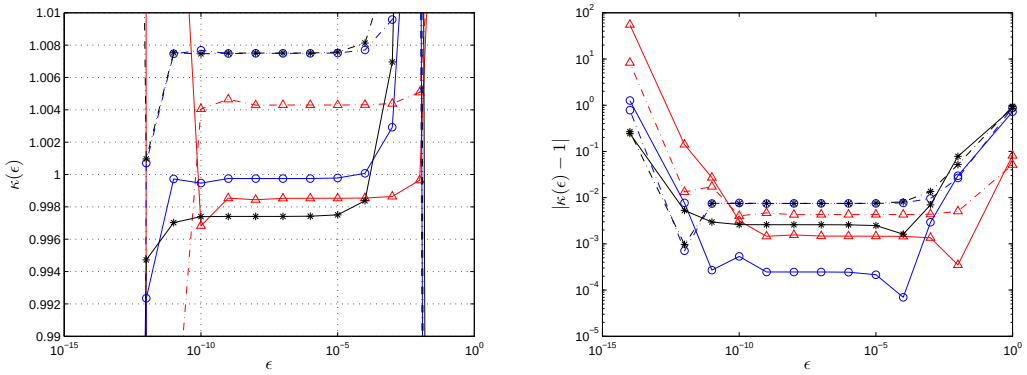

(a) (b)

Figure 4.12: The behavior of (a) $\kappa(\epsilon)$ and (b) $\log|\kappa(\epsilon)-1|$ as a function of ϵ for different perturbations (triangles) $\theta'(T)=\frac{10}{T}$, (circles) $\theta'(T)=e^{-\frac{T}{1000}}$ and (asterisks) $\theta'(T)=-\frac{T^2}{90000}+\frac{2T}{225}+\frac{2}{9}$. The time steps used in the time integration of (3.1)–(3.2) and (3.18)–(3.19) are (dash–dotted line) $\Delta t=5.0\cdot10^{-3}$ and (solid line) $\Delta t=5.0\cdot10^{-4}$.

with $\ell = 200.0$ which was found by trial–and–error to result in the fastest rate of convergence of iterations (3.14). The termination condition used was $\left|\frac{\mathcal{J}(\theta^{(n)})-\mathcal{J}(\theta^{(n-1)})}{\mathcal{J}(\theta^{(n-1)})}\right| < 10^{-6}$. The behavior of the cost functional $\mathcal{J}(\theta^{(n)})$ as a function of the iteration count n is shown in Figure 4.13a for all three minimization algorithms (SD, CG and BFGS). We note that in all cases a decrease over several orders of magnitude is observed in just a few iterations. Despite the fact that steepest descent and conjugate gradient methods show approximately the same performance in terms of rate of convergence, hereafter we will use only the steepest descent method for our computations in this work. This choice is supported by outstanding results shown by SD in further computations producing higher rate of convergence and termination at lower values of cost functional $\mathcal{J}(\theta)$ than CG method. Poorer than anticipated performance of the CG and also the BFGS methods in the current problem can be explained in the following way. Both methods are known to exhibit rate of convergence

superior to the SD approach in the case when the objective functional can be well approximated by a quadratic function. In the present problem we may suspect that this is happening only within the neighbourhoods of the local minimizers which are actually quite small.

The effect of the different initial guesses μ_0 on the decrease of the cost functional is illustrated in Figure 4.13b. Again, in all cases the sufficient decrease over 5–6 orders of magnitude is observed for all types of initial guesses the correspondent reconstruction results for which are presented in Figures 4.14a and 4.15. Reconstructions $\hat{\mu}(T)$ of the constitutive relation obtained using the initial guess $\mu_0 = \frac{C_1}{2}\left(e^{C_2/T_\alpha} + e^{C_2/T_\beta}\right) = 0.0177$ and the optimization time windows with $t_f = \frac{1}{4}, \frac{1}{2}, 1$ are shown in Figure 4.14. Comparing the accuracy of the reconstruction obtained for these different time windows, we can conclude that better results are achieved on shorter time windows $t_f = \frac{1}{4}, \frac{1}{2}$. Given considerations of the computational time, hereafter we will therefore focus on the case with $t_f = \frac{1}{4}$.

In Figure 4.15 we show the reconstructions $\hat{\mu}(T)$ of the constitutive relation obtained from different initial guesses such as constant values of μ_0, $\mu_0(T)$ varying linearly with the temperature T and μ_0 given as a rescaling of the true relationship $\tilde{\mu}$. As mentioned earlier, the correspondent decrease of the cost functional for each reconstruction is shown in Figure 4.13b. The best results are obtained in the cases where some prior information about the true material property is already encoded in the initial guess μ_0, such as the slope, cf. Figure 4.15c, or the exponent, cf. Figure 4.15d. We may also conclude that, since all the reconstructions shown in Figures 4.14 and 4.15 are rather different, the iterations starting from different initial guesses converge in fact to different local minimizers. However, it should be emphasized that in all cases the reconstructions do capture the main qualitative

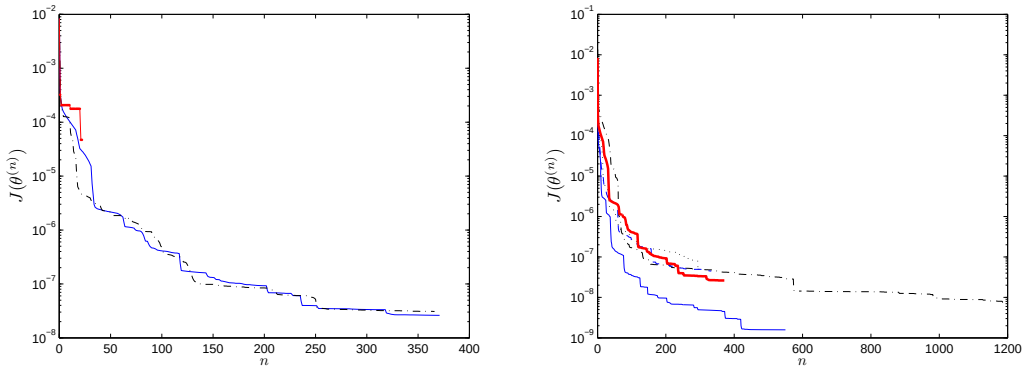

(a) (b)

Figure 4.13: (a) Decrease of the cost functional $\mathcal{J}(\theta^{(n)})$ with iterations n using the Sobolev gradient $\boldsymbol{\nabla}^{H^1}\mathcal{J}$ defined in (3.31) and obtained with (solid line) steepest descent, (dash dotted line) conjugate gradient and (line with dots) BFGS methods with $\ell = 200.0$ and initial guess $\mu_0 = 0.0177$. (b) Decrease of the cost functional $\mathcal{J}(\theta^{(n)})$ with iterations n for different initial guesses: (dots) $\mu_0 = \tilde{\mu}(T_\alpha) = 0.0280$, (dash–dotted line) $\mu_0 = \tilde{\mu}(T_b) = 0.0042$, (dashed line) varying linearly between $\tilde{\mu}(T_\alpha)$ and $\tilde{\mu}(T_\beta)$, (thin solid line) $\mu_0 = \frac{1}{2}\tilde{\mu}(T)$ and (thick solid line) $\mu_0 = 0.0177$.

features of the actual material property with differences becoming apparent only outside the measurement span interval $\mathcal{M}$. In order to make our tests more challenging, in the subsequent computations we will use the initial guess $\mu_0 = \frac{1}{2}\left(\tilde{\mu}(T\alpha) + \tilde{\mu}(T_\beta)\right) = 0.0177$ (cf. Figure 4.14) which contains little prior information about the true material property.

In the remainder of this Section we illustrate two approaches for extending the identifiability region $\mathcal{I}$. We recall that the goal is to extend the range of the state variable T on which one can accurately reconstruct the constitutive relation so as to cover the entire interval $\mathcal{L}$. As already indicated in Section 3.2.2, this is accomplished by making a suitable choice of the time–dependent temperature boundary conditions (3.2b).

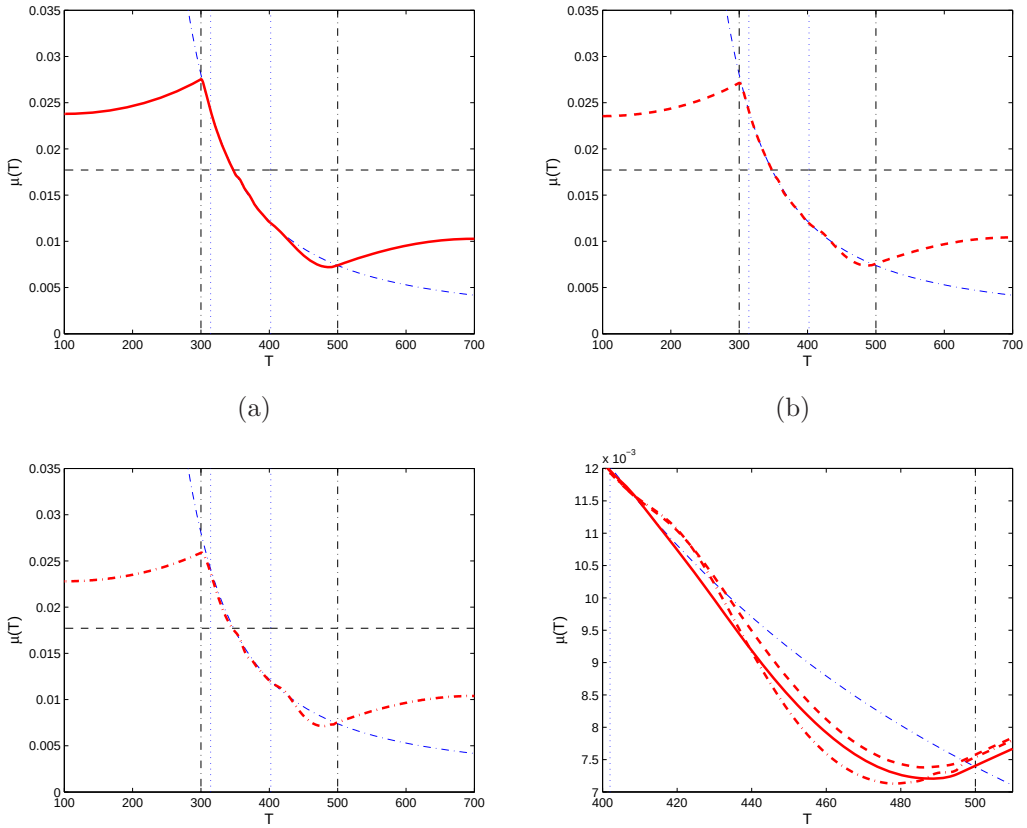

Figure 4.14: Reconstruction $\hat{\mu}(T)$ of the constitutive relation obtained using the Sobolev gradients defined in (3.31) on (a,b,c) the interval $\mathcal{L}$ and (d) close–up view showing the interval outside the identifiability region $\mathcal{I}$ with the time window $[0, t_f]$, where (a) $t_f = \frac{1}{4}$ (b) $t_f = \frac{1}{2}$ and (c) $t_f = 1$. The dash–dotted line represents the true constitutive relation (4.1), the thick solid, dashed and dash dotted lines are the reconstructions for (a,d) $t_f = \frac{1}{4}$, (b,d) $t_f = \frac{1}{2}$ and (c,d) $t_f = 1$ correspondingly, whereas the dashed line represents the initial guess $\mu_0 = 0.0177$; the vertical dash–dotted and dotted lines represent respectively the boundaries of the identifiability interval $\mathcal{I}$ and the measurement span $\mathcal{M}$.

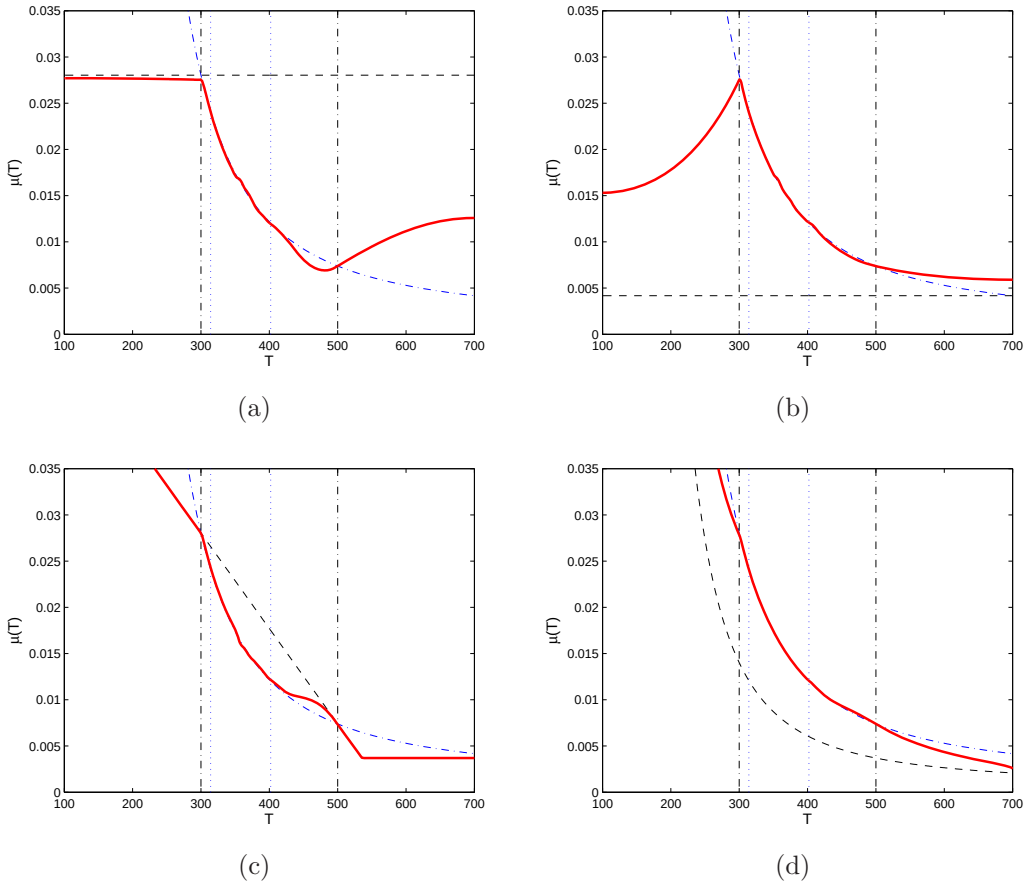

Figure 4.15: Reconstruction $\hat{\mu}(T)$ of the constitutive relation obtained using different initial guesses (a) $\mu_0 = \tilde{\mu}(T_\alpha) = 0.0280$, (b) $\mu_0 = \tilde{\mu}(T_b) = 0.0042$, (c) $\mu_0(T)$ varying linearly between $\tilde{\mu}(T_\alpha)$ and $\tilde{\mu}(T_\beta)$ and (d) $\mu_0 = \frac{1}{2}\tilde{\mu}(T)$, and the Sobolev gradients defined in (3.31) on the interval $\mathcal{L}$. The dash–dotted line represents the true constitutive relation (4.1), the solid line is the reconstruction, whereas the dashed line represents the initial guess μ_0; the vertical dash–dotted and dotted lines represent, respectively, the boundaries of the identifiability interval $\mathcal{I}$ and the measurement span $\mathcal{M}$.

Firstly, we do this by solving a new reconstruction problem where boundary conditions (3.2b) are chosen to vary in time as described in Section 3.2.2, namely

$$T_b = T_b^0 + \frac{h_e}{\Delta t}\, t, \tag{4.12}$$

where T_b^0 are boundary conditions which provide reconstruction on the identifiability interval $\mathcal{I}_0 = [T_\alpha, T_\beta]$, e.g. set up as described in Section 4.1.2, h_e is an extension step and Δt is the step in time discretization. Applying boundary conditions (4.12) allows one to perform the reconstruction on the new identifiability interval $\mathcal{I} = [T_\alpha, T_\beta + h_e]$ if $h_e > 0$ and $\mathcal{I} = [T_\alpha - h_e, T_\beta]$ if $h_e < 0$, hence performing the extension of $\mathcal{I}$ to higher and lower temperatures, respectively.

Results obtained with this approach extending the identifiability interval in one direction only (towards larger values of T) are shown in Figure 4.16. The identifiability region $\mathcal{I}$ is extended from its initial range $\mathcal{I}_0 = [300.0, 500.0]$ to new ranges of $[300.0, 600.0]$ and $[300.0, 700.0]$, corresponding to $h_e = 100.0$ and $h_e = 200.0$, respectively, in (4.12). We observe that, as compared to the reconstruction performed on $\mathcal{I}_0$, now a good estimate of the material property $\mu(T)$ is obtained for a much broader range of T, although the quality of this reconstruction slowly degrades in the direction in which the interval $\mathcal{I}$. is extended, i.e., towards larger values of T.

Then in Figure 4.17 we present the reconstruction $\hat{\mu}(T)$ where the identifiability region $\mathcal{I}$ is extended from its initial range $\mathcal{I}_0$ to new ranges $[290.0, 500.0]$ and $[250.0, 500.0]$ which is performed using $h_e = -10$ and $h_e = -50$, respectively, in (4.12). Even though the decrement $h_e = -10$ causes approximately the same relative changes in the values of $\mu(T)$ as the increment $h_e = 200$, as evident from Figures 4.17(a,b), the reconstruction $\hat{\mu}(T)$ is rather poor on the new interval $[290.0, 300.0]$. Extension of the interval $\mathcal{I}_0$ towards

smaller values with a larger decrement, e.g. $h_e = -50$, performs slightly better, as shown in Figures 4.17(c,d), however, at the cost of deterioration of smoothness of $\hat{\mu}$ on the original identifiability interval $\mathcal{I}_0$.

In our second approach we performed reconstructions of the constitutive relation $\mu(T)$ assuming that the identifiability interval $\mathcal{I}$ coincides with the reconstruction interval $\mathcal{L}$ by specifying the boundary condition in (3.2b) as follows

$$\begin{aligned} T_b|_{\text{top}} &= T_b, \\ T_b|_{\text{else}} &= T_a \end{aligned} \tag{4.13}$$

ensuring that $\mathcal{I} = \mathcal{L}$. We thus perform reconstructions on the intervals $[300, 600]$ (Figures 4.18(a,b)), $[300, 700]$ (Figures 4.18(c,d)), $[290, 500]$ (Figures 4.19(a,b)) and $[250, 500]$ (Figures 4.19(c,d)) which are in fact equivalent to extending the original identifiability interval $\mathcal{I}_0$, respectively, using the increments $h_e = 100, 200$ and the decrements $h_e = -10, -50$. As is evident from both Figures 4.18 and 4.19, these reconstructions produce much better results.

Finally, in Figure 4.20 we present the reconstruction $\hat{\mu}(T)$ extending the identifiability region $\mathcal{I}_0$ in both directions, so that the new identifiability region is $[250.0, 700.0]$. Figures 4.20(a,b) show the reconstruction obtained by means of the first approach described in Section 3.2.2 and formula (4.12), while the Figures 4.20(c,d) show the reconstruction $\hat{\mu}(T)$ performed with the second approach discussed above (setting $\mathcal{I} = \mathcal{L}$ in (4.13)). We observe that in this case as well good reconstruction of the constitutive relation $\mu(T)$ was obtained on the entire interval $\mathcal{L}$ with the use of the second approach.

We close this Section by concluding that the accurate reconstruction on different intervals $\mathcal{L}$ can be achieved by adjusting the identifiability region via a suitable choice of temperature boundary conditions (3.2b). This process can

be interpreted as adjusting the conditions of the experiment used to obtain the measurements $\{\tilde{T}_i\}_{i=1}^{M}$.

4.4.2 Reconstruction in the Presence of Noise

In this Section we first assess the effect of noise on the reconstruction without the Tikhonov regularization and then study the efficiency of the regularization techniques introduced in Section 3.2.3. In Figure 4.21(a,b) we revisit the case already presented in Figure 4.14a (reconstruction on the interval $\mathcal{L} = [100.0, 700.0]$ with identifiability region $\mathcal{I} = [300.0, 500.0]$), now for measurements contaminated with 0.05%, 0.1%, 0.3%, 0.5% and 1.0% uniformly distributed noise (in the same way as described in Section 2.6.3) and without Tikhonov regularization. We may note that the noise level we implement for the current problem is much lower than those which we used for the simple "toy" problem in Chapter 2 where the maximum noise level was 10%. Due to the time dependency of our multiphysics model, uniformly distributed noise is incorporated into measurements at every time step, and therefore tends to accumulate the error in the solution for the direct problem (3.1)–(3.2). As expected, we see that increasing level of noise from 0% to 1.0% leads to oscillatory instabilities developing in the reconstructed constitutive relations $\mu(T)$ comparable to those seen earlier for the simple model in Chapter 2.

The effect of the Tikhonov regularization is studied in Figure 4.21(c,d), where we illustrate the performance of the technique described in Section 3.2.3, cf. (3.33), on the reconstruction problem with 1.0% noise in the measurement data (i.e., the "extreme" case presented in Figures 4.21(a,b)). In terms of the (constant) reference function we take $\overline{\theta} = \sqrt{\mu_0 - m_\mu}$, where $\mu_0 = 0.0177$. We note that by increasing the values of the regularization parameter λ in (3.33)

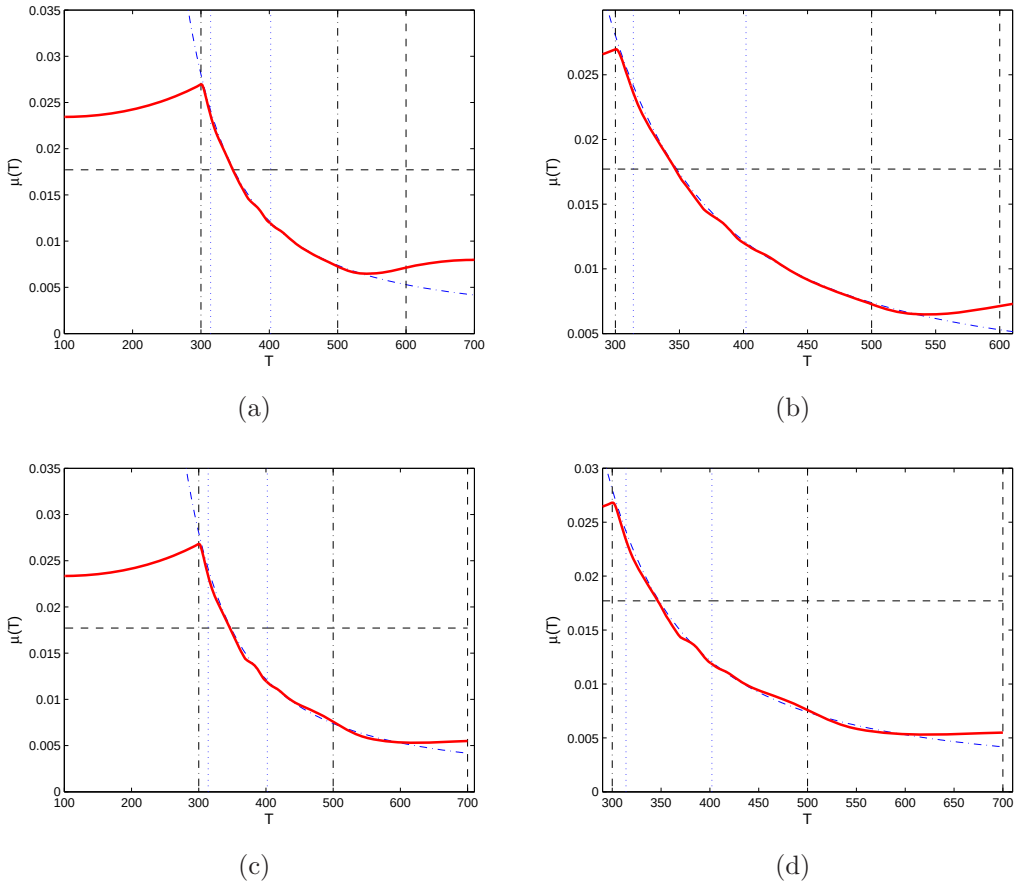

Figure 4.16: Reconstruction $\hat{\mu}(T)$ of the constitutive relation on the extended identifiability region: (a,c) the interval $\mathcal{L}$, (b,d) magnification of the new identifiability region. The dash–dotted line represents the true constitutive relation (4.1), the solid line is the reconstruction $\hat{\mu}(T)$ after extending the identifiability interval $\mathcal{I}_0$ using formula (4.12) with the increments (a,b) $h_e = 100.0$ and (c,d) $h_e = 200.0$. The dashed line represents the initial guess μ_0, the vertical dash–dotted and dotted lines represent respectively the boundaries of the initial identifiability interval $\mathcal{I}_0 = [300.0, 500.0]$ and the measurement span $\mathcal{M}$, while the dashed vertical line shows the right boundary of the new identifiability interval (a,b) $T_\beta = 600$ and (c,d) $T_\beta = T_b = 700$.

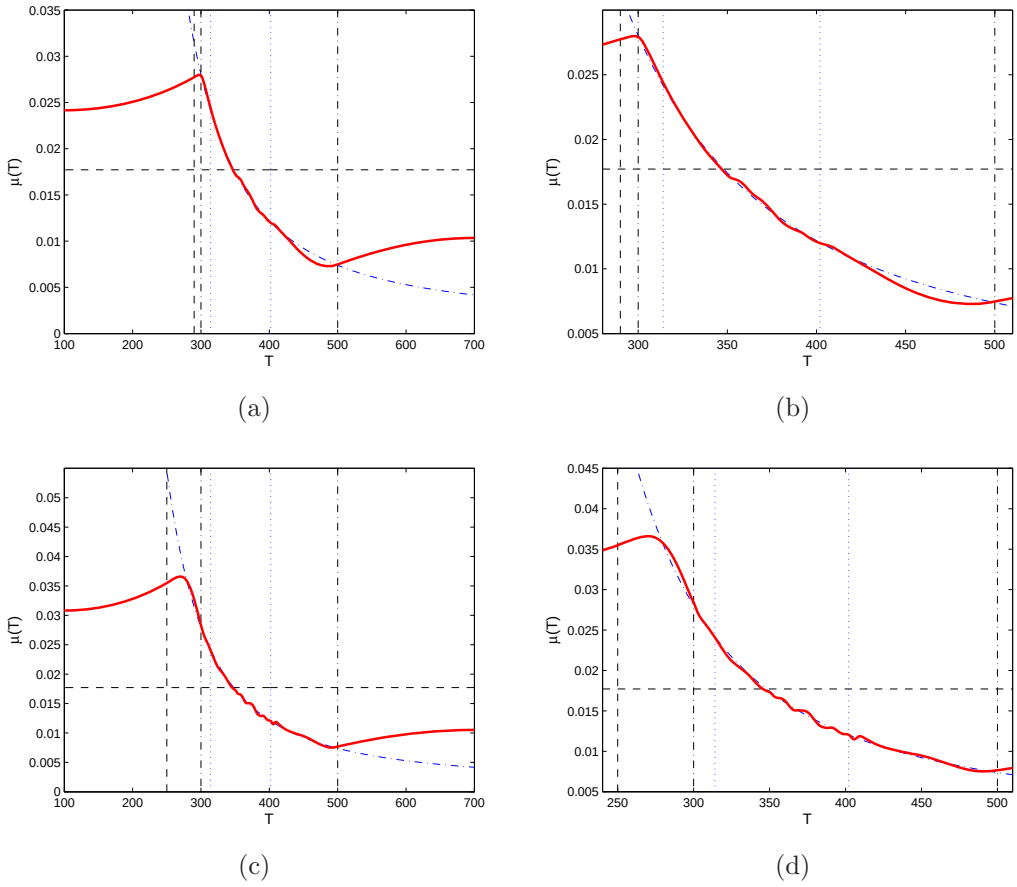

Figure 4.17: Reconstruction $\hat{\mu}(T)$ of the constitutive relation on the extended identifiability region: (a,c) the interval $\mathcal{L}$, (b,d) magnification of the new identifiability region. The dash–dotted line represents the true constitutive relation (4.1), the solid line is the reconstruction $\hat{\mu}(T)$ extending the identifiability interval $\mathcal{I}_0$ using formula (4.12) with the decrements (a,b) $h_e = -10.0$ and (c,d) $h_e = -50.0$, whereas the dashed line represents the initial guess μ_0; the vertical dash–dotted and dotted lines represent respectively the boundaries of the initial identifiability interval $\mathcal{I}_0 = [300.0, 500.0]$ and the measurement span $\mathcal{M}$, while the dashed vertical line shows the left boundary of the new identifiability interval (a,b) $T_\alpha = 290$ and (c,d) $T_\alpha = 250$.

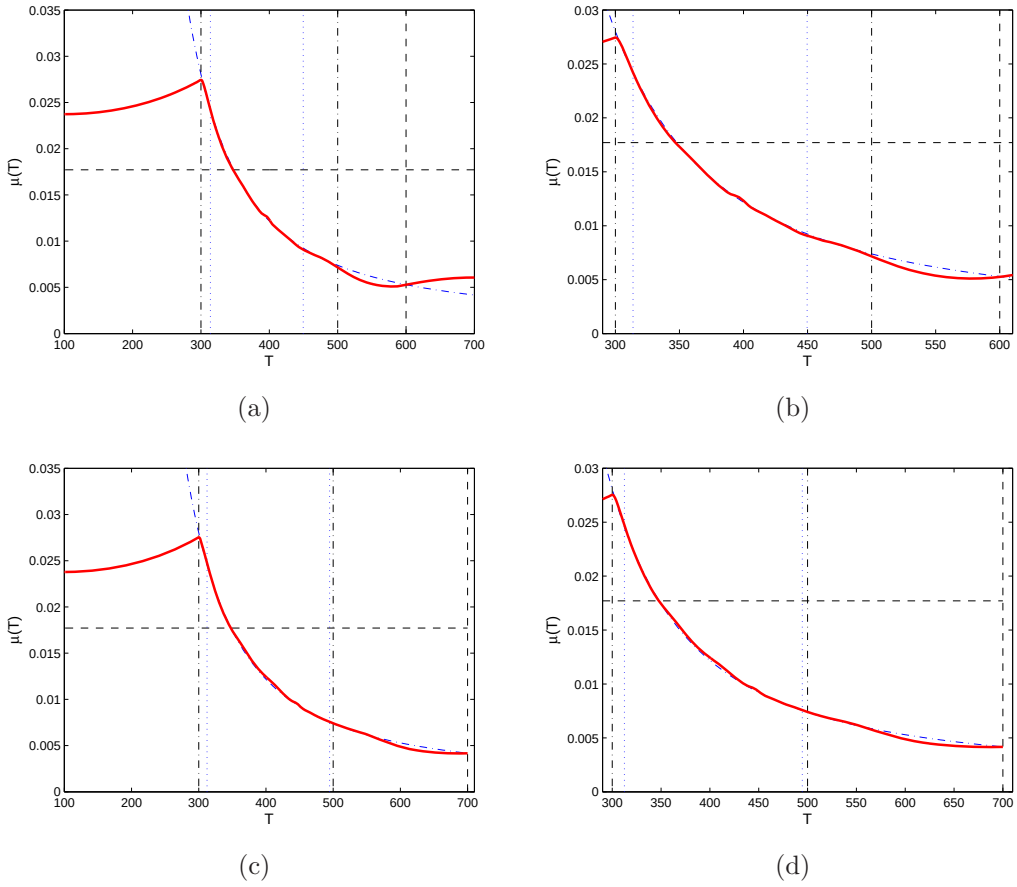

Figure 4.18: Reconstruction $\hat{\mu}(T)$ of the constitutive relation on the new identifiability region $\mathcal{I}$ using formula (4.13) equivalent to extending $\mathcal{I}_0$ with the increments (a,b) $h_e = 100.0$ and (c,d) $h_e = 200.0$; (a,c) the interval $\mathcal{L}$, (b,d) magnification of the identifiability region. The dash–dotted line represents the true constitutive relation (4.1), the solid line is the reconstruction $\hat{\mu}(T)$, whereas the dashed line represents the initial guess μ_0; the vertical dash–dotted and dotted lines represent respectively the boundaries of the original identifiability interval $\mathcal{I}_0 = [300.0, 500.0]$ and the measurement span $\mathcal{M}$, while the dashed vertical line shows the right boundary of the new identifiability interval (a,b) $T_\beta = 600$ and (c,d) $T_\beta = T_b = 700$.

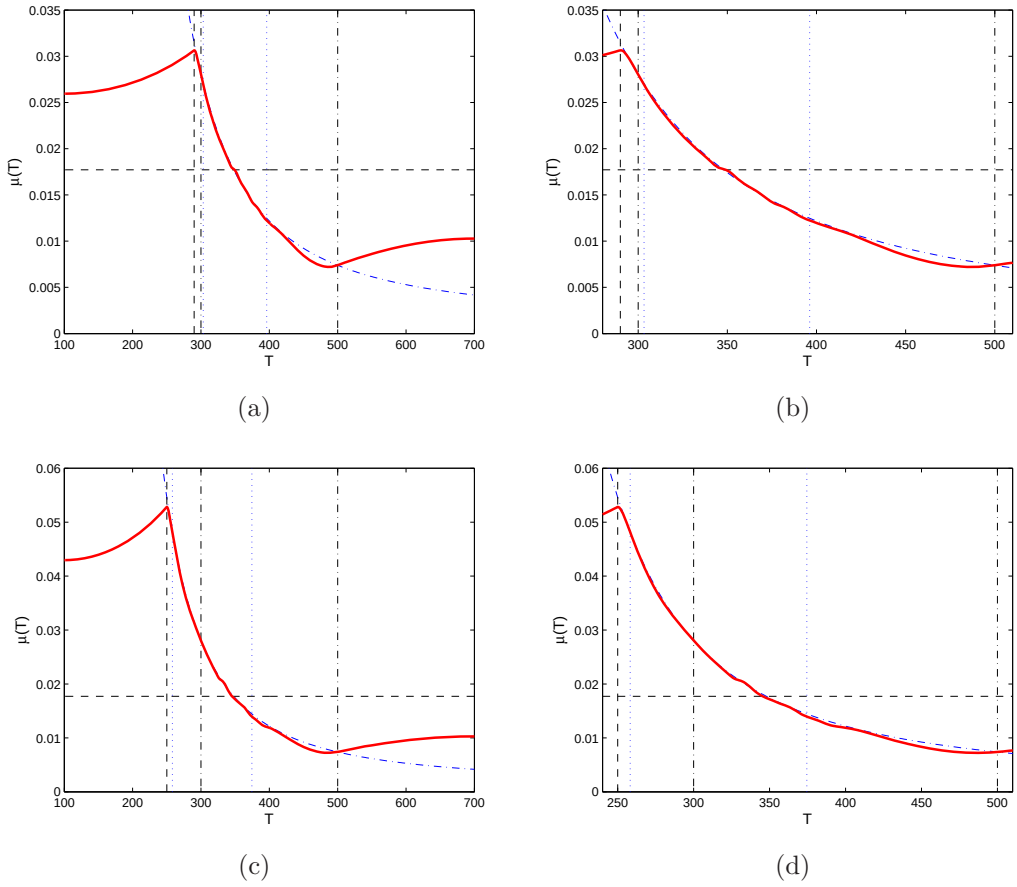

Figure 4.19: Reconstruction $\hat{\mu}(T)$ of the constitutive relation on the new identifiability region $\mathcal{I}$ using formula (4.13) equivalent to extending $\mathcal{I}_0$ with the decrements (a,b) $h_e = -10.0$ and (c,d) $h_e = -50.0$: (a,c) the interval $\mathcal{L}$, (b,d) magnification of the identifiability region. The dash–dotted line represents the true constitutive relation (4.1), the solid line is the reconstruction $\hat{\mu}(T)$, whereas the dashed line represents the initial guess μ_0; the vertical dash–dotted and dotted lines represent respectively the boundaries of the original identifiability interval $\mathcal{I}_0 = [300.0, 500.0]$ and the measurement span $\mathcal{M}$, while the dashed vertical line shows the left boundary of the new identifiability interval (a,b) $T_\alpha = 290$ and (c,d) $T_\alpha = 250$.

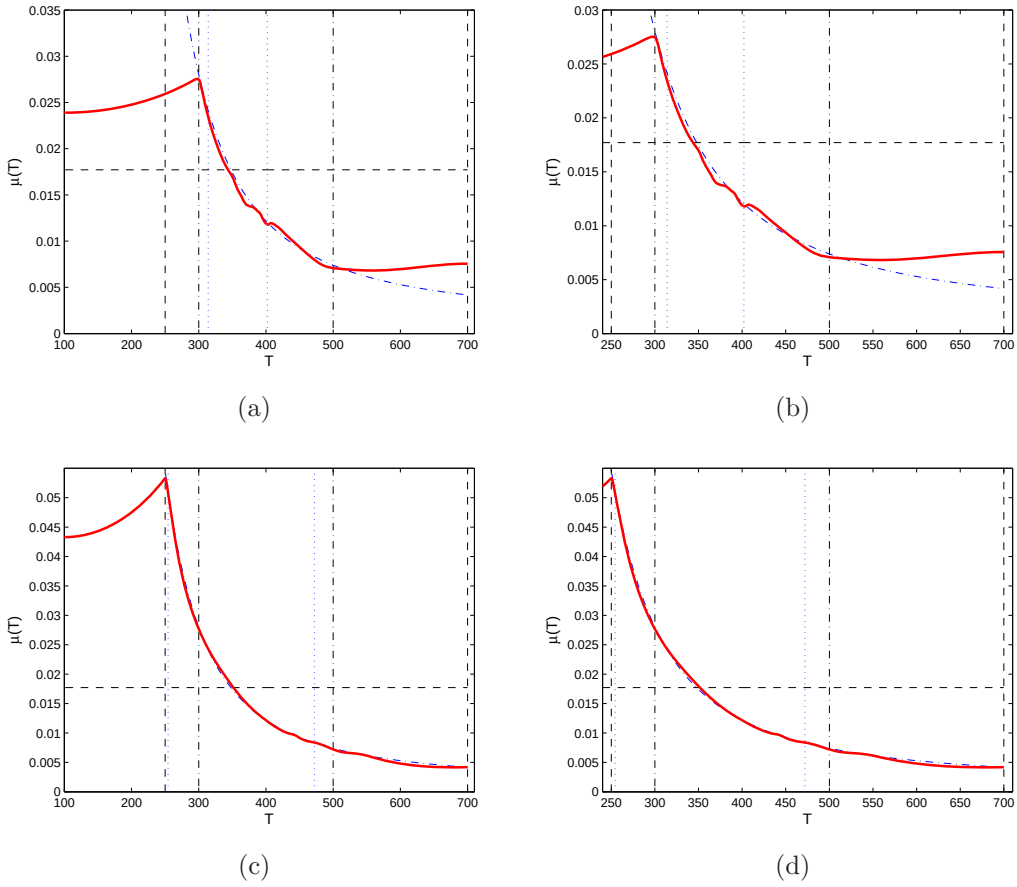

Figure 4.20: Reconstruction $\hat{\mu}(T)$ of the constitutive relation on the extended identifiability region in both directions: (a,c) the interval $\mathcal{L}$, (b,d) magnification of the new identifiability region using (a,b) extending techniques described in Section 3.2.2 and formula (4.12) and (c,d) in formula (4.13). The dash–dotted line represents the true constitutive relation (4.1), the solid line is the reconstruction $\hat{\mu}(T)$, whereas the dashed line represents the initial guess μ_0; the vertical dash–dotted and dotted lines represent respectively the boundaries of the original identifiability interval $\mathcal{I}_0 = [300.0, 500.0]$ and the measurement span $\mathcal{M}$, while the dashed vertical line shows the boundaries of the new identifiability interval $[250.0, 700.0]$.

from 0 (no regularization) to 2500 we manage to eliminate the instabilities caused by the presence of noise in the measurements and obtain as a result smoother constitutive relations, cf. Figure 4.21(c,d). We add that, while after introducing the Tikhonov regularization the reconstructed solutions converge in fact to different local minimizers (in comparison with the reconstructions without noise), however, we emphasize that this does not prevent the reconstructions from capturing the main qualitative features of the actual material property. Systematic methods for determining optimal values of regularization parameters are discussed for instance in [40–42]. Finally, in Figure 4.22 we present the relative reconstruction errors $\|\hat{\mu} - \tilde{\mu}\|_{L_1(\mathcal{I})} / \|\tilde{\mu}\|_{L_1(\mathcal{I})}$ obtained using the approach reported earlier in Section 3.2.3 for data with different noise levels and averaged over 10 noise samples. From Figure 4.22 we conclude that larger values of the regularization parameter λ are required for more noisy measurements. We close this Section by concluding, in agreement with our earlier results reported in Chapter 2, that Tikhonov regularization performs as expected in problems with noise present in the measurement data. We also discussed the ways of improving the performance of this regularizing approach earlier at the end of Section 2.6.3.

4.5 Summary of Results for the Multiphysics Problem

In Chapters 3 and 4 we extended the approach of the reconstruction of the solution–dependent material properties to more complex multiphysics phenomena to validate its applicability for time–dependent systems where the reconstructed property used in one conservation equation is a function of a

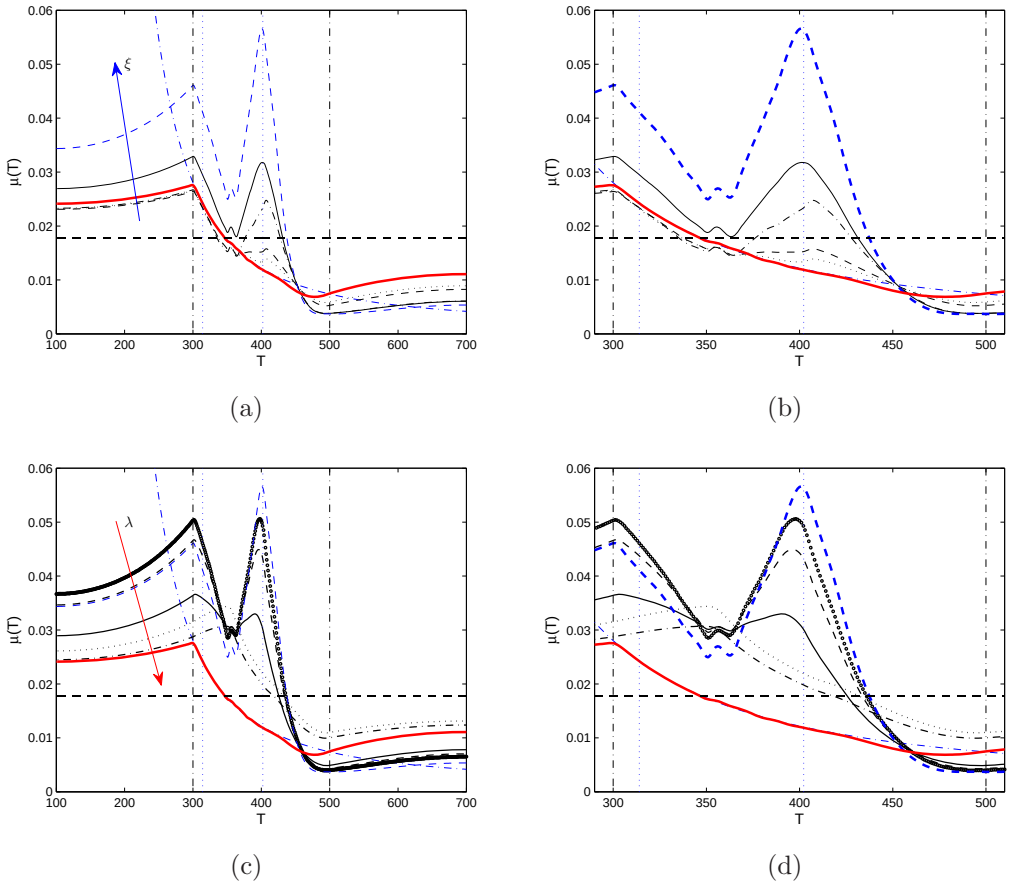

Figure 4.21: (a,b) Reconstruction $\hat{\mu}(T)$ of the material property obtained in the presence of different noise levels in the measurement data: (thick solid line) no noise, (dotted line) 0.05%, (dashed line) 0.1%, (dash–dotted line) 0.3%, (thin solid line) 0.5%, and (thick dashed line) 1.0% on (a) the interval $\mathcal{L}$ and (b) close–up view showing the identifiability interval $\mathcal{I}$. (c,d) Effect of Tikhonov regularization on the reconstruction from the measurement data with 1.0% noise using regularization term (3.33) on (c) the interval $\mathcal{L}$ and (d) close–up view showing the identifiability interval $\mathcal{I}$. In both figures (c,d) the following values of the regularization parameter were used: (thick dashed line) $\lambda = 0$, (circles) $\lambda = 2.5$, (dashed line) $\lambda = 6.25$, (thin solid line) $\lambda = 25.0$, (dash–dotted line) $\lambda = 250.0$, and (dots) $\lambda = 2500.0$. For all figures the horizontal dashed line represents the initial guess $\mu_0 = 0.0177$; the vertical dash–dotted and dotted lines represent, respectively, the boundaries of the identifiability interval $\mathcal{I}$ and the measurement span $\mathcal{M}$. The arrows indicate the trends with increasing (a) noise level ξ and (c) regularization parameter λ.

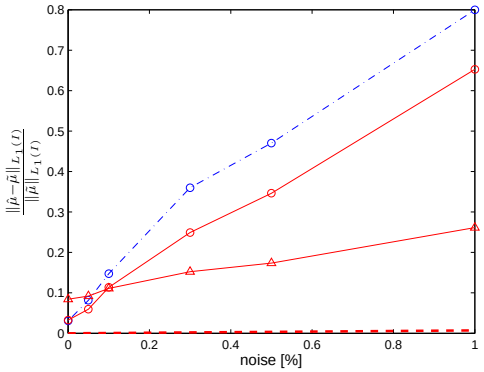

Figure 4.22: Relative L_1 reconstruction errors $\|\hat{\mu} - \tilde{\mu}\|_{L_1(\mathcal{I})} / \|\tilde{\mu}\|_{L_1(\mathcal{I})}$ obtained in the presence of noise with the amplitude indicated and averaged over 10 samples: (dash–dotted line) reconstruction with Sobolev gradients and without Tikhonov regularization, and (solid line) reconstruction with $\dot{H}^1$ Tikhonov regularization term (3.33) [(circles) $\lambda = 2.5$, (triangles) $\lambda = 250.0$]. The thick dashed line represents the "error" in the exact material property (4.1) obtained by adding noise to T and averaging over time steps.

state variable governed by a different conservation equation. This approach was first developed and validated based on a fairly simple model problem discussed previously in Chapter 2. As an example of complex "multiphysics" phenomena in Chapters 3 and 4 we considered a reconstruction of the temperature dependence of the viscosity coefficient used in the momentum equation where the temperature is governed by a separate energy equation. As a model problem we considered two–dimensional unsteady flows in a lid–driven cavity involving also heat transfer. We showed that an elegant and computationally efficient solution of this inverse problem is obtained by formulating it as a PDE–constrained optimization problem which is solved within the "optimize–then–discretize" framework using a gradient–based descent method. We may note that other approaches are also available for the class of problems considered in Chapters 3 and 4. One may use, for example, a simple approach

for reconstructing the coefficients C_1 and C_2 in Andrade law given by (4.1) assuming that the reconstructed material property could be approximated using a known mathematical expression with some unknown coefficients. We may refer to similar problems considered by Alifanov et al. [12, 13], where in their formulation the dependence of the material property on the state variable was assumed in the form of a spline interpolant, effectively resulting in a finite–dimensional optimization problem usually referred as "discretize–then–optimize" approach. Although good reconstructions were reported for that method, they were obtained for different problems, and therefore direct quantitative comparison with our results presented in Chapters 3 and 4 is not possible. At the same time, implementing a "discretize–then–optimize" approach to the present problems, in addition to the work already described, would be outside the scope of this thesis. We also discussed three different approaches to evaluation of the cost functional gradients which are given in terms of integrals defined on the level sets of the temperature field. The results obtained in computational experiments demonstrate good performance of the algorithm, in particular, it is demonstrated that by suitably adjusting the boundary conditions in the governing system we can stretch the identifiability region.

Chapter 5

Extensions and Open Research Problems

5.1 Simultaneous Reconstruction of Several Material Properties

For the future research, we may consider extensions of the approaches developed in the present work (for both models) and apply them to more complicated problems involving systems of coupled PDEs depending on time and defined on domains in two or three dimensions. In the context of such systems an interesting issue is the reconstruction of constitutive relations in systems involving phase changes. As an example one may consider a problem described in Chapter 3 extended to the multiphase case. At a physical level, it can be described as the spatial domain $\Omega \subset \mathbb{R}^d$, $d = 2, 3$ is divided into N subdomains each occupied by a material in a different phase. Suppose the material in subdomain $\Omega_i \subset \Omega$, $i = 1, \ldots, N$, has temperature–dependent viscosity coefficient $\mu_i : \mathbb{R} \to \mathbb{R}^+$. The system of governing PDEs for the i-th phase can be defined

in a way similar to a problem described in Section 3.1, namely

$$\partial_t \mathbf{u} + \mathbf{u}\cdot\boldsymbol{\nabla}\mathbf{u} + \boldsymbol{\nabla} p - \boldsymbol{\nabla}\cdot\left[\mu_i(T)[\boldsymbol{\nabla}\mathbf{u} + (\boldsymbol{\nabla}\mathbf{u})^T]\right] = 0 \qquad \text{in } \Omega_i, \tag{5.1a}$$

$$\boldsymbol{\nabla}\cdot\mathbf{u} = 0 \qquad \text{in } \Omega_i, \tag{5.1b}$$

$$\partial_t T + \mathbf{u}\cdot\boldsymbol{\nabla} T - \boldsymbol{\nabla}\cdot[k_i\boldsymbol{\nabla} T] = 0 \qquad \text{in } \Omega_i, \tag{5.1c}$$

subject to appropriate initial and interface boundary conditions. The optimal reconstruction $\hat{\mu}$ may be obtained as an unconstrained minimizer of cost functional $\mathcal{J}(\mu_1, \mu_2, \ldots, \mu_N)$, i.e.,

$$\hat{\mu} = [\hat{\mu}_1, \hat{\mu}_2, \ldots, \hat{\mu}_N]^T = \underset{\mu_i\in\mathcal{X}_i\; i=1,\ldots,N}{\operatorname{argmin}} \mathcal{J}(\mu_1, \mu_2, \ldots, \mu_N). \tag{5.2}$$

A problem described in Chapter 3 may also be extended to reconstructing both viscosity μ and heat conductivity k assuming their simultaneous dependence on temperature. The governing system which describes the single–phase problem may be written in the following form

$$\partial_t \mathbf{u} + \mathbf{u}\cdot\boldsymbol{\nabla}\mathbf{u} + \boldsymbol{\nabla} p - \boldsymbol{\nabla}\cdot\left[\mu(T)[\boldsymbol{\nabla}\mathbf{u} + (\boldsymbol{\nabla}\mathbf{u})^T]\right] = 0 \qquad \text{in } \Omega, \tag{5.3a}$$

$$\boldsymbol{\nabla}\cdot\mathbf{u} = 0 \qquad \text{in } \Omega, \tag{5.3b}$$

$$\partial_t T + \mathbf{u}\cdot\boldsymbol{\nabla} T - \boldsymbol{\nabla}\cdot[k(T)\boldsymbol{\nabla} T] = 0 \qquad \text{in } \Omega, \tag{5.3c}$$

and the optimal reconstruction $[\hat{\mu},\, \hat{k}]^T$ may be obtained as an unconstrained minimizer of cost functional $\mathcal{J}(\mu, k)$, i.e.,

$$[\hat{\mu}, \hat{k}]^T = \underset{\mu\in\mathcal{X}_\mu,\, k\in\mathcal{X}_k}{\operatorname{argmin}} \mathcal{J}(\mu, k) \tag{5.4}$$

or with the help of dimensionless parameter $D(T) = \dfrac{\mu(T)}{k(T)}$ resulting in optimal

reconstruction in the simpler form

$$\hat{D} = \underset{D \in \mathcal{X}}{\operatorname{argmin}} \mathcal{J}(D). \tag{5.5}$$

5.2 Free–Boundary Problem

Another example of a similar challenging problem is the recovery of the temperature dependence of the surface tension coefficient in a two–phase flow. As an example of such a system one could consider a droplet falling down in the field of a significant temperature gradient, cf. Figure 5.1. We add that this problem was in fact brought to our attention by our industrial collaborators as a motivation for the research discussed in this dissertation.

In order to describe such a model problem mathematically, we may assume that Ω_L and Ω_G are respectively the liquid (droplet) and gas (ambient environment) domains, $\Omega_L, \Omega_G \subset \mathbb{R}^d$, $d = 2, 3$, and the model system will involve the following dependent variables: velocity $\mathbf{u} : (\bar{\Omega}_L \cup \bar{\Omega}_G) \times (0, t_f] \to \mathbb{R}^d$, pressure $p : (\bar{\Omega}_L \cup \bar{\Omega}_G) \times (0, t_f] \to \mathbb{R}$, temperature $T : (\bar{\Omega}_L \cup \bar{\Omega}_G) \times (0, t_f] \to \mathbb{R}$ and position of the free surface $(\Gamma_{LG} \triangleq \bar{\Omega}_L \cap \bar{\Omega}_G) \times (0, t_f] \in \mathcal{S}^d$, $d = 2, 3$. Thus, we may consider the following equations governing the fluid flow in the two phases and the energy equations governing the temperature fields T_L and T_G (subscripts L and G denote quantities defined in the corresponding phases)

$$\rho_L \frac{\partial \mathbf{u}_L}{\partial t} + \rho_L (\mathbf{u}_L \cdot \boldsymbol{\nabla}) \mathbf{u}_L - \boldsymbol{\nabla} \cdot \boldsymbol{\sigma}_L = \rho_L \mathbf{g} \quad \text{in } \Omega_L, \tag{5.6a}$$

$$\boldsymbol{\nabla} \cdot \mathbf{u}_L = 0 \qquad \text{in } \Omega_L, \tag{5.6b}$$

$$\rho_G \frac{\partial \mathbf{u}_G}{\partial t} + \rho_G(\mathbf{u}_G \cdot \boldsymbol{\nabla})\mathbf{u}_G - \boldsymbol{\nabla} \cdot \boldsymbol{\sigma}_G = \rho_G \mathbf{g} \quad \text{in } \Omega_G, \tag{5.7a}$$

$$\boldsymbol{\nabla} \cdot \mathbf{u}_G = 0 \qquad \text{in } \Omega_G, \tag{5.7b}$$

$$\frac{\partial T_L}{\partial t} + \mathbf{u}_L \cdot \boldsymbol{\nabla} T_L - k_L \Delta T_L = 0 \quad \text{in } \Omega_L, \tag{5.8a}$$

$$\frac{\partial T_G}{\partial t} + \mathbf{u}_G \cdot \boldsymbol{\nabla} T_G - k_G \Delta T_G = 0 \quad \text{in } \Omega_G, \tag{5.8b}$$

where ρ_L and ρ_G are the densities, μ_L and μ_G are the viscosities, k_L and k_G are the heat conductivities in the liquid and gas phase, respectively, and $\mathbf{g} = [0, g_y]^T$ is the gravitational acceleration. System of PDEs (5.6), (5.7) and (5.8) is subject to the following boundary conditions on the liquid–gas interface Γ_{LG}

$$\mathbf{u}_L = \mathbf{u}_G \qquad \text{on } \Gamma_{LG}, \tag{5.9a}$$

$$T_L = T_G \qquad \text{on } \Gamma_{LG}, \tag{5.9b}$$

$$k_L \frac{\partial T_L}{\partial \mathbf{n}} = k_G \frac{\partial T_G}{\partial \mathbf{n}} \qquad \text{on } \Gamma_{LG}, \tag{5.9c}$$

$$\Big[\boldsymbol{\sigma}\Big]_L^G . \mathbf{n} = \gamma(T_L)\ \kappa\ \mathbf{n} \quad \text{on } \Gamma_{LG}, \tag{5.9d}$$

where $\mathbf{n}$ is the unit normal vector on the interface Γ_{LG}, κ is the interface curvature and $\gamma(T_L)$ the surface tension (a *temperature–dependent* material property). For simplicity, on the far boundary Γ_0, cf. Figure 5.1, we may use

simple Dirichlet type boundary condition

$$\mathbf{u}_G = \mathbf{0} \qquad \text{on } \Gamma_0, \tag{5.10a}$$

$$T_G = T_b \qquad \text{on } \Gamma_0. \tag{5.10b}$$

The role of the "experimental" input, i.e. measurements in this problem, will be played by the series of M snapshots of the shape of the falling droplet. In other words, one can record the M locations of the interface $\{\tilde{\Gamma}_{LG}(t_i)\}_{i=1}^{M}$ at different discrete times $\{t_i\}_{i=1}^{M}$, $t_i \in [0, t_f]$. Therefore, the parameter estimation problem can be formulated as follows. Given a set of "measurements" $\{\tilde{\Gamma}_{LG}(t_i)\}_{i=1}^{M}$ of the interface Γ_{LG}, we seek to reconstruct the constitutive relation $\gamma = \gamma(T_L)$ such that the solutions of the problem (5.6)–(5.10) obtained with this reconstructed function $\gamma(T_L)$ will best match the available measurements $\tilde{\Gamma}_{LG}$.

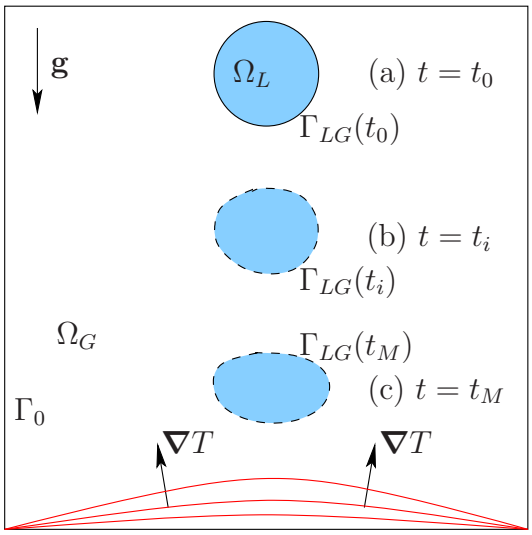

Figure 5.1: Falling droplet model: (a) initial shape of the interface Γ_{LG} at time $t_0 = 0$ and two snapshots recorded at time (b) $t = t_i$ and (c) $t = t_M$ from the series of measurements $\{\tilde{\Gamma}_{LG}(t_i)\}_{i=1}^{M}$.

The idea is to extend the methodology devised in this work to reconstruct a material property defined on an interface from information about the evolution of this interface. While there is a number of technical issues related to solution of PDE–constrained optimization problem in variable domains [62], this reconstruction problem at least in principle appears amenable to treatment with the approach devised in this study.

Chapter 6

Summary and Conclusions

In this study we investigated a novel computational approach to reconstruction of constitutive relations based on incomplete and noisy measurement data. This parameter estimation problem is solved using a gradient–based optimization technique in which the sensitivities of the cost functional with respect to the form of the constitutive relation are computed using a suitably–defined adjoint system. The main challenge inherent in this problem follows from the fact that the control variable is a function of the state, rather than the independent variable in the governing system. We studied the problem in the context of the "optimize–then–discretize" approach to PDE–constrained optimization and demonstrated how one can obtain an expression of the cost functional gradient. We also argued that the traditional L_2 cost functional gradients are discontinuous, or do not have a required degree of regularity, and therefore are unsuitable for reconstruction of smooth constitutive relations. It was shown that this difficulty can be resolved by using the Sobolev gradients defined consistently with the functional setting of the problem in the optimization algorithm. We also proposed and validated a procedure allowing

one to shift, or extend, the identifiability region, and in this way reconstruct the constitutive relation over a much broader range of the state variable. A first set of computational tests demonstrated the feasibility of the proposed approach on a simple 1D model problem providing a proof of concept for the method. We then extended this approach to more complex multiphysics phenomena to demonstrate its applicability to time-dependent systems where the reconstructed property used in one conservation equation is a function of a state variable governed by a different conservation equation. We also addressed the important issue of reconstruction in the presence of random noise in the measurement data, and showed that the classical Tikhonov regularization is able to stabilize the reconstruction process. Our computations indicated that the use of suitable Sobolev gradients in the reconstruction process may also have some regularizing effect. We also addressed a number of computational challenges related to accurate and efficient evaluation of cost functional gradients, which are at a heart of the reconstruction procedure. As these gradients are given in terms of integrals over manifolds defined by a level-set function (in 2D and 3D), we analyze and compare three different methods for evaluation of cost functional gradients. We also demonstrate, both theoretically and computationally, the superior accuracy and efficiency of our novel numerical approach to the evaluation of these gradients.

In regard to the possibility of using the proposed computational approach to reconstruct the constitutive relations in other problems, the following comments are in place:

- The accurate reconstruction on different intervals $\mathcal{L}$ can be achieved by adjusting the identifiability region $\mathcal{I}$ via a suitable choice of temperature boundary conditions. As it was shown for our both model problems,

extension of the identifiability region $\mathcal{I}$ in time–dependent and steady–state problems can be employed in a different way pursuing better performance in reconstruction. For time–dependent problem in general this can be accomplished by making a suitable choice of the time–dependent temperature boundary conditions. The steady–state problem in contrast requires repeating the optimization procedure with new sets of parameters (boundary conditions and/or source terms) to perform extensions in a stepwise manner.

- As expected, the increasing level of noise incorporated into measurements leads to oscillatory instabilities developing in the reconstructed constitutive relations. We note that in the time–independent problem a stable reconstruction of the material property was possible in the presence of a much higher noise level than in the time–dependent problem. This can be explained by accumulation of the error in the solution of the direct time–dependent problem when the uniformly distributed noise is incorporated into measurements at every time step.

- We also note that the use of the cost functional of the quadratic form (in the least square sense) combined with a nonlinear governing PDE leaves the minimization problems in general nonconvex. In our current work as well as in other similar problems this results in the fact that the optimality conditions may characterize only a local, rather than global, minimizer. We add that development of the methods applicable for finding the global minima is beyond the scope of the problems considered in this thesis.

- In regard to reconstruction of constitutive relations in general, it is im-

portant that such relations be consistent with the second principle of thermodynamics. In continuous thermodynamical and mechanical systems this principle is expressed in terms of the Clausius–Duhem inequality. This may therefore require additional constraints whose structure will depend on the complexity of the problem considered. For our present work, it was possible to reduce this principle to the positivity of the reconstructed constitutive relations which can be easily enforced by applying the "slack" variable technique (in the second model problem). This in fact may not be feasible in more complicated multiphysics problems where other specific constraints must be introduced.

Appendices

A Minimum Principle for Problem (2.3)

Theorem A.1 *Let $T \in C^2(\Omega) \cap C^0(\overline{\Omega})$ be a solution of (2.3). If $k(T) > 0$, $\forall\, T \in \mathcal{I}$, and $g(\mathbf{x}) > 0$, $\forall \mathbf{x} \in \Omega$, then*

$$\min_{\mathbf{x}\in\overline{\Omega}} T(\mathbf{x}) = T_\alpha = \min_{\mathbf{x}\in\partial\Omega} T_0(\mathbf{x}),$$

i.e., the minimum is attained on the boundary $\partial\Omega$.

Proof. Although Theorem A.1 may be obtained as a special case from a more general result given in [63], we present here the proof for the sake of completeness. We prove this theorem by contradiction. Let us assume that the minimum of the solution T is attained at an interior point $\tilde{\mathbf{x}} \in \Omega$. Since $\nabla T(\tilde{\mathbf{x}}) = 0$, Equation (2.3a) takes form $-k(T)\,\Delta T = g$ at the point $\tilde{\mathbf{x}}$. Therefore, by continuity, we would have $\Delta T < 0$ in a small neighborhood of $\tilde{\mathbf{x}}$ which would contradict the assumption that $T(\tilde{\mathbf{x}})$ is a minimum. □

B Differentiability of Map (2.5)

In this Appendix we outline the proof of a theorem concerning the differentiability of map (2.5) from the constitutive relations to measurements. In its

main idea our proof is analogous to the proof presented in [11] for a different (time–dependent) problem, however, a number of intermediate estimates are different. We thus consider problem (2.3) in a general bounded domain Ω with a $C^{1,1}$ boundary and start by defining the following functional spaces for the dependent variable T

$$\mathcal{T} = \{T \in H^1(\Omega); T = 0 \text{ on } \partial\Omega\}, \quad H = L_2(\Omega), \quad \mathcal{T}' = H^{-1}(\Omega), \tag{B.1}$$

where for simplicity we have assumed homogeneous Dirichlet data. The inner product $((\cdot,\cdot))_*$ in the dual space $\mathcal{T}'$ is defined as

$$((u,v))_* = (D^{-1}u, D^{-1}v)_{H^1}, \tag{B.2}$$

where $D = \Delta$ is the canonical isomorphism between $\mathcal{T}$ and $\mathcal{T}'$, i.e.,

$$\text{if } u \in \mathcal{T} \quad \Longrightarrow \quad D\,u = \Delta u \in \mathcal{T}'. \tag{B.3}$$

We consider two weak formulations of governing system (2.3), namely, a variational formulation in the space $\mathcal{T}$ defined as follows

$$\int_\Omega k(T)\,\nabla T \cdot \nabla u\, d\mathbf{x} = \int_\Omega g\,u\, d\mathbf{x}, \qquad T, u \in \mathcal{T}, \tag{B.4}$$

and a weaker one obtained from (B.4) by setting $u = D^{-1}w$

$$\int_\Omega V(T) \cdot w\, d\mathbf{x} = ((g,w))_*, \qquad \forall w \in H, \tag{B.5}$$

where $V(T)$ is defined in (2.15). Now, we state a differentiability result for the solution $T = T(\mathbf{x};k)$ of equation (B.4) in which the solution $T(\mathbf{x};k)$ is treated

as an element of $L_2(\Omega)$, cf. (2.5) and (3.5).

Theorem B.1 *Assume that m_k, cf.* (2.4)*, is sufficiently large and solutions of* (2.3) *satisfy $\|\boldsymbol{\nabla} T\|_{L^\infty(\Omega)} < \infty$. Then the map $k \to T(\cdot; k)$ from $\mathcal{K}$ to $L_2(\Sigma)$ defined by* (B.4) *is Fréchet–differentiable in the norm $H^1(\mathcal{I})$.*

Proof. Let k' denote the variation of k such that k, $\check{k} \triangleq k + k' \in \mathcal{K} \subset H^1(\mathcal{I})$. To show differentiability of the map $k \to T(\cdot; k)$ we need to prove the existence of the Fréchet differential T', such that

$$\lim_{\|k'\|_{H^1(\mathcal{I})} \to 0} \frac{\|T(k+k') - T(k) - T'(k;k')\|_{L_2(\Sigma)}}{\|k'\|_{H^1(\mathcal{I})}} = 0. \tag{B.6}$$

For simplicity, we shall use the following notation

$$\mathcal{R} \triangleq T(k+k') - T(k) - T'(k;k'), \quad \check{T} \triangleq T + T' + \mathcal{R}, \quad \delta T \triangleq T' + \mathcal{R}. \tag{B.7}$$

Writing equation (B.5) for $\check{T}$ and T, and subtracting we obtain

$$\int_\Omega \left[V(\check{T}) - V(T)\right] w \, d\mathbf{x} = -\int_\Omega V'(\check{T})\, w \, d\mathbf{x}, \tag{B.8}$$

where, in analogy with (2.15), the integrand on the RHS is defined as

$$V'(\check{T}) = \int_{T_\alpha}^{\check{T}} k'(s)\, ds$$

so that $V(\check{T}) = V(T) - V'(\check{T})$. Next, we postulate that the Fréchet differential T' satisfy the following equation

$$\int_\Omega k(T)\, T' \, w \, d\mathbf{x} = -\int_\Omega V'(T)\, w \, d\mathbf{x}. \tag{B.9}$$

Existence of solutions of (B.9) is established via a straightforward application of Lax–Milgram lemma, since (B.9) is a linear elliptic boundary–value problem. Therefore, our goal now is to prove that $\|\mathcal{R}\|_{L_2(\Sigma)}$, cf. (B.7), vanishes faster that $\|k'\|_{H^1(\mathcal{I})}$. Subtracting (B.9) from (B.8) yields

$$\int_\Omega \left[V(\check{T}) - V(T) - k(T)\,T'\right]\, w\,d\mathbf{x} = -\int_\Omega \left[V'(\check{T}) - V'(T)\right]\, w\,d\mathbf{x}. \tag{B.10}$$

Since $k(T) \in H^1(\mathcal{I})$, it follows from Taylor's theorem that there exist $\theta \in [0,1]$ such that

$$V(\check{T}) = V(T) + k(T)\,\delta T + \frac{1}{2}\dot{k}(T+\theta\delta T)(\delta T)^2, \tag{B.11}$$

almost everywhere in $\mathcal{T}$, where $\dot{k}$ denotes the derivative of k with respect to its argument. Therefore, the left hand side of (B.10) simplifies to

$$\int_\Omega \left[k(T)\,\mathcal{R} + \frac{1}{2}\,\dot{k}(T+\theta\,\delta T)(\delta T)^2\right]\, w\,d\mathbf{x}, \tag{B.12}$$

whereas for the right hand side of (B.10) we use

$$V'(\check{T}) = V'(T) + k'(T+\theta'\,\delta T)\delta T, \tag{B.13}$$

where $\theta' \in [0,1]$. Transforming equation (B.10) with expressions (B.12) and (B.13) yields

$$\int_\Omega k(T)\,\mathcal{R}\,w\,d\mathbf{x} = -\int_\Omega \left[\frac{1}{2}\,\dot{k}(T+\theta\delta T)(\delta T)^2 + k'(T+\theta'\delta T)\delta T\right]\, w\,d\mathbf{x}. \tag{B.14}$$

This is a linear elliptic boundary–value problem for which there exist an *a priori* estimate (see, for example, Section 2.3 in [63])

$$\|\mathcal{R}\|_{L_2(\Omega)} \leqslant \left\| \frac{1}{2}\,\dot{k}(T+\theta\delta T)(\delta T)^2 + k'(T+\theta'\delta T)\delta T \right\|_{L_2(\Omega)}. \tag{B.15}$$

For $k \in \mathcal{K}$ we can reduce inequality (B.15) to the form

$$\|\mathcal{R}\|_{L_2(\Omega)} \leqslant C_1 \|(\delta T)^2\|_{L_2(\Omega)} + \|k'\|_{L_2(\mathcal{I})}\, \|\delta T\|_{L_2(\Omega)}. \tag{B.16}$$

We now proceed to demonstrate that the RHS of (B.16) vanishes faster than $\|k'\|_{H^1(\mathcal{I})}$, i.e., as $\|k'\|^q_{H^1(\mathcal{I})}$ for some $q > 1$. In relation (B.16) and hereafter the symbols C with subscripts and primes will denote different positive constants.

We start with the term $\|\delta T\|_{L_2(\Omega)}$. Writing the original weak form (B.4) for k and $\check{k}$, subtracting and setting $u = \delta T$ produces

$$\int_\Omega \check{k}(\check{T})\,(\nabla \delta T)^2\, d\mathbf{x} + \int_\Omega \left[k(\check{T}) + k'(\check{T}) - k(T)\right] \nabla \delta T \cdot \nabla T\, d\mathbf{x} = 0. \tag{B.17}$$

For $\check{k} \in \mathcal{K}$ we have the following estimate for the first term in (B.17)

$$\int_\Omega \check{k}(\check{T})\,(\nabla \delta T)^2\, d\mathbf{x} \geqslant m_k\, \|\nabla \delta T\|^2_{L_2(\Omega)}. \tag{B.18}$$

Now we need to assume that $C_2 = \|\nabla T\|_{L^\infty(\Omega)} < \infty$, cf. [11]. Then, for the second term in (B.17) we have

$$\begin{aligned} &\int_\Omega \left[k'(\check{T}) + \dot{k}(T+\theta\delta T)\delta T\right] \nabla \delta T \cdot \nabla T\, d\mathbf{x} \\ &\leqslant C_2 \int_\Omega \left[k'(\check{T}) + \dot{k}(T+\theta\,\delta T)\delta T\right] |\nabla \delta T|\, d\mathbf{x}. \end{aligned} \tag{B.19}$$

Next, we combine (B.18) and (B.19) to obtain the inequality

$$m_k \, \|\nabla \delta T\|_{L_2(\Omega)} \leqslant C_1' \, \|k'\|_{L_2(\mathcal{I})} + C_2' \, \|\delta T\|_{L_2(\Omega)}. \tag{B.20}$$

Using the following Poincare inequality $\|\delta T\|_{L_2(\Omega)} \leqslant C_3 \|\nabla \delta T\|_{L_2(\Omega)}$ we see that

$$\begin{aligned} \frac{m_k}{C_3} \|\delta T\|_{L_2(\Omega)} &\leqslant C_1' \|k'\|_{L_2(\mathcal{I})} + C_2' \|\delta T\|_{L_2(\Omega)}, \\ m_k \, \|\nabla \delta T\|_{L_2(\Omega)} &\leqslant C_1' \, \|k'\|_{L_2(\mathcal{I})} + C_2' \, C_3 \, \|\nabla \delta T\|_{L_2(\Omega)}. \end{aligned}$$

Assuming that m_k is sufficiently large, so that $m_k - C_2' \, C_3 > 0$, we obtain

$$\begin{aligned} \|\delta T\|_{L_2(\Omega)} &\leqslant \frac{C_1' \, C_3}{m_k - C_2' \, C_3} \, \|k'\|_{L_2(\mathcal{I})}, \\ \|\nabla \delta T\|_{L_2(\Omega)} &\leqslant \frac{C_1'}{m_k - C_2' \, C_3} \, \|k'\|_{L_2(\mathcal{I})}. \end{aligned} \tag{B.21}$$

Next we estimate $\|(\delta T)^2\|_{L_2(\Omega)} \equiv \|\delta T\|^2_{L_4(\Omega)}$. As a consequence of the Sobolev embedding theorem (see, e.g., Theorem 4.12 in [64]), we have the following inclusion

$$\mathcal{T} \subset H^1(\Omega) = W^{1,2}(\Omega) \subset L_6(\Omega), \quad n \leqslant 3.$$

Therefore, for $\delta T \in \mathcal{T}$ and in the light of estimates (B.21), we obtain

$$\|\delta T\|_{L_6(\Omega)} \leqslant C \, \|\delta T\|_{H^1(\Omega)} \leqslant C' \|k'\|_{L_2(\mathcal{I})}. \tag{B.22}$$

We then use the interpolation theorem (see e.g., Theorem 2.11 in [64]) for the L_p spaces which states that for $\xi \in L_p \cap L_q$, $1 \leqslant p \leqslant r \leqslant q \leqslant \infty$ and $t \in [0, 1]$, we have

$$\|\xi\|_{L_r} \leqslant \|\xi\|^t_{L_p} \, \|\xi\|^{1-t}_{L_q} \quad \Longleftrightarrow \quad \frac{1}{r} = \frac{t}{p} + \frac{1-t}{q}.$$

Applying this result to $\|\delta T\|^2_{L_4(\Omega)}$ with $r = 4, p = 2, q = 6$ we obtain using (B.21) and (B.22)

$$\begin{aligned} \|\delta T\|_{L_4(\Omega)} &\leqslant \|\delta T\|^{\frac{1}{4}}_{L_2(\Omega)} \|\delta T\|^{\frac{3}{4}}_{L_6(\Omega)} \\ \implies \quad \|(\delta T)^2\|_{L_2(\Omega)} = \|\delta T\|^2_{L_4(\Omega)} &\leqslant C''' \|k'\|^2_{L_2(\mathcal{I})}. \end{aligned} \tag{B.23}$$

Finally, substituting estimates (B.21) and (B.23) for $\|\delta T\|_{L_2(\Omega)}$ and $\|(\delta T)^2\|_{L_2(\Omega)}$ into (B.16) we obtain

$$\begin{aligned} \|\mathcal{R}\|_{L_2(\Omega)} &\leqslant C_1 \|(\delta T)^2\|_{L_2(\Omega)} + \|k'\|_{L_2(\mathcal{I})} \|\delta T\|_{L_2(\Omega)} \\ &\leqslant C'''' \|k'\|^2_{L_2(\mathcal{I})} \leqslant C''''' \|k'\|^2_{H^1(\mathcal{I})}, \end{aligned} \tag{B.24}$$

This demonstrates that $\|\mathcal{R}\|_{L_2(\Omega)}$ vanishes faster than $\|k'\|_{H^1(\mathcal{I})}$. Therefore $k \longrightarrow T(\cdot; k)$ is Fréchet–differentiable from $H^1(\mathcal{I})$ to $L_2(\Sigma)$. □

We remark that, as is evident from (B.24), $T(\cdot; k)$ is also differentiable from $L_2(\mathcal{I})$ to $L_2(\Sigma)$.

C Proof of Equivalence of Contour Integral (3.38) and Area Integral (3.37)

To rewrite the integral, given also in (3.37),

$$f(s) = \int_\Omega \delta(\phi(s, \mathbf{x})) g(\mathbf{x})\, d\mathbf{x} \tag{C.1}$$

explicitly as a line integral, we introduce first a local coordinate system (ξ, η), where ξ and η are chosen as the coordinates in the direction tangent and normal to the s–level set of the function $\phi(s, \mathbf{x})$, see Figure C.1. The coordinates (ξ, η) are scaled, so that the Jacobian $J(\mathcal{G})$ of the transformation $\mathcal{G} : (x, y) \to (\xi, \eta)$

is identically equal to the unity, i.e., we require

$$d\mathbf{x} = dx\,dy = \det J(\mathcal{G})\,d\xi\,d\eta = d\xi\,d\eta. \tag{C.2}$$

This condition is satisfied by defining the transformation $\mathcal{G}$ in the following affine form

$$x = \alpha_{\xi/x}\xi\cos\gamma - \alpha_{\eta/y}\eta\sin\gamma + x_0,$$
$$y = \alpha_{\xi/x}\xi\sin\gamma + \alpha_{\eta/y}\eta\cos\gamma + y_0,$$

where $\tan\gamma = f'(x)$ at the point (x_0, y_0) and the curve $y = f(x)$ is defined by the zero–level set $\phi(s,\mathbf{x}) = \phi(s,x,f(x)) = 0$, cf. Figure C.1; $\alpha_{\xi/x}, \alpha_{\eta/y} \in \mathbb{R}$. So that

$$\begin{aligned}\det J(\mathcal{G}) &= \frac{\partial x}{\partial\xi}\frac{\partial y}{\partial\eta} - \frac{\partial x}{\partial\eta}\frac{\partial y}{\partial\xi} \\ &= \alpha_{\xi/x}\alpha_{\eta/y}\cos^2\gamma + \alpha_{\xi/x}\alpha_{\eta/y}\sin^2\gamma = \alpha_{\xi/x}\alpha_{\eta/y} = 1.\end{aligned} \tag{C.3}$$

One may require the coordinate ξ to increase at a uniform rate along the curve $y = f(x)$. To ensure this, we fix $d\xi = d\sigma = \sqrt{(dx)^2 + (dy)^2} = \sqrt{1 + [f'(x)]^2}dx$ and, using (C.3), define $d\eta = \dfrac{dy}{\sqrt{1 + [f'(x)]^2}}$. We thus have

$$d\eta = \left(\frac{\partial\phi}{\partial\eta}\right)^{-1} d\phi$$

which, when used in (C.1), yields

$$\begin{aligned}f(s) &= \int_\Omega \delta(\phi(s,\mathbf{x}))g(\mathbf{x})\;d\mathbf{x} = \int_\Omega \delta(\phi(s,\mathbf{x}))g(\mathbf{x})\;d\xi\,d\eta \\ &= \int_\Omega \delta(\phi(s,\mathbf{x}))g(\mathbf{x})\left(\frac{\partial\phi}{\partial\eta}\right)^{-1} d\phi\;d\xi = \int_{\Gamma_s} g(\mathbf{x})\left(\frac{\partial\phi}{\partial n}\right)^{-1} d\sigma,\end{aligned} \tag{C.4}$$

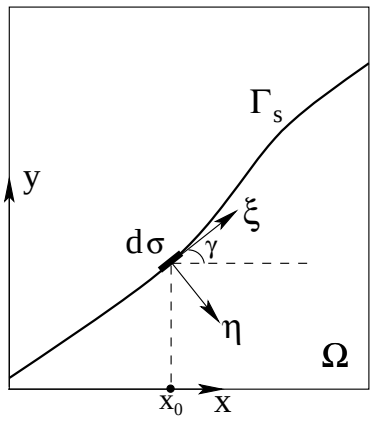

Figure C.1: Level set Γ_s and the local coordinate system (ξ, η) used in the derivation of line integral (3.38).

where we used the standard property of the Dirac delta measure and the fact that $\frac{\partial}{\partial \eta} \equiv \frac{\partial}{\partial n}$. The derivative of $\phi(\mathbf{x})$ in the direction normal to the level set Γ_s can be then expressed as follows

$$\frac{\partial \phi}{\partial n} = \boldsymbol{\nabla}\phi(x,y) \cdot \mathbf{n} = \phi_x \frac{\phi_x}{\sqrt{\phi_x^2 + \phi_y^2}} + \phi_y \frac{\phi_y}{\sqrt{\phi_x^2 + \phi_y^2}} = \sqrt{\phi_x^2 + \phi_y^2} = |\boldsymbol{\nabla}\phi|,$$

so that we finally obtain for (C.1)

$$f(s) = \int_{\Gamma_s} \frac{g(\mathbf{x})}{|\boldsymbol{\nabla}\phi|}\, d\sigma \tag{C.5}$$

which is valid provided $|\boldsymbol{\nabla}\phi| \neq 0$ for every $\mathbf{x} \in \Gamma_s$.

Bibliography

[1] O. Volkov, B. Protas, W. Liao and D. Glander, "Adjoint–Based Optimization of Thermo–Fluid Phenomena in Welding Processes", *Journal of Engineering Mathematics* **65**, 201–220, (2009).

[2] J. Hadamard, *Lectures on the Cauchy Problem in Linear Partial Differential Equations*, Yale University Press, New Haven, (1923).

[3] G. H. Golub, C. F. Van Loan, *Matrix Computations*, 3rd Edition, Johns Hopkins University Press, Baltimore, (1996).

[4] C. R. Vogel, *Computational Methods for Inverse Problems*, SIAM (2002).

[5] A. Tarantola, *Inverse Problem Theory and Methods for Model Parameter Estimation*, SIAM (2005).

[6] M. D. Gunzburger, *Perspectives in Flow Control and Optimization*, SIAM (2003).

[7] H. Banks and K. Kunisch, *Estimation Techniques for Distributed Parameter Systems*, Birkhäuser (1989).

[8] M. Z. Nashed and O. Scherzer, *Inverse Problems, Image Analysis, and Medical Imaging*, AMS (2002).

[9] J. Gottlieb and P. DuChateau, *Parameter Identification and Inverse Problems in Hydrology, Geology, and Ecology*, Kluwer Academic Publishers (1996).

[10] I. M. Navon, "Practical and Theoretical Aspects of Adjoint Parameter Estimation and Identifiability in Meteorology and Oceanography", *Dynamics of Atmospheres and Oceans* **27**, 55–79, (1998).

[11] G. Chavent and P. Lemonnier, "Identification de la Non–Linearité D'Une Équation Parabolique Quasilineaire", *Applied Mathematics and Optimization* **1**, 121–162, (1974).

[12] O. M. Alifanov, A. V. Nenarokomov, S. A. Budnik, V. V. Michailov and V. M. Ydin, "Identification of Thermal Properties of Materials with Applications for Spacecraft Structures", *Inverse Problems in Science and Engineering* **12**, 579–594, (2004).

[13] O. M. Alifanov, S. A. Budnik, V. V. Michaylov, A. V. Nenarokomov, D. M. Titov, and V. M. Ydin, "An Experimental–Computational System for Materials Thermal Properties Determination and its Application for Spacecraft Structures Testing", *Acta Astronautica* **61**, 341–451, (2007).

[14] X.-C. Tai and T. Kärkkäinen, "Identification of a Nonlinear Parameter in a Parabolic Equation from a Linear Equation", *Computational and Applied Mathematics* **14**, 157–184, (1995).

[15] P. DuChateau, R. Thelwell and G. Butters, "Analysis of an Adjoint Problem Approach to the Identification of an Unknown Diffusion Coefficient", *Inverse Problems* **20**, 601–625, (2004).

[16] M. Janicki and S. Kindermann, "Recovering Temperature Dependence of Heat Transfer Coefficient in Electronic Circuits", *Inverse Problems in Science and Engineering* **17**, 1129–1142, (2009).

[17] M. Hanke and O. Scherzer, "Error Analysis of an Equation Error Method for the Identification of the Diffusion Coefficient in a Quasi-Linear Parabolic Differential Equation" , *SIAM J. Appl. Math.* **59** 1012–1027, (1999).

[18] Ph. Kügler, *Identification of a Temperature Dependent Heat Conductivity by Tikhonov Regularization*, Diploma Thesis, Johannes Kepler Universität Linz (2000).

[19] Ph. Kügler, "Identification of a Temperature Dependent Heat Conductivity from Single Boundary Measurements", *SIAM J. Numer. Anal.* **41**, 1543–1563, (2003).

[20] A. Neubauer, "Identification of a Temperature Dependent Heat Conductivity via Adaptive Grid Regularization", *Journal of Integral Equations and Applications* **20**, 229–242, (2008).

[21] J. R. Cannon and P. DuChateau, "An Inverse Problem for a Nonlinear Diffusion Equation", *SIAM J. Appl. Math.* **39**, 272–289, (1980).

[22] P. DuChateau, "An Inverse Problem for the Hydraulic Properties of Porous Media", *SIAM J. Math. Anal.* **28**, 611–632, (1997).

[23] J. L. Steward, I. M. Navon, M. Zupanski, and N. Karmitsa, "Impact of Non–Smooth Observation Operators on Variational and Sequential Data Assimilation for a Limited–Area Shallow–Water Equation Model", *In Early View in the Quart. Jour. Roy. Met. Soc.* (2011).

[24] D. Luo, L. He, S. Lin, T.–F. Chen, and D. Gao, "Determination of Temperature Dependent Thermal Conductivity by Solving IHCP in Infinite Regions", *Int. Comm. Heat Mass Transfer* **30**, 903–908, (2003).

[25] L. T. Biegler, O. Ghattas, M. Heinkenschloss, D. Keyes, and B. van Bloemen Waanders, *Real–time PDE–constrained Optimization*, SIAM (2007).

[26] V. Bukshtynov, O. Volkov, B. Protas, "On Optimal Reconstruction of Constitutive Relations", *Physica D* **240**, 1228–1244, (2011).

[27] V. Bukshtynov, B. Protas, "Optimal Reconstruction of Material Properties in Complex Multiphysics Phenomena" (in preparation).

[28] W. Muschik, "Aspects of Non-Equilibrium Thermodynamics", World Scientific, (1989).

[29] B. D. Coleman and W. Noll, "The Thermodynamics of Elastic Materials with Heat Conduction and Viscosity", *Arch. Rat. Mech. Anal* **13**, 167–178, (1963).

[30] I.-S. Liu, "Method of Lagrange Multipliers for Exploitation of the Entropy Principle", *Arch. Rat. Mech. Anal* **46**, 131–148, (1972).

[31] V. Triano, Ch. Papenfuss, V. A. Cimmelli, and W. Muschik, "Exploitation of the Second Law: Coleman–Noll and Liu Procedure in Comparison", *J. Non-Equilib. Thermodyn.* **33**, 47–60, (2008).

[32] D. Luenberger, *Optimization by Vector Space Methods*, John Wiley and Sons (1969).

[33] J. Nocedal and S. Wright, *Numerical Optimization*, Springer (2002).

[34] A. Ruszczyński, *Nonlinear Optimization*, Princeton University Press (2006).

[35] M. S. Berger, *Nonlinearity and Functional Analysis*, Academic Press (1977).

[36] G. Kirchhoff, *Vorlesungen über die Theorie der Warme*, Barth, Leipzig (1894).

[37] J. Neuberger, *Sobolev Gradients and Differential Equations*, Springer (1997).

[38] B. Protas, T. Bewley and G. Hagen, "A Comprehensive Framework for the Regularization of Adjoint Analysis in Multiscale PDE Systems", *Journal of Computational Physics* **195** (1), 49-89, (2004).

[39] B. Protas, "Adjoint–Based Optimization of PDE Systems with Alternative Gradients", *Journal of Computational Physics* **227**, 6490–6510, (2008).

[40] H. Engl, M. Hanke and A. Neubauer, *Regularization of Inverse Problems*, Kluver (1996).

[41] R. C. Aster, B. Borchers and C. Thurber, *Parameter Estimation and Inverse Problems*, Elsevier Academic Press (2005).

[42] P. C. Hansen, *Rank-Deficient and Discrete Ill-Posed Problems: Numerical Aspects of Linear Inversion*, SIAM (1998).

[43] C. Homescu, I. M. Navon and Z. Li, "Suppression of Vortex Shedding for Flow Around a Circular Cylinder Using Optimal Control", *Int. J. Numer. Meth. Fluids* **38**, 43–69, (2002).

[44] S. Zahedi, A.-K. Tornberg, "Delta Functions Approximations in Level Set Methods by Distance Function Extension", *Journal of Computational Physics* **229**, 2199–2219, (2010).

[45] B. Engquist, A.-K. Tornberg and R. Tsai, "Discretization of Dirac Delta Functions in Level Set Methods", *Journal of Computational Physics* **207**, 28–51, (2004).

[46] P. Smereka, "The Numerical Approximation of a Delta Function with Application to Level Set Methods", *Journal of Computational Physics* **211** (1), 77–90, (2006).

[47] A. Mayo, "The Fast Solution of Poisson's and the Biharmonic Equations on Irregular Regions", *SIAM Journal of Numerical Analysis* **21**, 285–299, (1984).

[48] J. T. Beale, "A Proof that a Discrete Delta Function is Second–Order Accurate", *Journal of Computational Physics* **227**, 2195–2197, (2008).

[49] J. D. Towers, "Discretizing Delta Functions via Finite Differences and Gradient Normalization", *Journal of Computational Physics* **228**, 3816–3836, (2009).

[50] J. D. Towers, "Two Methods for Discretizing a Delta Function Supported on a Level Set", *Journal of Computational Physics* **220**, 915–931, (2007).

[51] C. Min, F. Gibou, "Geometric Integration over Irregular Domains with Application to Level–Set Methods", *Journal of Computational Physics* **226**, 1432–1443, (2007).

[52] C. Min, F. Gibou, "Robust Second-Order Accurate Discretizations of the Multi-Dimensional Heaviside and Dirac Delta Functions", *Journal of Computational Physics* **227**, 9686–9695, (2008).

[53] S. Boyd and L. Vandenberghe, *Convex Optimization*, Cambridge University Press, (2004).

[54] S. Osher, J.A. Sethian, "Fronts Propagating with Curvature Dependent Speed: Algorithms Based on Hamiltonian–Jacobi Formulations", *Journal of Computational Physics* **79**, 12–49, (1988).

[55] M. S. Gockenbach, *Understanding and Implementing the Finite Element Method*, SIAM, (2006).

[56] C.E. Pérez, J.-M. Thomas, S. Blancher and R. Creff, "The Steady Navier–Stokes/Energy System with Temperature–Dependent Viscosity – Part 1: Analysis of the Continuous Problem", *International Journal for Numerical Methods in Fluids* **56**, 63–89, (2007).

[57] Ch.-H. Bruneau and M. Saad, "The 2D Lid–Driven Cavity Problem Revisited", *Computers & Fluids* **35**, (2006).

[58] U. Ghia, K. N. Ghia, and C. T. Shin, "High–Re Solutions for Incompressible Flow Using the Navier–Stokes Equations and a Multigrid Method", *Journal of Computational Physics* **48**, 387–411, (1982).

[59] `http://www.freefem.org`

[60] R. Schreiber, H. B. Keller, "Driven Cavity Flows by Efficient Numerical Techniques", *Journal of Computational Physics* **49**, 310–333, (1983).

[61] S. P. Vanka, "Block–Implicit Multigrid Solution of Navier-Stokes Equation in Primitive Variables", *Journal of Computational Physics* **65**, 138–158, (1986).

[62] B. Protas and W. Liao, "Adjoint–Based Optimization of PDEs in Moving Domains", *Journal of Computational Physics* **227**, 2707–2723, (2008).

[63] P. Grisvard, *Elliptic Problems in Nonsmooth Domains*, Pitman Publishing (1985).

[64] R. A. Adams, *Sobolev Spaces*, Academic Press, (1975).